Control and Operation of Offshore Wind Farms Connected with Diode Rectifier HVDC Systems

Lujie Yu

A thesis presented in fulfilment of the requirements for the degree of Doctor of Philosophy

Department of Electronic and Electrical Engineering

University of Strathclyde, Glasgow, UK

March 2019

This thesis is the result of the author's original research. It has been composed by the author and has not been previously submitted for examination which has led to the award of a degree.

Signed: Date:

Dedicated to my family

Acknowledgements

I would like to express my deepest gratitude to Prof. Lie Xu for his constructive supervision and invaluable guidance during my PhD study. He has always been able to share interesting research ideas with me and give helpful feedback to my work. His research attitude, methods and passion motivate me to become a person with high efficiency and integrity. I would also like to express my thanks to Dr. Derrick Holliday for his help and constructive comments.

My special gratitude goes to Dr. Rui Li, who has always been patient to help me when I got stuck with a research issue and provide useful comments for the manuscript I wrote. The encouragement from Dr. Grain P Adam is highly appreciated, especially when I was with negative mood. I would also like to thank Dr. Agusti Egea Alvarez, Dr. Dong Chen, Md Habibur Rahman, Gabriele Amico and other colleagues in PEDEC research group for all the help and advice.

A gracious acknowledgement is made to my dear friends---Yin Chen, Ding Zhou, Xiaozuo Huang, Deyang Guo for being there for me, sharing all the happiness and challenges. In addition, I am grateful to Yiran Jing and Yinyong Zhang for the help with my transition to Glasgow.

Financial support from University of Strathclyde and China Scholarship Council (CSC) is greatly appreciated.

Abstract

Due to the advantage of abundant space and more consistent wind speed, interest in offshore wind energy has significantly increased. To reduce the cost related to offshore wind power integration, this thesis investigates the control, modelling and operation of offshore wind farms connected with diode rectifier HVDC (DR-HVDC) systems, where a diode rectifier is used offshore and a modular multilevel converter (MMC) is used onshore. Compared to MMC based HVDC systems, the main benefits of DR-HVDC are lower investment, lower space requirement, higher efficiency and improved robustness. However, as the diode rectifier is unable to control offshore frequency and voltage as the MMC counterpart does, permanent magnet synchronous generator based wind turbines (WTs) have to perform more control functions including the establishment of the offshore AC network.

In order to ensure that each WT converter autonomously contributes to the regulation of the overall offshore voltage and frequency, a distributed phase locked loop-based control for WT converters connected with DR-HVDC is proposed. A small-signal state-space model of the DR-HVDC system is developed to justify the use of active power and voltage (*P*-*V*) control, and reactive power and frequency (*Q*-*f*) control. The WT level analysis is implemented and to reveal the coupling between WT active power and reactive power with such control scheme. An angle compensation control is further proposed to reduce the coupling during WT active power change. Small-signal analysis is also carried out to investigate the impact of the angle compensation control parameters, active power control parameters and reactive power control parameters on system stability.

To ride-through onshore faults, an active MMC DC voltage control combined with a WT overvoltage limiting control is proposed. With this control scheme, active power re-balance between the offshore and onshore side is achieved faster and thus, the MMC submodule capacitor overvoltage is alleviated. During offshore AC faults, a current limiting method is proposed to ensure the safe operation of WTs and an effective offshore overcurrent protection solution is proposed for fault detection and isolation. In addition, the system response during permanent DC pole-to-pole faults is analysed.

Finally, the operation of offshore wind farms connected with two parallel transmission links, i.e. a DR-HVDC and a HVAC link, is investigated. A hierarchical control structure which contains primary, secondary and tertiary controls, is proposed to ensure reliable operation and smooth transition between DR-HVDC mode, HVAC mode and parallel mode.

List of Abbreviations

DFIG	Doubly-Fed Induction Generator
DR-HVDC	Diode Rectifier HVDC
DRU-HVDC	Diode Rectifier Unit based HVDC
EU	European Union
FBSM	Full Bridge Submodule
FRC	Fully-Rated Converter
GPS	Global Position System
GSC	Generator-Side Converter
HBSM	Half Bridge Submodule
HVAC	High Voltage Alternating Current
HVDC	High Voltage Direct Current
IGBT	Insulated Gate Bipolar Transistor
LCC	Line Commutated Converter
LSC	Line-Side Converter
MMC	Modular Multilevel Converter
MTDC	Multi-Terminal HVDC
PCC	Point of Common Coupling
PLL	Phase Locked Loop
PMSG	Permanent Magnet Synchronous Generator
PWM	Pulse Width Modulation
RSC	Rotor-Side Converter
SCIG	Squirrel Cage Induction Generator
STATCOM	Static Compensator
THD	Total Harmonic Distortion

VDCOL	Voltage Dependent Current Order Limit
VSC	Voltage Source Converter
WRIG	Wound Rotor Induction Generator
WT	Wind Turbine

List of Symbols

Offshore wind farms symbols:

V_{pcc}	Offshore PCC voltage
θ_{pcc}	Offshore PCC phase angle
f_{pcc}	Offshore PCC frequency
P_{wt}	WT LSC active power
Q_{wt}	WT LSC reactive power
v_f	WT LSC filter voltage
θ_f	WT LSC filter phase angle
i_w	WT LSC inductance current
i_s	WT transformer LSC side current
v_c	WT LSC output voltage
R_w	WT LSC resistance
L_w	WT LSC inductance
C_f	WT LSC filter capacitance
T_{wt}	Turn ratio of WT transformer
k_{pllp}	Proportional gain of WT phase lock loop
k_{plli}	Integral gain of WT phase lock loop
k_f	Gain of WT frequency control
k_q	Gain of WT reactive power and frequency droop control
k_{vp}	Proportional gain of WT voltage control loop
k_{vi}	Integral gain of WT voltage control loop
k_{ip}	Proportional gain of WT current control loop

k_{ii}	Integral gain of WT current control loop
k_{pp}	Proportional gain of WT active power control loop
k_{pi}	Integral gain of WT active power control loop
Subscript *d*,*q*	*d*-axis and *q*-axis value
Subscript *ref*	Reference of the value
Subscript n_0	Nominal value
Subscript *0*	Operating point
Subscript max	Maximum value
Subscript min	Maximin value
k_{pq}	Parameter of WT angle compensation control
k_{v0}	Overvoltage capability of WT converters
k_0	Overload capability of WT converters
I_{rated}	WT converter rated current
i_{BS}	Current of the offshore breaker

Offshore diode rectifier symbols:

I_{dcr}	Diode rectifier DC current
P_{dr}	Diode rectifier AC power
Q_{dr}	Reactive power consumption of diode rectifier
V_{dcr}	Diode rectifier DC voltage
P_{dc}	Diode rectifier DC power
T_{dr}	Turn ratio of the diode rectifier transformer
X_{dr}	Reactance of the diode rectifier transformer
L_{dr}	Inductance of the diode rectifier transformer

C_1	Reactive power compensation capacitance
R_1	Resistance of diode rectifier low frequency filter
C_2, C_3	Capacitances of diode rectifier low frequency filter
L_1	Inductance of diode rectifier low frequency filter
R_2	Resistance of diode rectifier high frequency filter
C_4	Capacitance of diode rectifier high frequency filter
L_2	Inductance of diode rectifier high frequency filter
R_{dc}	Resistance of HVDC cables
L_{dc}	Capacitance of HVDC cables
C_{dc}	Inductance of HVDC cables
v_1, v_2, v_3, v_4	Voltage of C_1, C_2, C_3 and C_4
i_1, i_2	Current of L_1 and L_2
i_{dr}	AC current of diode rectifier
v_{dcc}	DC voltage of DC cable capacitor
φ, μ	Diode rectifier power factor angle and commutation overlap angle

Onshore modular multilevel converter symbols:

V_{sm}	Capacitor voltage of submodule in MMC
V_{dci}	MMC DC voltage
I_{dci}	MMC DC current
n_{up}, n_{down}	Number of inserted submodules in the upper arm and lower arm
N	Rated total number of inserted submodules in each phase

HVAC link and hierarchical control symbols:

V_{T2}	Voltage of the HVAC link
θ_{T2}	Phase angle of the HVAC link
P_{ac}	AC power of the HVAC link
k_{svp}	Proportional gain of secondary voltage control loop
k_{svi}	Integral gain of secondary voltage control loop
T_v	Delay of the secondary voltage control
k_{fp}	Proportional gain of secondary frequency control loop
k_{fi}	Integral gain of secondary frequency control loop
T_d	Delay of the secondary frequency control
k_{synp}	Proportional gain of phase angle control loop
k_{syni}	Integral gain of phase angle control loop

List of Figures

List of Tables

Table of Contents

Chapter 1 Introduction

1.1 Offshore wind development

To reduce the greenhouse gas emission and lower the dependency on fossil fuels, European Union (EU) sets a target of boosting renewable energy share to 20% in 2020 and 32% in 2030 [1]. According to European Environment Agency, renewable energy used in 2017 accounted for 17.4 % of total energy consumption in the EU and 11 Member States have already reached their national 2020 renewable energy targets [2].

Fig. 1. 1 shows the development of different energies from 2005 to 2017 in the EU [3], and it clearly shows that wind energy has played a major role during the transition towards a more sustainable and cost-effective energy system. With a cumulative installed capacity of 168.7 GW in 2017, wind energy overtook coal and became the second largest energy source. It is anticipated that, in the next five years, wind energy will become the major energy source with a cumulative installed capacity exceeding 258 GW [4].

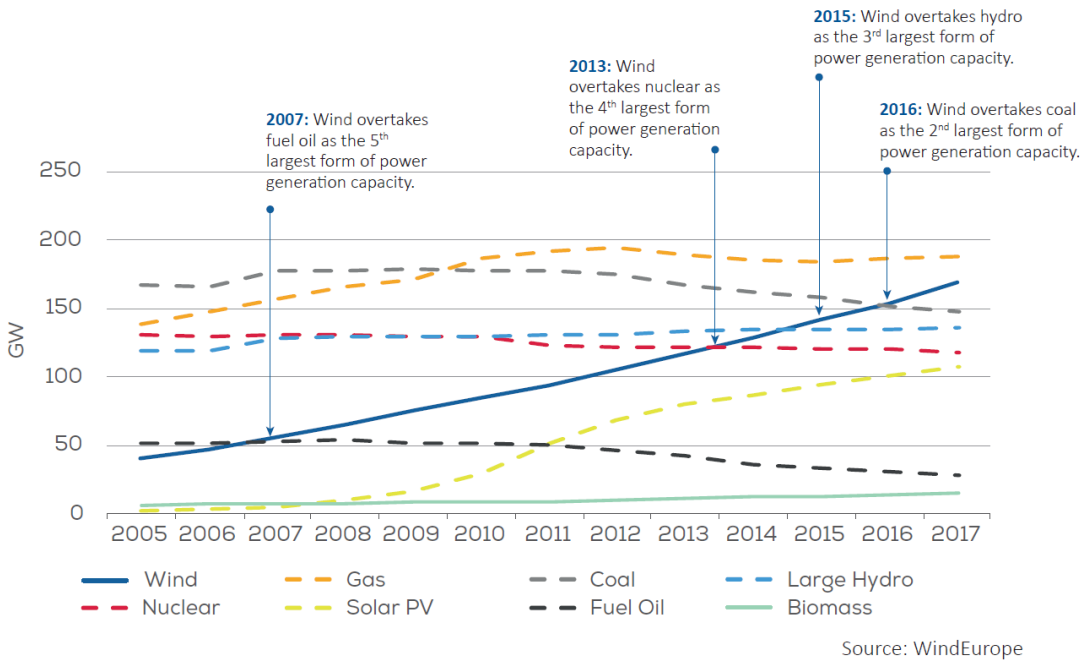

Fig. 1. 1 Total power generation capacity in the EU from 2005-2017 [3].

Due to the advantage of abundant space and more consistent wind speed, interest in offshore wind energy has significantly increased [5]. EU has set a new record of annual offshore wind turbines (WTs) installation in 2017 (3,148 MW) and expanded its cumulative installed capacity of offshore wind to 15,780 MW, as presented in Fig. 1. 2 [5]. The United Kingdom leads the offshore turbine installation among all the member states in EU, accounting for 43% of EU's total offshore installed capability [5].

To reduce the cost of offshore WT installations, the power rating of offshore wind turbines has significantly increased recent years. The average power rating of offshore WTs installed in 2017 was 5.9 MW, 23% larger than that in 2016 [5]. Such increase will continue in the following years, and it is anticipated that the majority of offshore WT installations after 2019 will be above 8 MW and 10 MW offshore WTs are expected to be commercially available before 2022 [5].

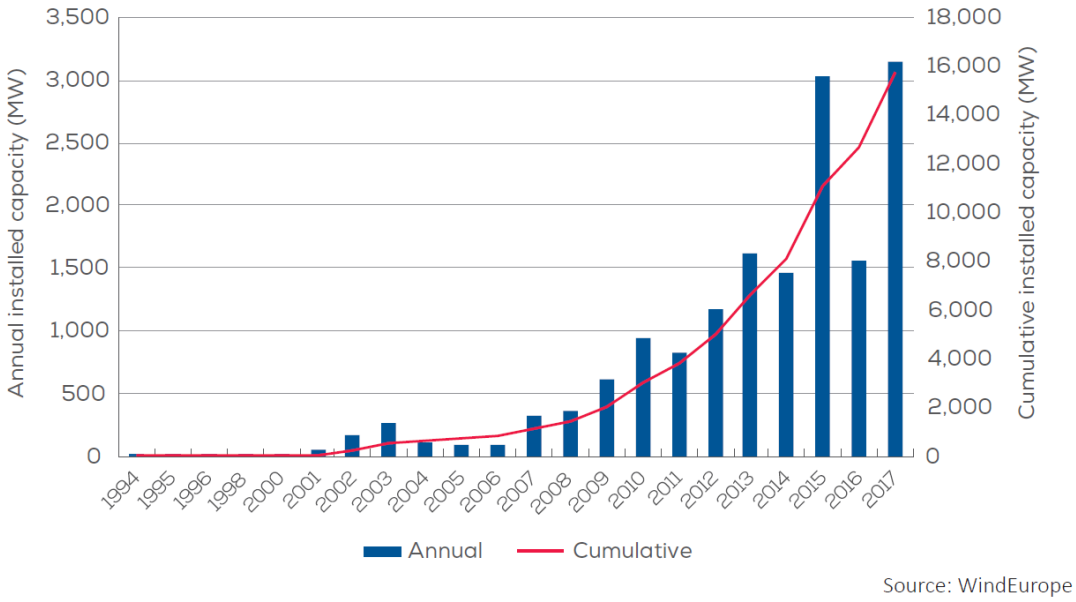

Fig. 1. 2 Cumulative and annual installed capacity of offshore wind energy [5].

1.2 Offshore wind power transmission solutions

The rapid offshore wind energy development requires reliable and efficient transmission technology. High-voltage-alternating-current (HVAC) and high-voltage-

direct-current (HVDC) have been used commercially in several projects for grid integration of offshore wind power [6].

1.2.1 HVAC for offshore wind energy transmission

HVAC is a proven transmission technology when the offshore wind farms are located near onshore. Fig. 1. 3 shows a “typical” layout of HVAC connected offshore wind farms. WTs in the offshore wind farms are connected to the point of common coupling (PCC) through the collection system typically at 33 kV or 66 kV. A step-up transformer, installed in the offshore substation, is used to increase the AC voltage from collection level to transmission level, e.g. 132 kV. Through the subsea three phase AC cables, wind power is transmitted to the onshore grid.

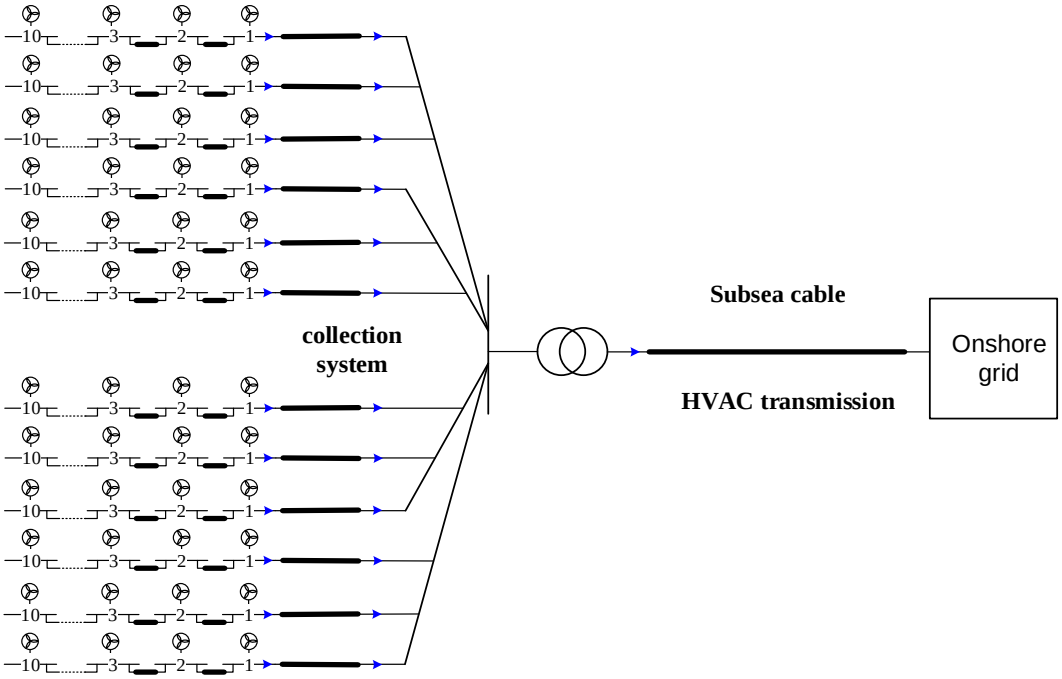

Fig. 1. 3 Layout of HVAC connected offshore wind farms.

The main characteristics of HVAC when used for offshore wind power transmission are as follows [6-8]:

- HVAC is the simplest and most cost-effective solution for relatively low power and short-distance offshore wind power transmission.

- Charging currents of AC cables reduce the transmission capability and increase power losses, which becomes more severe with the increase of transmission length. Offshore reactive power compensation such as switched reactors, static compensator (STATCOM) and/or static VAR compensator may be required for long-distance power transmission to limit voltage rise and improve efficiency.
- The offshore network and onshore grid are synchronously coupled. Faults on one side of the network will directly affect the other side.
- High capacitance of HVAC cables may result in harmonic resonance.

1.2.2 HVDC for offshore wind energy transmission

HVDC technology is a more attractive solution for long-distance large offshore wind farm connection. Fig. 1. 4 shows a "typical" layout of HVDC connected offshore wind farms. WTs are connected to the PCC through the AC collection system, and an offshore HVDC rectifier is used to convert the offshore AC power to DC power. The DC power is then transmitted to the onshore inverter through the HVDC cables and is converted back to AC. Table 1. 1 shows the existing HVDC connected offshore wind farm projects [9, 10].

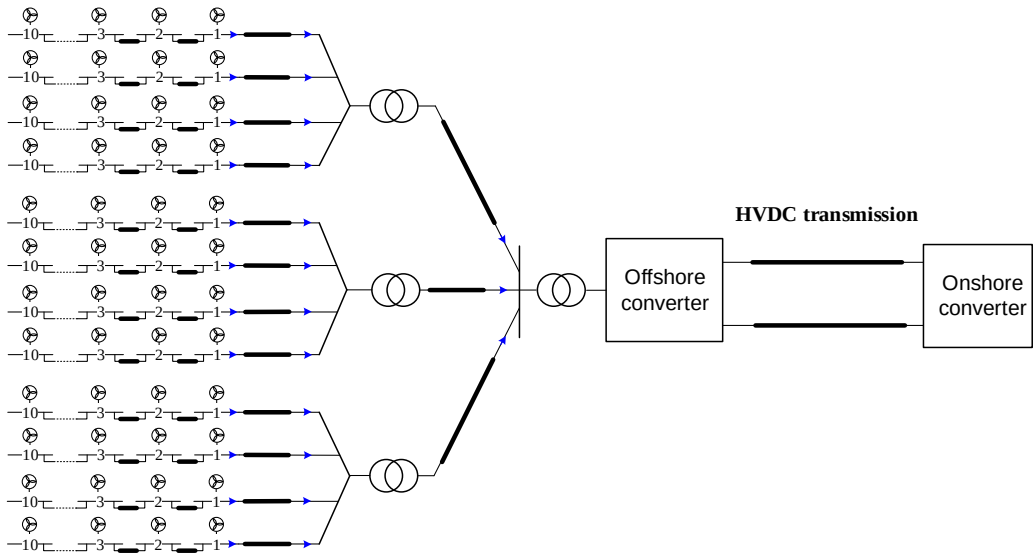

Fig. 1. 4 Layout of the HVDC connected offshore wind farms.

Comparing with HVAC, HVDC offers the following advantages [6, 11, 12]:

- There is no technical limit on transmission distance, as HVDC cables do not consume reactive power.
- The offshore network and onshore grid are decoupled, so the impact of one side faults on the other is reduced.

The potential disadvantage of HVDC when comparing with HVAC for offshore wind power transmission is the higher cost. But with its further development, it is expected the cost of HVDC can be reduced significantly[6].

Table 1. 1 Existing HVDC connected offshore wind farm projects

Project	Capacity	Voltage	Length	Year	Converter
Tjaereborg	7.2 MW	±9 kV	17.2 km	2000	Two-level
BorWin 1	400 MW	±150 kV	200 km	2015	Two-level
BorWin 2	800 MW	±300 kV	200 km	2015	MMC
HelWin 1	576 MW	±250 kV	130 km	2015	MMC
SylWin 1	864 MW	±320 kV	205 km	2015	MMC
HelWin 2	690 MW	±320 kV	130 km	2015	MMC
DolWin 1	800 MW	±320 kV	165 km	2015	MMC
DolWin 2	916 MW	±320 kV	135 km	2017	MMC
DolWin 3	900 MW	±320 kV	160 km	2018	MMC
BorWin 3	900 MW	±320 kV	160 km	2019	MMC

1.3 Scope of the thesis

1.3.1 Research motivation and objective

The commercially used HVDC technology for long-distance offshore wind power transmission is based on voltage source converters (VSCs) [9, 10]. Comparing with line commutated converters (LCCs), VSCs provide the advantages of more compact design, fewer filter banks and no commutation failure. Besides, VSCs are capable of establishing the offshore AC voltage and frequency, behaving like an AC source. This enables the easy implementation of WT controller design, as the operation requirements of WTs under such case are similar to those when connected with HVAC.

Early VSC-HVDC links used two-level converter [9], but the HVDC projects for offshore wind power transmission in commission recent years or under construction are all based on MMC [10]. Comparing with the two-level VSC, MMC offers the advantages of modular construction, easier scalability to high DC voltage, fewer AC filters, reduced voltage derivative (*dv/dt*) and higher efficiency. However, the following drawbacks must be taken into consideration when MMC-HVDC is used for offshore wind power transmission [12]:

- Offshore MMC converter has large volume and heavy weight, making the construction of offshore platform difficult and costly.
- Complex control system.
- High station power losses and capital cost.

The above drawbacks have reinvigorated new interest in exploring alternatives to MMC-HVDC transmission solutions. Recently, connection of offshore wind farms using diode rectifier HVDC (DR-HVDC) systems, where a diode rectifier is used offshore and an MMC is used onshore, has drawn a lot of attention [13, 14]. The main benefits of DR-HVDC when compared to MMC-HVDC are lower investment, lower space requirement, higher efficiency and improved robustness [15, 16]. As presented in [17], compared with MMC-HVDC for offshore wind farm connection, the volume and transmission losses are reduced by 80% and 20% respectively, while the total cost can be reduced by 30%. However, as the uncontrolled diode rectifier is unable to provide offshore frequency and voltage control as the MMC counterpart does, WTs have to perform more control functions. In addition to the transmission of the generated wind power, WTs have to establish offshore network with satisfactory AC voltage magnitude and frequency.

Therefore, this thesis will investigate the control, modelling and operation of the DR-HVDC for offshore wind power transmission, with main focus on development of suitable control method for the WTs to ensure safe and reliable system operation during normal and fault conditions. Small-signal stability analysis will be used to assist with tuning of the controllers. In addition, parallel operation of DR-HVDC and HVAC links will also be explored.

1.3.2 Thesis contributions

The main contributions of this thesis are:

- A distributed PLL based control is proposed for offshore WT converters connected through DR-HVDC systems, which enables WTs to operate autonomously and contribute to the overall offshore AC voltage and frequency regulation.
- A small-signal state-space model of the WTs connected with DR-HVDC systems is developed. Wind farm level and WT level analysis is carried out to reveal the interactions between active / reactive powers, and offshore AC voltage / frequency. An angle compensation control is further proposed for WT converters to reduce the coupling between WT active and reactive powers.
- An active onshore MMC DC voltage control combined with a WT overvoltage limiting control is proposed to alleviate the MMC submodule capacitor overvoltage during onshore AC faults. A fault current limiting method is proposed to avoid converter overcurrent during offshore AC faults and an effective offshore AC fault overcurrent protection solution is proposed for offshore fault detection and isolation.
- Parallel operation of DR-HVDC and HVAC links connected with offshore wind farms is investigated. A hierarchical control structure, which includes the primary control, secondary control and tertiary control, is proposed to achieve seamless transitions between various operation modes.

1.4 Author's Publications

[1] **L. Yu**, R. Li, and L. Xu, "Distributed PLL-Based Control of Offshore Wind Turbines Connected With Diode-Rectifier-Based HVDC Systems," *IEEE Transactions on Power Delivery,* vol. 33, pp. 1328-1336, 2018.

Abstract: A distributed PLL-based frequency control is proposed in this paper for offshore wind turbine converters connected with diode-rectifier based high-voltage-direct-current (HVDC) systems. The proposed control enables a large number of wind turbines to work autonomously to contribute to the offshore AC frequency and voltage regulation. The proposed control also provides automatic synchronization of the

offline wind turbines to the offshore AC grid. Stability of the proposed frequency control is analysed using root locus method. Moreover, an active dc voltage control of the onshore modular multilevel converter (MMC) is proposed to ride-through onshore AC fault, where the onshore MMC converter quickly increases the dc voltage by adding additional submodules in each phase, in order to rapidly reduce wind farm active power generation so as to achieve quick active power re-balance between the offshore and onshore sides. Thus, the overvoltage of the submodule capacitor is alleviated during the onshore fault, reducing the possibility of system disconnection. Simulation results in PSCAD verify the proposed control strategy during start-up, synchronization and under onshore and offshore fault conditions.

[2] **L. Yu**, R. Li, and L. Xu, " Hierarchical control of offshore wind farm connected by parallel diode-rectifier based HVDC and HVAC links," *IET Renewable Power Generation*. (accepted).

Abstract: This paper investigates the operation of offshore wind farm connected by parallel diode-rectifier based HVDC (DR-HVDC) and HVAC links. A secondary voltage control is proposed to control the offshore AC voltage amplitude by regulating the DC voltage of the DR-HVDC link. A secondary frequency control and a phase angle control are proposed to adjust the reactive power reference in the primary control, which synchronise the offshore point of common coupling (PCC) frequency and phase angle to those of the HVAC link. Such secondary voltage control, frequency control and phase angle control enable seamless transition from DR-HVDC mode to parallel mode. A tertiary power control scheme is further proposed to control the active power flow distribution between DR-HVDC and HVAC links through the regulation of PCC phase angle. To ensure smooth transition from HVAC mode to parallel mode, a virtual DC power control is proposed to control the virtual DC power at zero prior to the connection of the DR-HVDC link. A small-signal model of the parallel system is developed and the stability analysis is carried out for the proposed control scheme. Simulation results in PSCAD/EMTDC verify the proposed control under normal and fault conditions.

[3] **L. Yu**, R. Li, L. Xu and Grain P. Adam, "Analysis and Control of Offshore Wind Farm Connected with Diode Rectifier based HVDC System," *IEEE Transactions on Power Delivery.* (under second-round review).

Abstract: This paper analyses the control and operation of offshore wind farms connected with diode rectifier based HVDC (DR-HVDC) system. A small-signal state-space model of the offshore wind turbines (WTs) and DR-HVDC system is developed to investigate the interactions among the active and reactive power (*P* and *Q*), offshore AC voltage and frequency (*V* and *f*) at the offshore network level. The impact of using the previously proposed *P-V* and *Q-f* control on the individual WT active and reactive power transmission to offshore AC network and their interaction are clarified. In order to reduce the coupling between WT active power and reactive power, an angle compensation control is proposed where an additional phase shift is directly added to the WT output voltage based on the WT's active power output. The effectiveness of the proposed control on improving dynamic response and reducing active and reactive power interaction is verified by frequency-domain analysis and time-domain simulations in PSCAD/EMTDC.

[4] **L. Yu**, R. Li, and L. Xu, "Parallel operation of diode-rectifier based HVDC link and HVAC link for offshore wind power transmission," in the 7th International Conference on Renewable Power Generation (RPG2018), 2018.

Abstract: This paper investigates the integration of large offshore wind farms using parallel HVAC and diode-rectifier based HVDC (DR-HVDC) systems. Three different operation modes, i.e. HVAC operation mode, DR-HVDC operation mode and parallel operation mode are investigated. A wind turbine control scheme including distributed control and centralized control is proposed to ensure the stable operation of the offshore wind farms under different operation modes. The proposed control requires no switching of the distributed control strategy when operation mode is changed. Moreover, power flow between the DR-HVDC link and HVAC link under parallel operation can be well controlled with the centralized control. Simulation results in PSCAD/EMTDC verify the proposed control during transition among the three operation modes.

[5] R. Li, **L. Yu**, and L. Xu, "Offshore AC Fault Protection of Diode Rectifier Unit-Based HVdc System for Wind Energy Transmission," *IEEE Transactions on Industrial Electronics*, vol. 66, pp. 5289-5299, 2019.

Abstract: Offshore AC fault protection of wind turbines (WTs) connecting with diode rectifier unit based HVDC (DRU-HVDC) system is investigated in this paper. A voltage-error-dependent fault current injection is proposed to regulate the WT current during offshore AC fault transients and quickly provide fault current for fault detection. Considering different fault locations, the fault characteristics during symmetrical and asymmetrical faults are presented and the requirements for fault detection are addressed. A simple and effective offshore AC fault protection solution, combining both overcurrent protection and differential protection, is proposed by utilizing the developed fast fault current providing control. To improve system availability, reduced DC voltage of the DRU-HVDC system is investigated, where one of the series-connected DRUs is disconnected and the onshore modular multilevel converter (MMC) actively reduces DC voltage to resume wind power transmission. The proposed scheme is robust to various offshore AC faults and can automatically restore normal operation. Simulation results confirm the proposed fault protection strategy

[6] R. Li, **L. Yu**, L. Xu and Grain P. Adam, " Coordinated Control of Parallel DR-HVDC and MMC-HVDC Systems for Offshore Wind Energy Transmission," *IEEE Journal of Emerging and Selected Topics in Power Electronics.* (under second-round review).

Abstract: Parallel operation of diode rectifier based HVDC (DR-HVDC) and modular multilevel converter (MMC) based HVDC (MMC-HVDC) for transmitting offshore wind power is investigated in this paper. An enhanced active power control scheme of the offshore MMC station is proposed to improve the power flow distribution between the MMC-HVDC and DR-HVDC links which are both connected to the offshore wind farm AC network. By regulating the offshore voltage, all the wind powers are transmitted via the DR-HVDC link in low wind conditions while the offshore MMC power is controlled around zero to reduce transmission losses, considering the

efficiency superiority of DR-HVDC over its MMC counterpart. When the DR-HVDC is out of service, wind energy is transferred via the MMC-HVDC and the wind turbine generated power is automatically limited by slightly increasing the offshore AC voltage to avoid potential MMC-HVDC overload. A power curtailment control is also proposed which slightly increases the DC voltage of the DR-HVDC to enable autonomous reduction of the generated wind power so as to avoid DR-HVDC overload during MMC-HVDC outage. The proposed coordinated control only uses local measurements and, without the need for communication, can seamlessly handle transitions including various faults. The proposed scheme provides a highly efficient solution with flexible operation for integrating large offshore wind farms. Simulation results confirm the proposed control strategy.

[7] R. Li, **L. Yu**, and L. Xu, "Operation of offshore wind farms connected with DRU-HVDC transmission systems with special consideration of faults," *Global Energy Interconnection,* vol. 1, pp. 608-617, 2018.

Abstract: The diode rectifier unit (DRU)-based high-voltage DC (DRU-HVDC) system is a promising solution for offshore wind energy transmission thanks to its compact design, high efficiency, and strong reliability. Herein we investigate the feasibility of the DRU-HVDC system considering onshore and offshore AC grid faults, DC cable faults, and internal DRU faults. To ensure safe operation during the faults, the wind turbine (WT) converters are designed to operate in either current-limiting or voltage-limiting mode to limit potential excessive overcurrent or overvoltage. Strategies for providing fault currents using WT converters during offshore AC faults to enable offshore overcurrent and differential fault protection are investigated. The DRU-HVDC system is robust against various faults, and it can automatically restore power transmission after fault isolation. Simulation results confirm the system performance under various fault conditions.

[8] R. Li, **L. Yu**, L. Xu, and G. P. Adam, "DC Fault Protection of Diode Rectifier Unit Based HVDC System Connecting Offshore Wind Farms," in *2018 IEEE Power & Energy Society General Meeting (PESGM)*, pp. 1-5, 2018.

Abstract: DC fault ride-through operations of the offshore wind farm connecting with diode rectifier unit (DRU) based HVDC link are presented in this paper. A voltage-error-dependent fault current injection is proposed to regulate the WT current during DC faults and to provide fault current. This contributes the control of the offshore AC voltage, which does not drop to zero but is remained relatively high to facilitate fast system recovery after clearance of a temporary DC fault. The WT converters operate on current limiting mode during DC faults and automatically restore normal operation after fault clearance. The full-bridge based modular multilevel converter (MMC) is adopted as the onshore station and its DC fault current control ability is explored to effectively suppress the fault current from the onshore station around zero, which reduces semiconductor losses and potential overcurrent risk of the MMC station. Simulation results confirm the robustness of the system to DC faults.

1.5 Thesis organization

This thesis is organised as follows:

Chapter 2 presents a general overview of HVDC systems connected offshore wind farms, including the operation of LCC-HVDC, VSC-HVDC, hybrid HVDC and DR-HVDC.

Chapter 3 presents the offshore WT control requirements when connected to DR-HVDC, and develops a distributed and autonomous PLL-based WT control strategy, which includes current control, voltage control, PLL based frequency control, active and reactive power control. PSCAD simulations are then carried out to verify the effectiveness of the proposed control strategy.

Chapter 4 develops a small-signal model of WTs connected with DR-HVDC systems. Based on the developed model, the wind farm level analysis is conducted to clarify the interactions between active and reactive power, offshore AC voltage and frequency. WT level analysis is carried out to reveal the coupling between WT active power and reactive power with the proposed control scheme. An angle compensation control is further proposed to reduce such power coupling. The effectiveness of the

proposed control is verified by frequency domain results and PSCAD/EMTDC time domain simulations.

Chapter 5 develops an active DC voltage control of onshore MMC combined with a WT overvoltage limiting control to ride-through onshore AC faults. By adding additional submodules in each phase in MMC, the onshore MMC converter quickly increases the DC voltage and the WTs reach overvoltage limit faster to alleviate the overvoltage of MMC submodules. A fault current limiting method is also developed to ensure the continuous operation of WTs during offshore AC faults. To facilitate the detection and isolation of offshore faults, a simple and effective offshore AC fault overcurrent protection solution is proposed. In addition, the system response after permanent DC pole-to-pole faults is investigated. Simulation results in PSCAD verify the proposed strategy under various fault conditions.

Chapter 6 investigates the parallel operation of DR-HVDC and HVAC links connected offshore wind farms. A secondary control scheme, including secondary voltage control, secondary frequency control and phase angle control, is proposed to achieve seamless transition from DR-HVDC operation mode (when offshore wind farms are only connected with DR-HVDC link) to parallel operation mode (when offshore wind farms are connected with both DR-HVDC and HVAC links). To regulate the active power flow distribution between the two links on parallel operation mode, a tertiary power control scheme is proposed, whereas a virtual DC power control is developed to ensure smooth transition from HVAC mode to parallel mode. Simulation results in PSCAD/EMTDC verify the proposed control under normal and fault conditions.

Chapter 7 draws the conclusions and provides recommendations for future work.

Chapter 2 Review on HVDC connected offshore wind farms

This chapter provides an overview of HVDC connected offshore wind farms. WT generator types for offshore application and their developments are described first. A general overview of four offshore HVDC transmission solutions, i.e. LCC-HVDC, VSC-HVDC, hybrid-HVDC and DR-HVDC is then presented and the advantages and disadvantages of different solutions are compared.

2.1 WT generator types

There are mainly four types of WTs that have been used, i.e. fixed-speed WT based on squirrel cage induction generator (SCIG), wound rotor induction generator (WRIG) based WT with variable rotor resistance, doubly-fed induction generator (DFIG) based WT, fully-rated converter (FRC) based WT [18, 19].

Fixed-speed WT based on SCIG [7, 8, 19] as shown in Fig. 2. 1 was employed in early wind farms due to its simple structure and low cost. But it is unable to track maximum wind power as the generator rotating speed is largely fixed with very small variation. The low wind energy conversion efficiency of such WT has limited its market share and there has been very limited use in recent years.

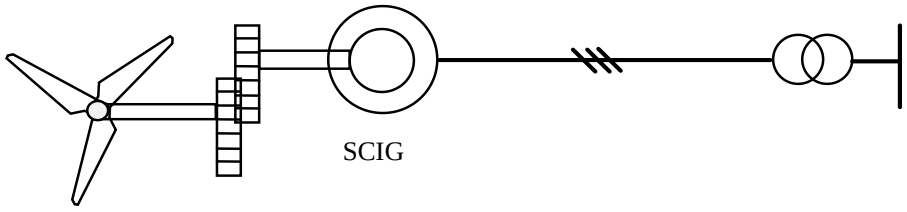

Fig. 2. 1 Diagram of a SCIG based fixed-speed WT.

WRIG-WT with variable rotor resistance was used to achieve variable-speed operation [18, 19], as shown in Fig. 2. 2. By regulating the variable resistance connected in series with the rotor winding, WRIG is able to change the rotating speed within 10% above the synchronous speed. But high loss caused by the additional rotor resistance limits its use.

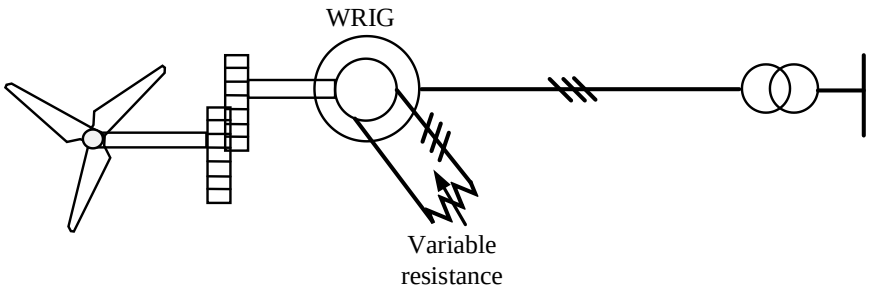

Fig. 2. 2 Diagram of a WRIG-WT with variable resistance.

DFIG-WT is an economic approach to operate with variable speed [20], as shown in Fig. 2. 3. Its stator is connected with the AC grid directly while its rotor is connected through back-to-back VSCs, namely a rotor-side converter (RSC) and a line-side converter (LSC). The VSC is typically rated at around 30% of the DFIG capability. By controlling the current fed into the rotor, the rotational speed of the DFIG is decoupled from the synchronous frequency and is able to vary at a range of ± 25%. The main drawback of DFIG-WT is the need of slip-rings and complicated scheme to ride-through external network faults.

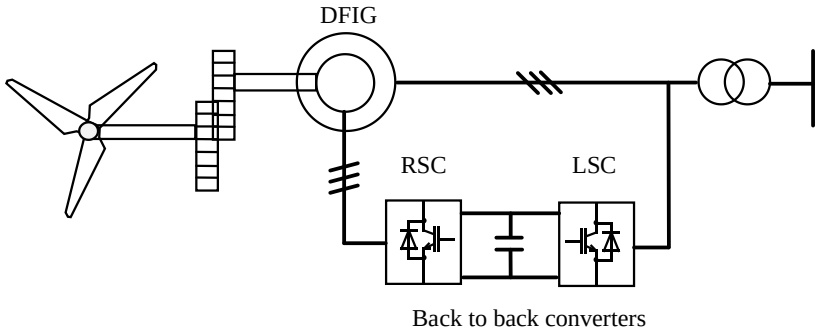

Fig. 2. 3 Diagram of a DFIG-WT.

FRC-WT**,** uses synchronous or induction generators which are connected to the AC grid through back-to-back fully-rated converters, i.e. a generator-side converter (GSC) and an LSC, as shown in Fig. 2. 4. FRC-WT is the most attractive solution for offshore application due to its low maintenance cost, high reliability and controllability [19]. Permanent magnet based synchronous generator (PMSG) becomes one of the most popular among all FRC-WTs [21], due to its no need of extra electrical power

for excitation, compact design and high reliability. Table 2. 1 shows the comparison of the four discussed WT generator types.

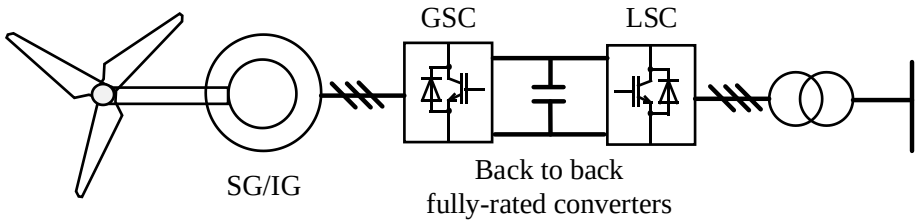

Fig. 2. 4 Diagram of an FRC-WT.

Table 2. 1 WT generator types

Generator types	**Advantage**	**Disadvantage**
SCIG-WT	Simple structure and low cost	Low wind energy conversion efficiency, complicated scheme to ride-through external faults
WRIG-WT	Improved energy conversion efficiency with variable-speed operation at a range of 10%	High power loss, complicated scheme to ride-through external faults
DFIG-WT	Improved energy conversion efficiency with variable-speed operation at a range of ± 25%	Complicated scheme to ride-through external faults
FRC-WT	Low maintenance cost, high reliability and controllability	Increased cost due to the need of fully rated converter

2.2 Offshore HVDC transmission solutions

When HVDC is used for offshore wind power integration, the onshore inverter maintains DC voltage, hence ensuring balanced active power between offshore and onshore sides. Referring to the types of offshore HVDC rectifiers, HVDC transmission

solutions can be classified as LCC-HVDC, VSC-HVDC, hybrid-HVDC and DR-HVDC.

2.2.1 LCC-HVDC

LCC-HVDC is a proven technology with commercial operation over 60 years. It is widely used for power transmission in onshore grid due to its advantages of large capacity, high reliability and low power loss. LCC uses thyristor valves and is usually arranged as a 12-pulse bridge, as shown in Fig. 2. 5. The 12-pulse bridge is formed of two 6-pulse bridges connected in series on DC side and in parallel on AC side through a star-star-delta transformer. Under such connections, harmonic currents (especially the 5^{th} and 7^{th}) generated by the thyristor bridge during operation can be effectively reduced. However, using LCC-HVDC for offshore wind power transmission has the following challenges:

- LCC needs an external voltage source for its commutation. When used offshore, this may require additional auxiliary equipment to establish a stable offshore network. Alternatively, the WTs need to form the offshore network.
- Breaker-switched passive filters are required to eliminate harmonics and support reactive power consumption of LCC. These filters require large footprint and are heavily weighted, creating challenges for offshore platform construction.

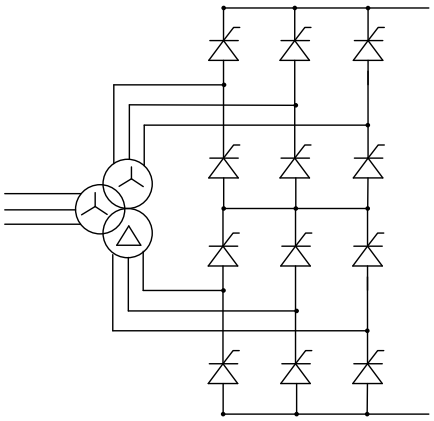

Fig. 2. 5 Twelve-pulse bridge of LCC.

2.2.2 VSC-HVDC

VSC-HVDC uses self-commutated insulated-gate-bipolar-transistors (IGBTs) [11, 20], which can be turned on and off multiple times per fundamental period, independent of grid voltage and current. Comparing with LCC-HVDC, VSC-HVDC provides the following advantages in offshore applications [11, 20]:

- Offshore VSC has the ability to form the offshore network, WT control can be designed in a similar way as for onshore applications.
- Offshore VSC can control reactive power and generates less harmonics, and thus only small filter banks or no filters are required.

These features make VSC-HVDC attractive for commercial offshore wind power integration. Early schemes used two-level VSC [9] and Fig. 2. 6 illustrates its topology. Pulse-width-modulation (PWM) with high switching frequency is employed to synthesize a sinusoidal AC voltage output. The main limitations of two-level VSC for offshore application include [22]:

- High switching frequency results in high converter power loss.
- Substantial filter is required to reduce AC harmonics.
- High voltage derivative *dv/dt* results in unwanted electromagnetic interference and limits its scalability to higher voltage level.
- Large numbers of IGBTs are connected in series in order to withstand high DC voltage which brings significant technical challenges.
- During pole-to-pole DC faults, DC-link capacitors are discharged and generate high fault current.

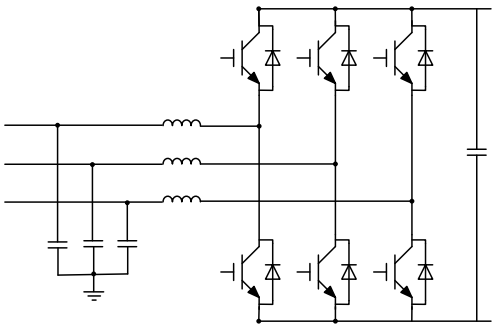

Fig. 2. 6 Two-level VSC.

MMC, as shown in Fig. 2. 7 (a), receives increased interest since it was first proposed in 2003 [23]. It consists of 6 arms and each arm contains a large number of series-connected submodules. Comparing with the two-level VSC, MMC offers the following advantages [23-26]:

- Modular construction with good scalability to meet any voltage level requirement.
- Increased efficiency due to reduced switching frequency.
- Good output waveform quality and thus small (or even no) AC filters.
- Absence of large DC-link capacitors.
- Reduced voltage derivative (dv/dt).

Half bridge submodule (HBSM) and full bridge submodule (FBSM) as shown in Fig. 2. 7 (b) and (c) respectively are the two main submodule configurations used for MMCs [25, 26]. The output voltage of a HBSM is V_{sm} when the upper IGBT S_1 is switched on and zero when the lower IGBT S_2 is switched on. The output voltage of a FBSM is V_{sm} when IGBTs S_1 and S_4 are switched on, zero when IGBTs S_1 and S_3 or S_2 and S_4 are switched on, and $-V_{sm}$ when IGBTs S_2 and S_3 are switched on. Compared with HBSM based MMC, FBSM based MMC has the advantage of DC fault blocking capability and is able to operate with reduced DC voltage [25, 26].

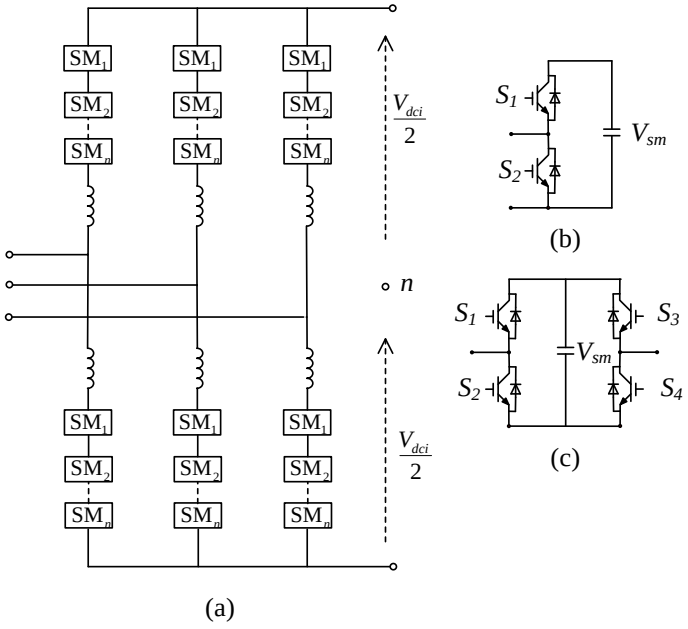

Fig. 2. 7 MMC and two submodule topologies.

2.2.3 Hybrid-HVDC

In [27], a hybrid-HVDC is proposed for offshore wind power transmission, where the offshore converter is made up of series-connected LCC and VSC, as shown in Fig. 2. 8. The offshore VSC is capable of establishing the offshore AC voltage and supporting the commutation of LCC. With the use of LCC, the transmission capacity can be easily increased while the power loss and cost can be effectively reduced. However, comparing with MMC-HVDC, the offshore footprint of this hybrid structure is increased due to the need of LCC AC filters and the control design becomes more complicated due to the need of DC voltage sharing between the two series-connected converters.

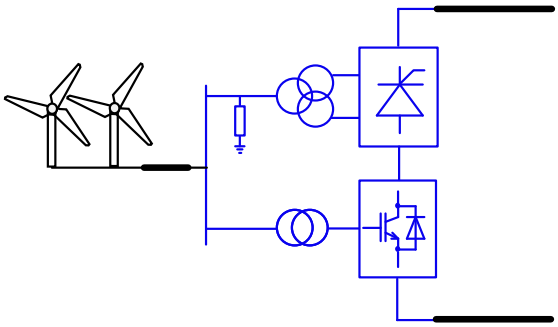

Fig. 2. 8 Series-connected LCC and VSC for connecting offshore wind farms.

Another hybrid offshore converter composing of series-connected DR and VSC is proposed in [28-30], as shown in Fig. 2. 9. By replacing the offshore LCC with DR, the power losses, maintenance and capital cost are further reduced while the reliability is increased. The challenges of this solution for offshore application are similar to those when series-connected LCC and VSC is used.

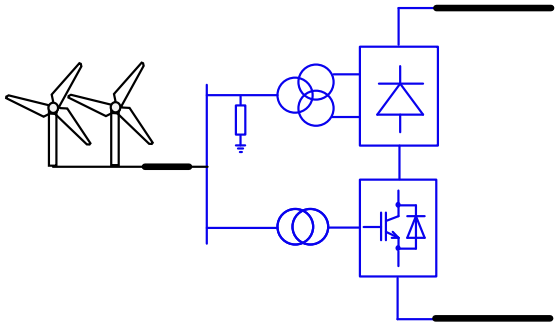

Fig. 2. 9 Series-connected DR and VSC for connecting offshore wind farms.

2.2.4 DR-HVDC

DR-HVDC is proposed in [31-34] for offshore wind power transmission, where an uncontrollable 12-pulse DR is used as the offshore converter, as shown in Fig. 2. 10. Compared with the previously presented HVDC transmission approaches, DR-HVDC offers the following advantages:

- Simplest and most robust offshore HVDC converter.
- Reduced offshore platform volume and weight.
- Reduced offshore HVDC converter power losses.
- No need of complex control system for offshore HVDC converter.
- Reduced operation and maintenance costs.
- Easier transport and installation.

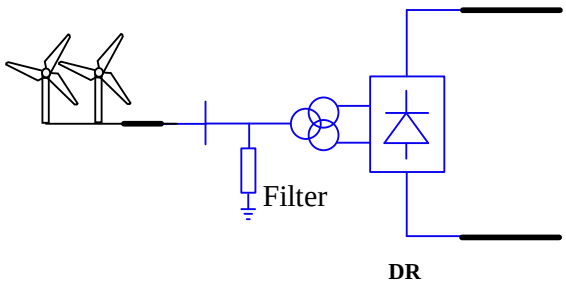

Fig. 2. 10 DR-HVDC for connecting offshore wind farms.

Although DR-HVDC system provides some attractive advantages, it also poses challenges for the offshore network operation. As DR-HVDC cannot offer the offshore network with frequency and voltage control as VSC-HVDC system does, WTs need to be capable of forming the offshore grid.

DR-HVDC has been further developed to diode rectifier unit based HVDC (DRU-HVDC) by Siemens [14, 35]. As shown in Fig. 2. 11, six DRUs are connected in series on the DC side to boost DC voltage while the AC sides are parallel connected to the wind farms. Each DRU is a 12-pulse bridge and two DRUs are installed together in a distributed offshore substation [16], as shown in Fig. 2. 12 (a) and (b), respectively. Such distributed DRU arrangements eliminate the large centralized offshore converter platform. The onshore inverter uses an MMC based on FBSMs to provide the capability of reduced DC voltage operation when some of the DRUs are bypassed, e.g. due to internal DRU faults.

As DR-HVDC systems and DRU-HVDC systems have largely the same characteristics, DR-HVDC systems are considered in this thesis for ease analysis. The proposed WT control, system modelling, stability analysis, fault ride-through strategies and operation for DR-HVDC systems are also applicable for DRU-HVDC systems.

Table 2. 2 compares the different HVDC transmission solutions.

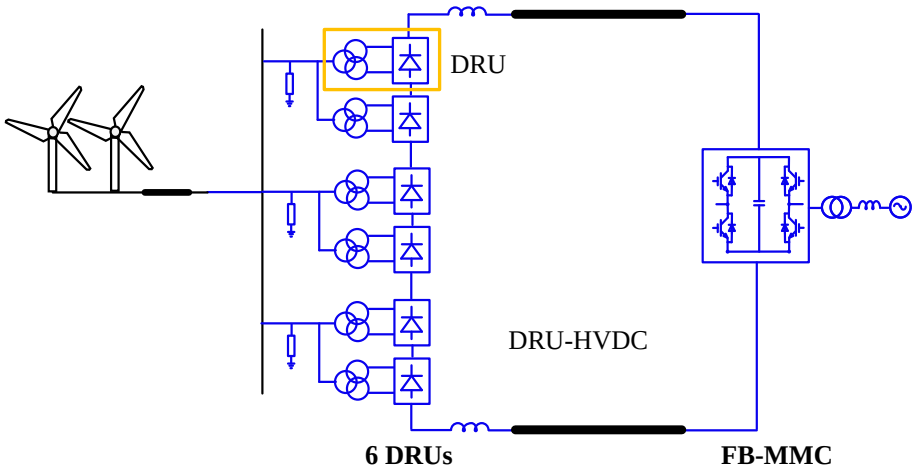

Fig. 2. 11 DRU-HVDC.

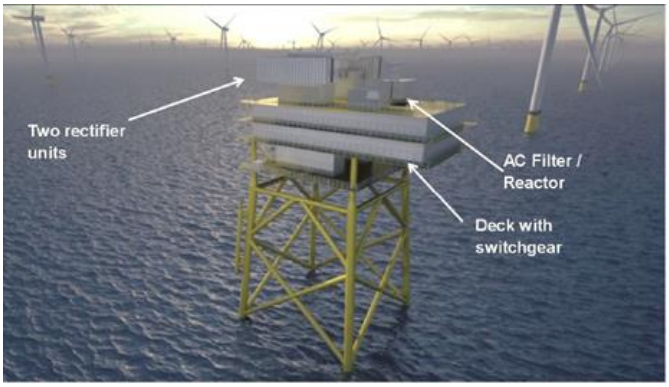

(a)

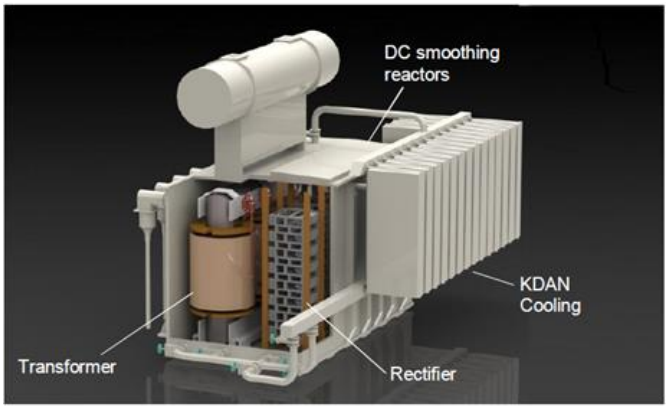

(b)

Fig. 2. 12 Distributed offshore substation and DRU presented by Siemens [16]: (a) distributed offshore substation; (b) DRU.

Table 2. 2 Offshore HVDC transmission solutions

HVDC solutions	Advantages	Disadvantages
LCC-HVDC	○ Large capacity ○ High reliability and low power loss	○ LCC needs an external voltage source for its commutation ○ Breaker-switched passive filters require large footprint
Two-level VSC-HVDC	○ Ability to form the offshore network ○ Small filter banks or no filters are required	○ High switching frequency and high converter power loss ○ High voltage derivative *dv/dt* ○ Technical challenges to connect large numbers of IGBTs in series ○ High fault current during pole-to-pole DC faults
MMC-HVDC	○ Modular construction with good voltage scalability ○ Reduced switching frequency ○ Small (or no) AC filters ○ Absence of large DC-link capacitors ○ Reduced *dv*/*dt*	○ Large volume and heavy weight of offshore MMC converter ○ Complex control system ○ High station power losses and capital cost
Hybrid-HVDC	○ Capability of establishing the offshore AC voltage by offshore VSC ○ Increased transmission capacity and reduced	○ Increased offshore footprint due to the need of LCC AC filters comparing with MMC-HVDC

	power loss and cost with the use of LCC	○ Complicated control design to share the DC voltage between two series-connected converters
DR-HVDC	○ Simplest and most robust offshore HVDC converter ○ Reduced offshore platform volume and weight ○ Reduced offshore HVDC converter power losses ○ No need of complex control system for offshore HVDC converter ○ Reduced operation and maintenance costs ○ Easier transport and installation	○ WTs need to form the offshore grid

2.3 Operation of LCC-HVDC for offshore wind power transmission

2.3.1 LCC-HVDC with a STATCOM

The operation of LCC-HVDC connected with offshore wind farms is first investigated in [11, 36], where an additional STATCOM is installed offshore to provide the commutation voltage and reactive power support for the HVDC rectifier. Fig. 2. 13 shows the control of DFIG-WT connected with a LCC-HVDC link and a STATCOM [11, 36]. In this configuration, STATCOM behaves as a grid-forming converter, controlling the offshore AC network with constant voltage magnitude, frequency and phase angle. For the LCC-HVDC link, the onshore inverter is on DC voltage control mode while the offshore rectifier controls DC current. The DC current control order is determined by an outer STATCOM DC voltage control, in order to

achieve the power balance between the generated wind power and LCC-HVDC transmitted active power. The DFIG-WT control is similar to that when connected with HVAC, i.e. GSC controls the power/torque and reactive power by regulating rotor current while LSC is applied to control the WT DC voltage and reactive power.

The study is extended in [37] to investigate the system operation under onshore grid faults. When the onshore voltage decreases to almost 0 after fault occurrence, the LCC inverter commutation failure happens, resulting in the collapse of the HVDC voltage. The active power unbalance between the offshore side and onshore side then leads to the increase of the STATCOM DC voltage. Such voltage increase is used as an indication of the onshore faults, and the STATCOM controlled offshore AC frequency is subsequently varied, allowing each WT to detect the faults and reduce its generated active power.

References [38-41] present the modelling of LCC-HVDC system with the STATCOM and an inner current loop is added in the STATCOM control. The potential use of such system for oil and gas platform in discussed in [42], whereas references [43, 44] present the small-signal modelling and analysis of the system. In [43], a phase-lead compensator is added in DC current control to increase the control bandwidth, whilst in [44] a proportional resonance controller is added in STATCOM AC voltage control to improve the stability.

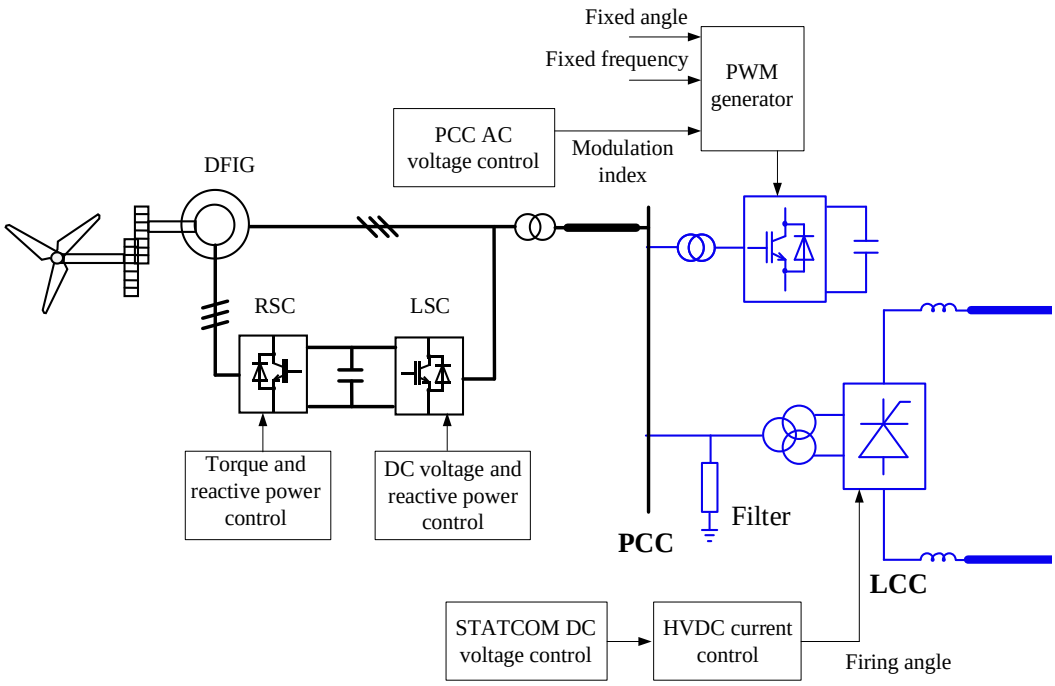

Fig. 2. 13 Control of DFIG connected with LCC-HVDC and STATCOM.

2.3.2 LCC-HVDC without STATCOM

Reference [45] investigates the operation of LCC-HVDC connected DFIG-WTs without the use of a STATCOM. The back-to-back converters in DFIG-WTs are used to establish the offshore AC voltage for LCC commutation. Fig. 2. 14 shows the control design of such a system, in which the DFIG RSC controls the stator flux of the DFIG while the LCC-HVDC rectifier controls the offshore frequency through the regulation of its firing angle. As the DFIG stator voltage is the combination of stator flux and offshore grid angular frequency, under such a control design, the offshore voltage can be maintained at a desired range.

References [46-49] add an inner HVDC current control for the offshore LCC and the transfer function between the offshore frequency and DC current is derived to design control parameters. Reference [50] presents the system operation when the offshore LCC controls the AC voltage magnitude instead of the frequency. Fault ride-through capability during onshore voltage sag of such a system is explored in [39], and an additional inertial and primary frequency control loop is added in the WT RSC to reduce system frequency variation during transients in [51]. Reference [52]

investigates the system optimisation with the objective of maximizing active power output, considering different wind speeds, HVDC cable lengths and WT reactive power ratings.

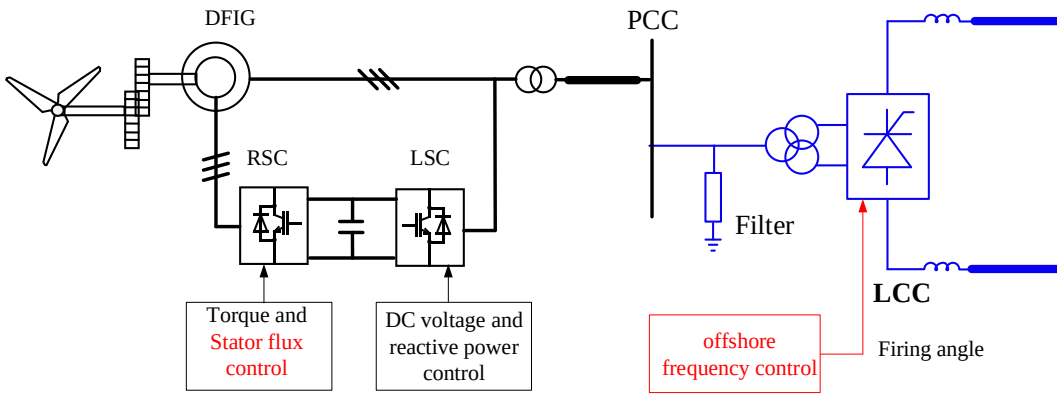

Fig. 2. 14 Control of LCC-HVDC connected DFIG-WTs without STATCOM.

Using LCC-HVDC to connect wind farms based on PMSG-WTs has been studied in [53-55], as shown in Fig. 2. 15. The offshore PCC voltage is controlled by LCC through the regulation of its firing angle whereas the offshore frequency is controlled through the adjustment of WT reactive power output [54]. However, the control of WTs relies on remote measurement of the PCC voltage and thus, it reduces the robustness of the control system. References [56-58] analyse the system stability when the offshore wind power is transmitted through LCC-HVDC with the consideration of an onshore synchronous generator.

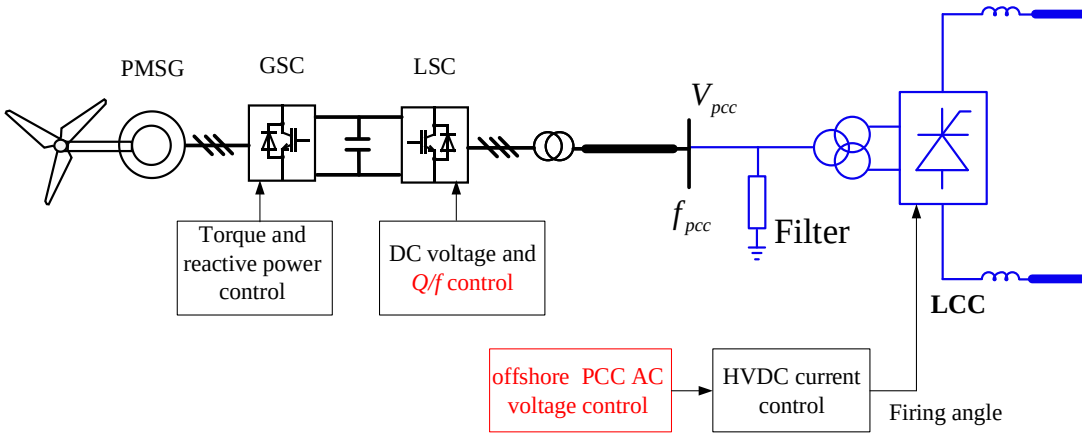

Fig. 2. 15 Control of LCC-HVDC connected PMSG-WTs without STATCOM.

2.4 Operation of VSC-HVDC for offshore wind power transmission

2.4.1 Control and fault analysis of VSC-HVDC

The operation of VSC-HVDC connected offshore wind farms is investigated in [11], and Fig. 2. 16 shows the controls of FRC-WTs and VSC-HVDC. The offshore HVDC rectifier is controlled to behave like an AC source with the capability to regulate offshore AC voltage and frequency. Thus, wind power generated by the WTs is absorbed by the offshore HVDC rectifier (as it resembles an infinite voltage source) and converted to DC power automatically. Under such HVDC converter control, the FRC-WT can be easily controlled, similar to the case of HVAC connection, e.g. the WT GSC controls the torque/active power and reactive power, while the LSC controls the WT DC voltage and reactive power.

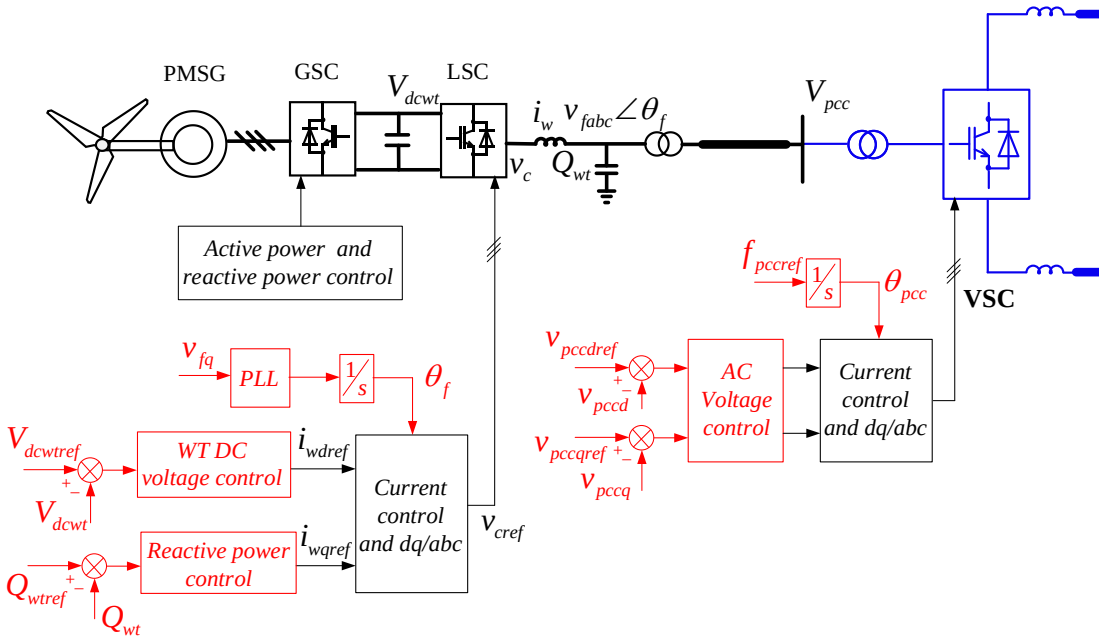

Fig. 2. 16 Control of WTs connected with VSC-HVDC.

Sharing the same control principle as in [11], fuzzy logic control and power synchronization control are used in [59, 60], respectively, and the fault performances under each control are also investigated. Reference [61] adds a PLL based frequency control in the offshore HVDC rectifier to provide a potential way for the HVDC rectifier to synchronize with the offshore network.

Reference [6] compares technical and economic aspects of three different transmission solutions, i.e. 150 kV HVAC, 400 kV HVAC and VSC-HVDC and concludes that VSC-HVDC is the preferred option when the offshore wind farms are more than 100 MW and located 90 km far away from onshore. WTs based on synchronous generators but without the use of back-to-back converters are proposed to be connected to offshore HVDC rectifier directly [62], in which the offshore frequency is regulated according to the total generated WT power. However, with this solution, each WT is unable to track the maximum power point due to the direct link between generator speed and offshore grid frequency.

A coordinated control strategy to ride-through onshore grid faults is proposed in [20]. In order to re-balance the active power between offshore and onshore sides after the onshore faults, the offshore PCC frequency is regulated, allowing each WT to detect the fault and reduce its active power without the use of communication. Reference [63] provides an overview of the onshore fault ride-through methods, including the use of a fully rated HVDC chopper, offshore HVDC power reduction or WT power reduction using fast communication, and automatic WT power reduction through offshore frequency increase and offshore voltage reduction.

To reduce the power oscillation and WT DC overvoltage during offshore asymmetrical faults, negative sequence current control is added to the offshore HVDC rectifier and WT LSC controllers [64]. System operation during DC pole-to-ground faults is investigated in [65] and improved control strategies for WTs and MMC are proposed to reduce fault current. Reference [66] proposes mixed HBSM and FBSM based MMC as the offshore rectifier and LCC as the onshore inverter to reduce the investment cost and power losses. During onshore voltage sags, the offshore MMC reduces the DC voltage to suppress the DC current increase caused by LCC commutation failure, which helps the system to achieve fast recover after fault clearance.

2.4.2 Small signal analysis of VSC-HVDC

Small signal models of VSC-HVDC connected offshore wind farms have been developed to investigate system stability [67, 68]. Reference [67] compares the

accuracy of aggregated model and detailed model according to time-domain and frequency-domain results, and it shows that the aggregated wind farm model can reduce simulation time and present similar frequency characteristics of the critical modes, but is unbale to reproduce accurate damping ratios. Small-signal analysis of a detailed WF model, consisting of 126 5MW FRC-WTs, are presented in [68], and participation analysis is carried out to identify the impacts of WT's PLL, LCL filter and HVDC rectifier control parameters on the critical modes. Reference [69] compares the system stability when offshore wind power is fed into a power system through a point-to-point VSC-HVDC, multi-terminal HVDC (MTDC) and HVAC, respectively, and a power oscillation damping control is designed to improve the MTDC system performance.

2.4.3 Operation of MTDC systems and parallel HVDC links

References [70-72] present the use of MTDC systems for connecting offshore wind farms, where two DC terminals are connected to two different wind farms while the other two DC terminals are connected to different onshore grids. In [70], DC voltage and active power droop control is proposed to ensure stable operation of the MTDC systems. In [71, 72], the same MTDC system structure is applied and its operation is investigated with three different transmission objectives, i.e. one onshore converter has the priority to absorb all the wind power until its power rating is reached, two onshore converters share the wind power, and a mixture of the above two objectives. Reference [73] presents a detailed state-space model of the wind farms connected with MTDC and small-signal analysis is carried out to identify the impact of the VSC controller on system stability, whereas reference [74] uses Newton-Raphson method to identify the power flow for VSC-MTDC connected offshore wind farms.

The operation of MTDC connected offshore wind farms to provide onshore frequency support is investigated in [75, 76]. A frequency support control is added as an outer loop in the original MTDC DC voltage / active power droop control. During large onshore frequency variation in one (or some) of the connected onshore network, the controller re-distributes the active power among the DC terminals to reduce AC frequency variation in the particular AC network. In addition, WT inertia response is

also considered to improve onshore grid frequency performance during onshore and offshore power unbalance.

References [77, 78] investigate the parallel operation of two point-to-point VSC-HVDC links connected with the same offshore wind farms. In [77], active power / frequency droop control is used for the offshore HVDC converters to regulate the power flow between the two HVDC links. During onshore faults at one of the links, the increase of the DC voltage at the link activates the offshore converter transient control, leading to the increase of offshore frequency and the consequent power transmission increase of the other link. After the offshore frequency increase hits the threshold set by each WT, the WT active power generation is then reduced to guarantee safe system operation. The work in [78] proposes a centralized outer offshore PCC voltage and frequency control loop to distribute the power flow between the two VSC-HVDC links. The produced current demand for the offshore HVDC converters is then shared between the two stations according to their power ratings.

Reference [79] investigates the parallel operation of VSC-HVDC and HVAC links for offshore wind power transmission. An active power control is added in the offshore HVDC VSC controller to adjust the active power distribution between the two links through the regulation of offshore PCC phase angle. Active power / frequency droop control and reactive power / voltage droop control are proposed in [80] for multiple offshore HVDC links connected with the same offshore wind farms. Small-signal model is established to analyse the impact of droop gains on system stability.

2.5 Operation of hybrid-HVDC for offshore wind power transmission

Series connection of different converter technologies has been considered, e.g. in [27] the operation of series-connected LCC and VSC is investigated whereas series connection of DR and VSC is studied in [28-30]. These two configurations share similar control principles. Fig. 2. 17 shows the control block diagram of series-connected DR and VSC based HVDC [28]. The offshore VSC establishes the offshore network with controlled voltage magnitude and frequency. It further regulates the VSC

DC voltage by controlling the active power exchange between its AC and DC sides. Moreover, the offshore VSC is controlled to operate as an active filter for the 11th and 13th order harmonic currents, to reduce the requirement for passive filters. Under the offshore VSC control, WT converter control can be implemented similar to that with HVAC connection. Onshore fault ride-through performance is also presented [28], but system response during offshore faults needs further elaboration due to the non-existence of any inner current control loop in the offshore VSC. Harmonic suppression control of the offshore VSC/MMC is further explored in [29, 30] to include the elimination of the 23rd, 25th order harmonic currents.

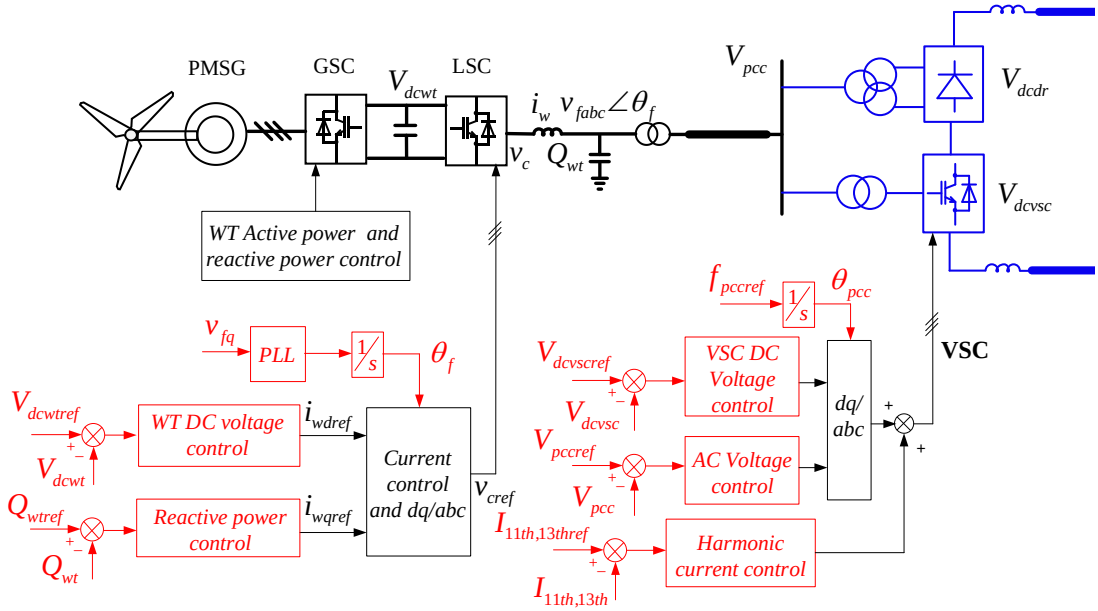

Fig. 2. 17 Control of series-connected DR and VSC based HVDC.

2.6 Operation of DR-HVDC for offshore wind power transmission

The operation of DR-HVDC connected offshore wind farms is first investigated in [31-34], where the offshore wind farms are simplified as a single aggregated WT. A WT voltage and frequency control is proposed, as shown in Fig. 2. 18. With WT DC voltage controlled by the GSC, LSC operates as a grid-forming converter to establish the offshore AC network with an open loop fixed offshore frequency control. Closed-loop active power control is used to regulate the WT AC voltage amplitude, transmitting active power from AC to DC by the DR. The main drawback of this

control is the use of fixed WT AC phase angle, making it difficult to apply in practical wind farms with large numbers of WTs.

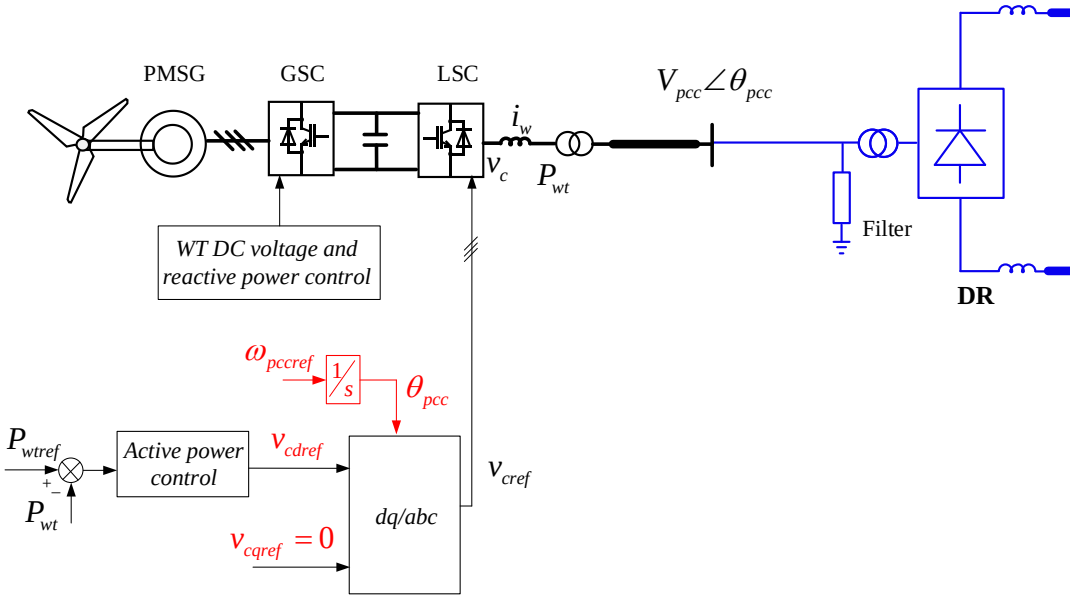

Fig. 2. 18 Control of a single aggregated WT connected with DR-HVDC.

Another WT voltage and frequency control is proposed in [81-83] to provide the capability of WT frequency and phase angle adjustment, although the offshore wind farms are still simplified as one aggregated WT. This control is further developed in [13, 84-87] to enable the operation of many parallel WT converters connected to DR-HVDC, as shown in Fig. 2. 19. The main objective of this control is to establish the PCC voltage magnitude and frequency by all the WT LSCs. When the DR is not conducting, each WT LSC shares certain active and reactive currents according to its own power rating, to control the offshore PCC AC voltage magnitude and frequency, respectively. When the DR is conducting to transmit the offshore wind power to onshore, WT active current is controlled to regulate the active power output [85]. Frequency / reactive current droop control is used to share the reactive current under both operation modes.

This method aims to share the total offshore current among the WTs for the establishment of offshore PCC voltage and frequency. Thus, the WT control relies on the remote measurement of offshore PCC voltage magnitude, frequency and phase

angle (used for voltage control, frequency control and *abc*/*dq* reference transformation), as shown in Fig. 2. 19. Such remote measurements require additional high-speed communication between the offshore PCC and each WT, reducing the control system robustness.

Using the same control principle, the work is extended to self-start-up operation [85, 88], and the analysis of system performances under onshore faults, offshore faults and DC faults [89]. References [90-92] investigate the effectiveness of the control and system efficiency when the offshore filter banks are reduced to one-fifth of the typical value. In [93], a model of WTs connected with DR-HVDC system is presented for stability analysis, though it is unable to derive accurate dynamic response due to the exclusion of offshore AC network frequency variation. References [94-96] investigate the feasibility of the DR-HVDC connected to MTDC, whereas in [97] potential operation of a 24-pulse DR-HVDC without using any offshore filter banks is studied and the system performances are compared with those of 12-pulse DR and 0.45 pu filter banks.

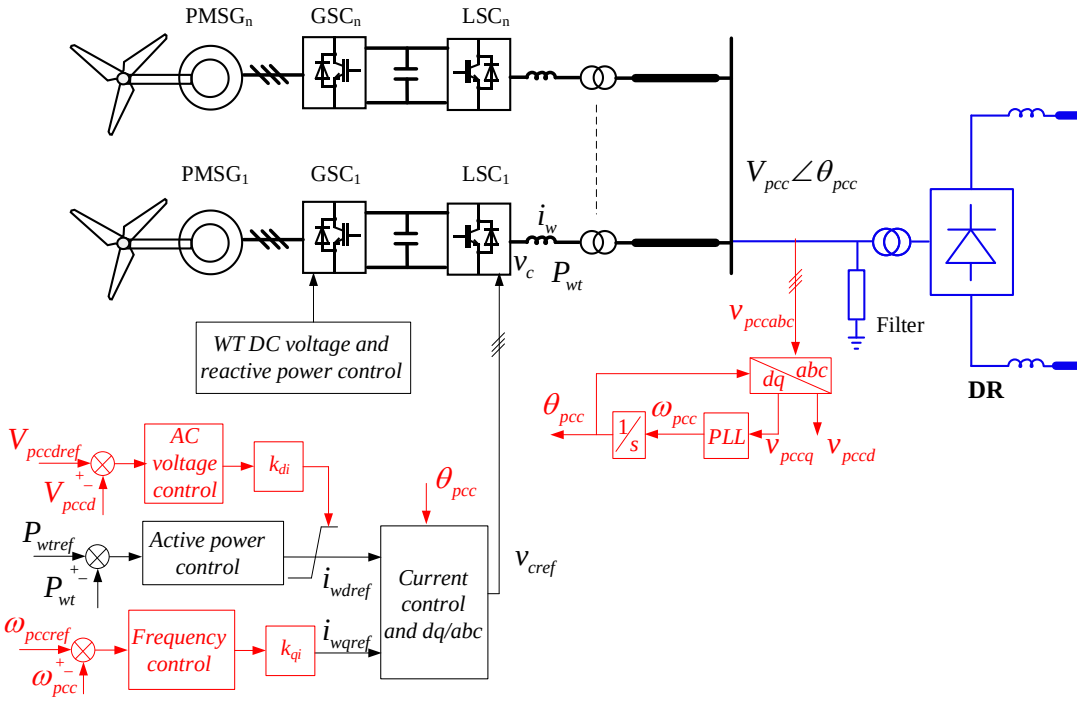

Fig. 2. 19 Control of parallel WTs connected with DR-HVDC.

In [98], a strategy based on an external centralized controller is proposed, as shown in Fig. 2. 20. The WT level control of this solution is similar to that when connected with HVAC or VSC-HVDC. However, an external centralized *f*-*Q* controller is needed to generate the total offshore reactive power requirement, which is then shared to each WT by communication. The offshore frequency control in this approach is similar to the control shown in Fig. 2. 19, except that the WT distributed control may improve its performance due to the use of PLL. However, system performance under low wind conditions needs further analysis due to the lack of offshore AC voltage control.

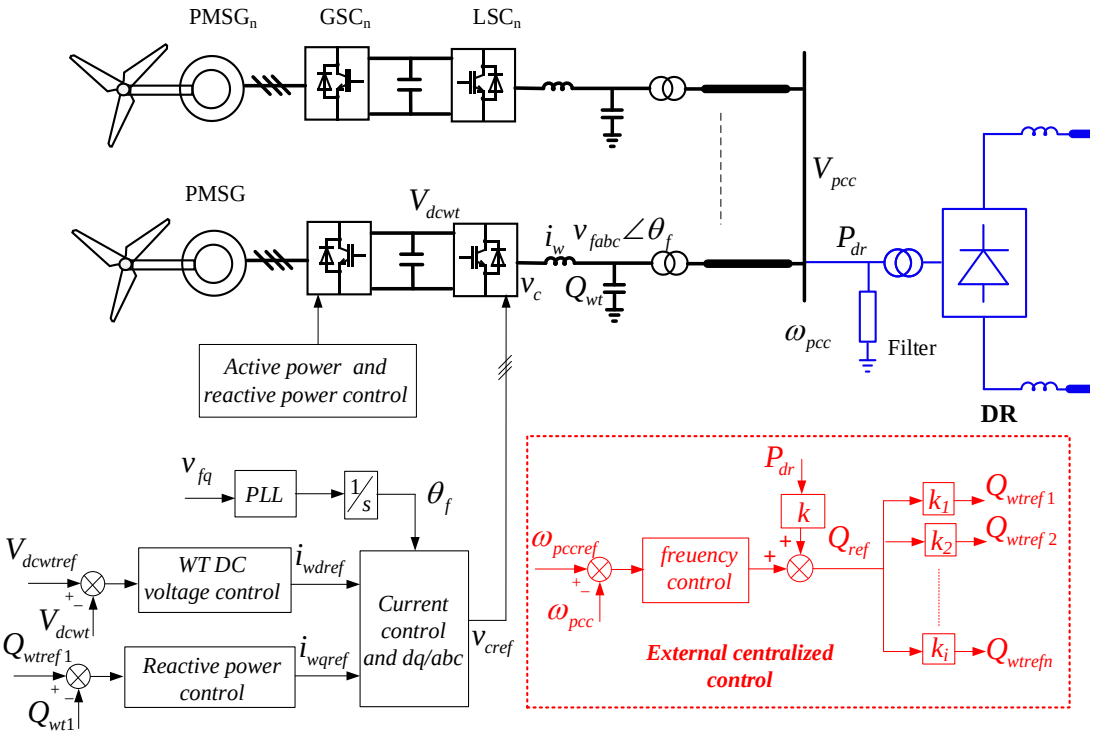

Fig. 2. 20 Control of WTs connected with DR-HVDC.

A FixReF control [99, 100] is proposed for offshore WTs when connected with DR-HVDC system, as shown in Fig. 2. 21. The global position system (GPS) is used to provide a fixed frequency reference and common angular reference for all the WTs. Thus, the aforementioned remote measurements for the offshore PCC frequency and angle can be avoided. A *q*-axis voltage v_{fq} and *q*-axis reactive current i_{wqref} droop control, expressed as $i_{wqref} = k_q v_{fq}$, is used to provide each WT with reactive power sharing capability and voltage phase angle regulation capability. This FixReF control

solution differs from PLL-based controls, as the rotating reference axis provided by the GPS is not aligned with the voltage vector any more. The main drawback of this control is the unsatisfactory reactive power sharing among the WTs. Although the v_{fq} / i_{wqref} droop control is used, the reactive power is not equally shared among the WT. Moreover, the use of the GPS leads to potential increase of investment cost and reduced robustness.

With the same WT control, reference [101] investigates the use of an umbilical AC cable to provide auxiliary power under low wind conditions and an additional AC/AC converter is installed onshore to control the umbilical AC power. Reference [102] shows the effectiveness of the FixReF control when the offshore wind farms are connected with both DR-HVDC and VSC-HVDC. System performances when using the WT control shown in Fig. 2. 19 and the FixReF control shown in Fig. 2. 21 are compared in [103] and it concludes that the control method in Fig. 2. 19 may not be able to control PCC voltage when the offshore collection AC cables are considered.

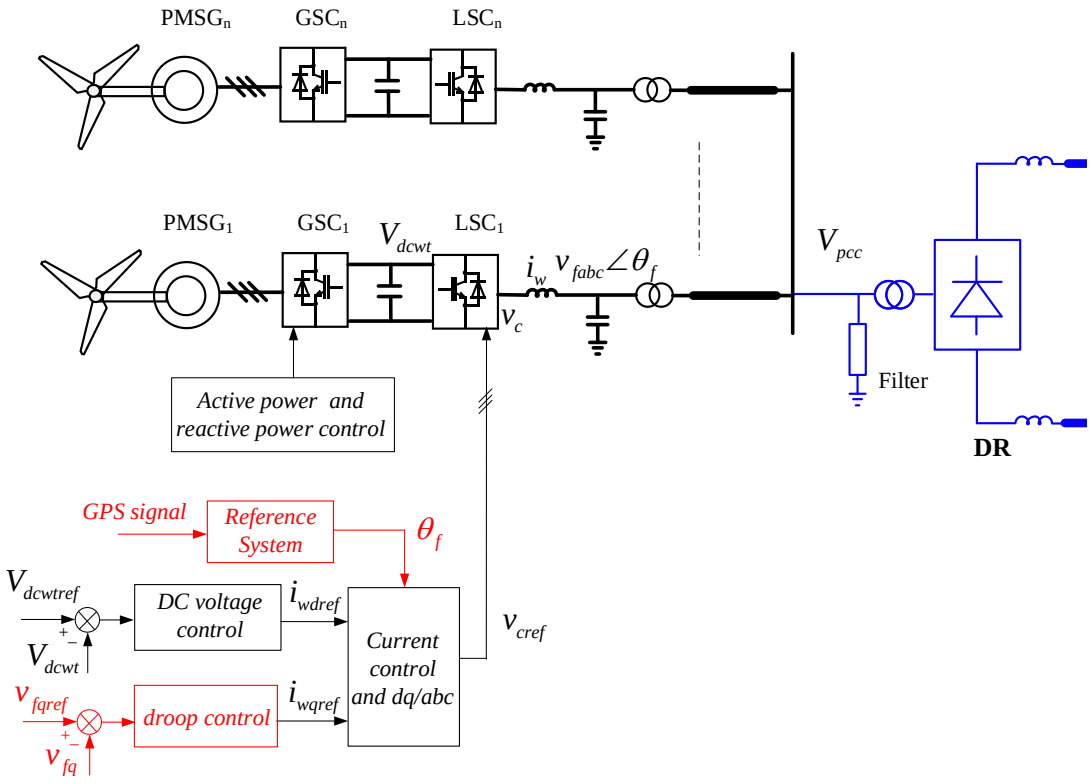

Fig. 2. 21 FixReF control of WTs connected with DR-HVDC.

References [104, 105] propose a decentralized control of offshore wind farms connected with DR-HVDC without the need of communications or the GPS, as shown in Fig. 2. 22. Active current is used to control the WT DC voltage while the reactive current is used to ensure the WT capacitor filter voltage vector is aligned with the rotating *d*-axis reference. A reactive power frequency ($Q-f$) droop control, expressed as $\omega_{ref} = k_q (Q_{wt} - Q_{wtref})$, is adopted to regulate the WT phase angle during generated WT active power change and to achieve equal reactive power sharing. However, such a control without the use of PLL may pose challenges during initial start-up as each WT has to be synchronized to the offshore network before de-blocking. Moreover, without an AC voltage control loop, it is difficult for the system to operate under low wind conditions or isolated mode when the DR-HVDC is not conducting.

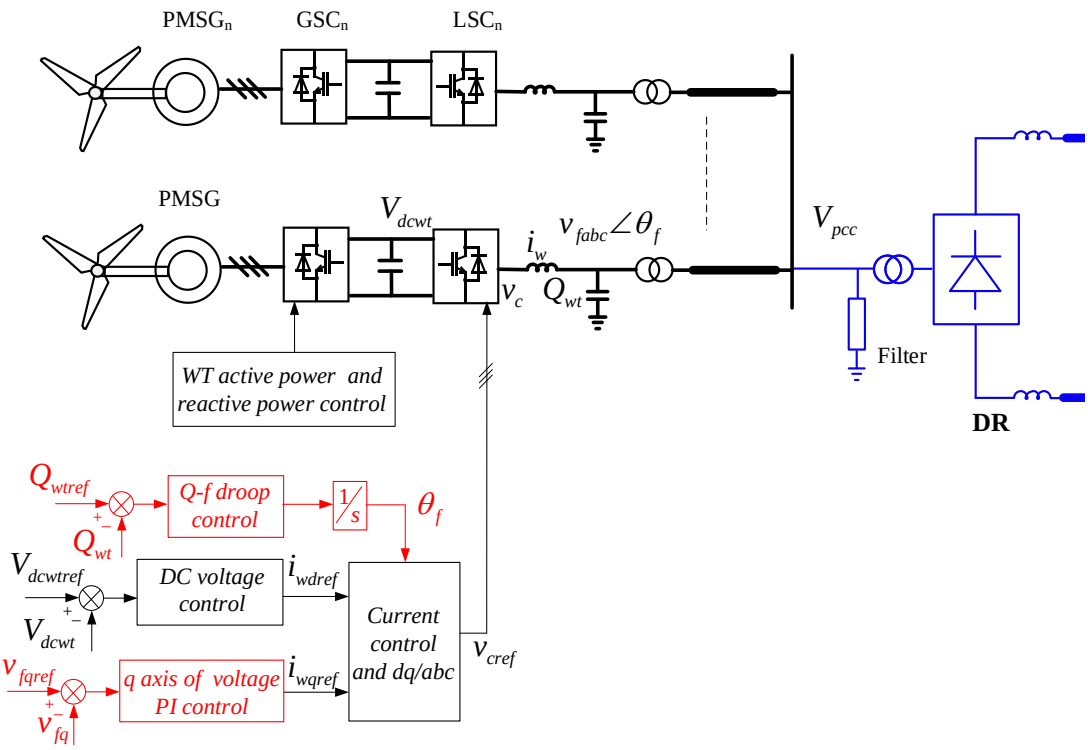

Fig. 2. 22 Control of WTs connected with DR-HVDC.

The operation of DFIGs connected with the DR-HVDC link has also been investigated in [106], where *d*-axis stator current is used to control the offshore frequency. But the reactive power sharing among the DFIGs is not addressed. Using the FixRef control for a single aggregated DFIG is studied in [107], whereas reference

[108] presents a WT control solution when DR-HVDC connects to wind farms containing mixed DFIG-WTs and FRC-WTs. *P*/*f* and *Q*/*V* droops are used for the distributed controllers of DFIG-WTs and FRC-WTs, while a centralized secondary *P*/*V* control is added in order to achieve maximum power generation.

In [109], umbilical AC cables are connected in parallel with DR-HVDC link during start-up, in order to energize the offshore network and diode rectifier, which are then disconnected during normal operation. In [110], the operation of wind farms is investigated under two different operation modes, i.e. DC mode when connected with a DR-HVDC link and AC mode when connected with a HVAC link. However, the transition between different operation modes is not detailed. With a number of DRUs connected in series, reference [111] investigates DC voltage unbalance among the DRUs, which is caused by the different distances of interconnection AC cables. A DRU DC voltage sharing control is proposed by modifying the PCC voltage magnitude. The operation of reduced DC voltage with onshore FB-MMC or hybrid MMC based on mixed HBSM and FBSM is investigated in [109], when a DRU (or some DRUs) is disconnected with the offshore wind farms.

2.7 Potential issues to be solved

Based on the review, the potential issues which have not been well addressed before are discussed in this section.

2.7.1 Synchronization issues

The reviewed research conducted has not taken the WT initial synchronization before deblocking into account. To achieve a smooth synchronization, the grid-forming WT LSC should be capable of estimating the offshore network phase angle. For the grid-connected converter, PLL is widely used as a simple and efficient tool for system synchronization. For the DR-HVDC connected WT converters, a grid forming control with the PLL can be an efficient way to tackle this issue.

2.7.2 WT level operation issues

For the DR-HVDC connected offshore wind farms (as shown in Fig. 2. 23), the DC voltage of the DR is expressed as

$$\begin{aligned} V_{dcr} &= 2.7T_{dr}\left(V_{pcc} - \frac{3X_{dr}I_{dcr}}{1.35T_{dr}\pi}\right) \\ V_{dcr} &= R_{dct}I_{dcr} + V_{dci} \\ I_{dcr} &= \frac{P_{dr}}{V_{dcr}} \end{aligned} \tag{2.1}$$

where X_{dr} and T_{dr} are the reactance and turn ration of the diode rectifier transformer, V_{dcr}, I_{dcr} and R_{dct} are the offshore DC voltage, DC current and DC resistance respectively.

Thus, the active power of DR-HVDC is rewritten as

$$P_{dr} = \frac{\left(2.7T_{dr}V_{pcc}R_{dct} + \frac{6}{\pi}X_{dr}V_{di}\right)\left(2.7T_{dr}V_{pcc} - V_{di}\right)}{(R_{dct} + \frac{6}{\pi}X_{dr})^2} \tag{2.2}$$

As can be seen, the transmitted active power P_{dr} is mainly determined by the offshore PCC voltage V_{pcc} when the onshore DC voltage V_{dci} is controlled at a constant value by MMC. This interaction between offshore PCC voltage V_{pcc} and HVDC transmitted active power P_{dr} leads to the WT *P-V* control design which is reviewed before [83, 85, 89, 91, 104]. *Q-f* control is used to ensure the reactive power consumed by the diode rectifier is well shared among the WTs.

However, when considering the power transmission from an individual WT to the offshore PCC, as shown in Fig. 2. 23, the WT active power P_{wt} and reactive power Q_{wt} is expressed as [112]

$$P_{wt} = \frac{V_{pcc} V_f \sin\theta_f}{X}$$
$$Q_{wt} = \frac{\left(V_f - V_{pcc}\cos\theta_f\right)V_f}{X} \tag{2.3}$$

where θ_f is the phase difference between the offshore PCC voltage and WT converter filter voltage and X is equivalent inductance between these two voltages (as the resistance and capacitance are much less than the sum of WT inductance and transformer leakage inductance, and thus are neglected).

As can be seen, when an individual WT transmits its active power to the PCC, the active power is mainly determined by the phase angle shift while the reactive power is mainly determined by the AC voltage magnitude.

When the *P-V* and *Q-f* control scheme is applied for each WT converter, how it affects the transmitted active and reactive power from each WT to the offshore wind farm AC network has not been properly addressed before.

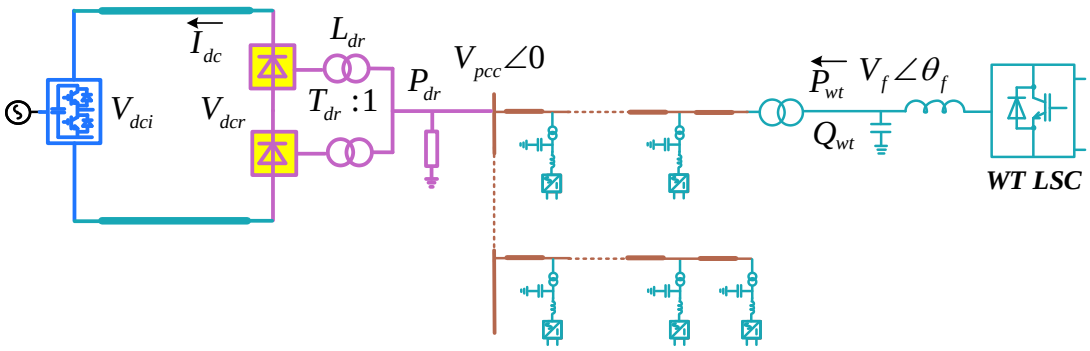

Fig. 2. 23 Offshore wind farms connected with DR-HVDC systems.

2.7.3 Fault ride-through issues

During the onshore faults, as shown in Fig. 2. 24, the onshore MMC power transmission capability is significantly reduced due to the drop of the onshore AC voltage. On the other hand, the offshore DR still tries to transfer the generated wind power to the DC link, which can lead to the overvoltage in onshore MMC submodule

capacitors and offshore overvoltage due to the active power unbalance between the DC and onshore sides. How to ensure the DR-HVDC systems can ride through the onshore fault has not been properly addressed before.

During the offshore faults, as shown in Fig. 2. 24, to ensure the WT converter current does not exceed its maximum value, the WT converter needs to operate on the current limiting mode. On the other hand, to provide the protection system with the capability of offshore fault detection, WTs should provide sufficient offshore fault current instead of reducing the currents to 0. How to ensure the DR-HVDC systems can ride through the offshore fault has not been properly addressed before.

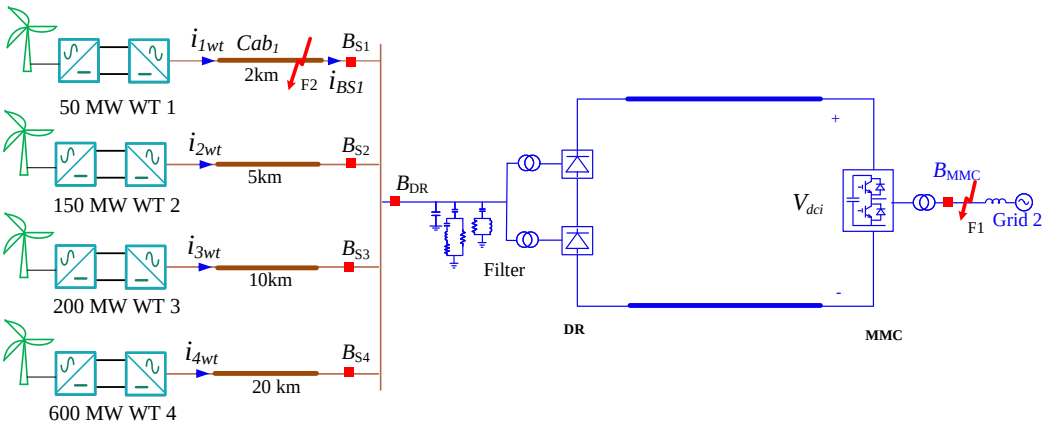

Fig. 2. 24 Onshore faults, offshore faults of the DR-HVDC systems.

2.7.4 Parallel operation issues

For the DR-HVDC connected offshore wind farms, initial energization of the offshore wind farms during the start-up is a challenge due to the unidirectional of the DR-HVDC link. Parallel operation of a DR-HVDC link with an HVAC link is a potential way to overcome this issue. How to ensure the stable operation of WTs under different transmission mode and smooth operation mode switch has not be properly addressed before.

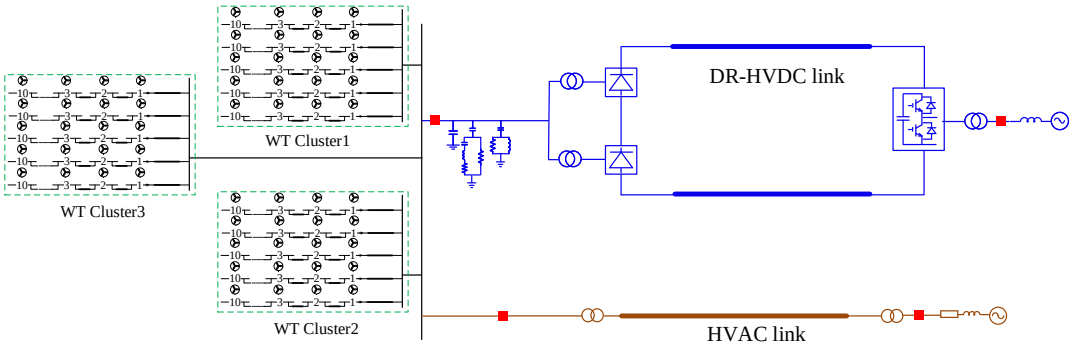

Fig. 2. 25 Parallel operation system.

2.8 Summary

HVDC for offshore wind power transmission has received noticeable interests due to its significant advantages when compared to HVAC systems. In this chapter, four offshore HVDC converter configurations, i.e. LCC-HVDC, VSC-HVDC, hybrid-HVDC and DR-HVDC are reviewed and the advantages and disadvantages are compared. Although the commercially-used HVDC technology for offshore wind power transmission is based on VSC, DR-HVDC has drawn significant attentions due to its attractive advantages of reduced investment, reduced space requirement, increased efficiency and improved reliability when compared to VSC-HVDC systems. As DR-HVDC cannot offer frequency and voltage control for the offshore network as VSC-HVDC systems do, WT control design plays a key role in the operation of DR-HVDC connected wind farms. A thorough review of DR-HVDC connected offshore wind farm systems is conducted to highlight the potential unsolved issues before, i.e. synchronization issues, WT level operation issues, fault ride-through issues and parallel operation issues.

Chapter 3 Distributed PLL-based control of offshore WTs connected with DR-HVDC systems

Due to the unique features of DR-HVDC systems, offshore WT converters are required to regulate the voltage and frequency of the offshore AC grid, and control the active power transmitted through the DR-HVDC link. This chapter proposes a distributed PLL-based control for WT converters connected with DR-HVDC, which includes a current control, voltage control, PLL based frequency control, active power control and reactive power control. With the proposed control, communication is not required and large numbers of wind turbines are able to work autonomously to contribute to offshore AC frequency and voltage regulation. This proposed control also provides synchronization for the offline wind turbines to the offshore AC grid. Simulation results in PSCAD verify the effectiveness of proposed control strategy.

3.1 Control requirements of WT converters

Fig. 3. 1 shows the structure of the considered offshore wind farms connected with DR-HVDC systems. The wind farms consist of a large number of PMSG-WTs. The DR-HVDC systems mainly comprise an offshore diode rectifier and an onshore MMC. The DR is made up of a 12-pulse bridge while the onshore MMC controls the DC voltage of the DR-HVDC link [83, 85].

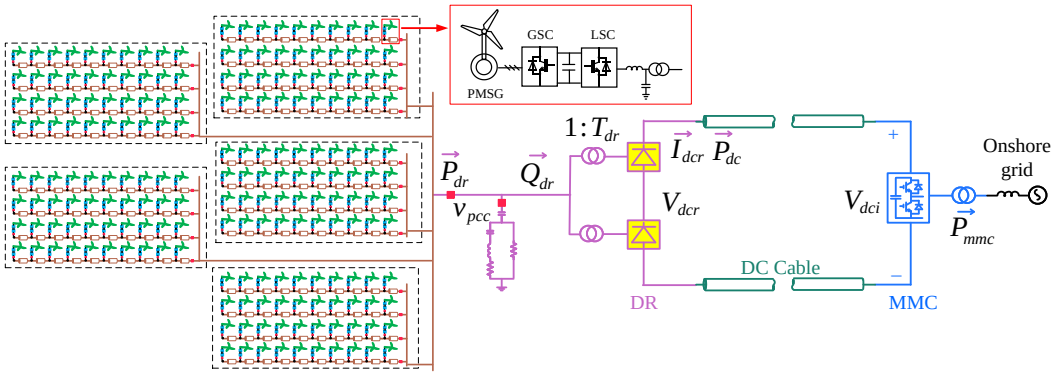

Fig. 3. 1 Diagram of the offshore wind farms connected with DR-HVDC systems.

When connected with DR-HVDC, the WT LSCs have to work as grid-forming converters rather than grid-following converters [85], as discussed in chapter 2. In addition to controlling WTs' active powers (assuming the GSCs control WT DC voltages [83, 85]), LSCs also need to establish the offshore frequency and voltage. The control functions of the WT LSCs are detailed as follows:

- AC voltage control. During the start-up and normal operation, the offshore network voltage should be established. In addition, overvoltage should be limited during transient conditions, e.g. onshore AC faults.
- Active power control. The LSCs need to control active power generation based on WT operation requirement, e.g. maximum power point tracking.
- Reactive power sharing control. Reactive power needs to be shared among WT converters while reactive current circulation among them is avoided.
- Frequency control. The LSCs need to regulate the frequency of the offshore network and ensure offline WTs can easily synchronize to the offshore AC grid.
- Current control. The LSCs should be able to ride-through various faults.

Fig. 3. 2 shows the overall structure of the proposed WT LSC control when WTs are connected with DR-HVDC systems. The detailed function and design of the individual control block will be described in the following sections.

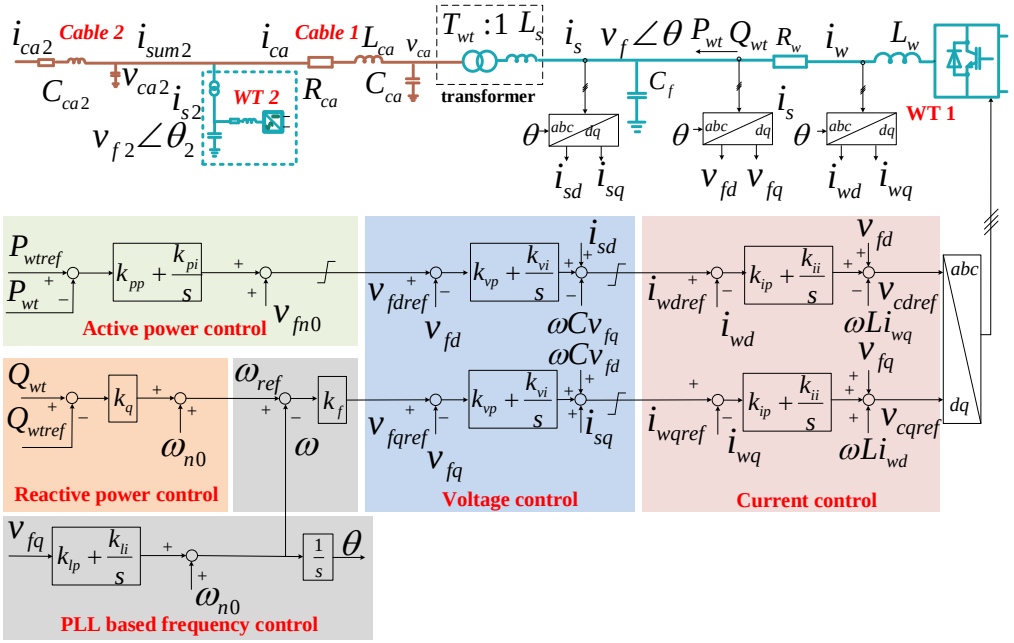

Fig. 3. 2 Diagram of WT LSC control.

3.2 Voltage and current control

The inner current loop has been widely used for controlling VSC with the benefit of fast response and current limit during external AC faults [20, 61]. For the converter circuit shown in Fig. 3. 3, the VSC current dynamics in the *dq* reference frame in which the VSC filter bus voltage is aligned with the rotating *d*-axis reference, are expressed as

$$R_w i_{wd} + L_w \frac{di_{wd}}{dt} = v_{cd} - v_{fd} + \omega L_w i_{wq} \tag{3.1}$$

$$R_w i_{wq} + L_w \frac{di_{wq}}{dt} = v_{cq} - v_{fq} - \omega L_w i_{wd} \tag{3.2}$$

where ω is the angular frequency of the offshore network. Using proportional-integral (PI) regulators, the current control loop is illustrated in Fig. 3. 3. The maximum and minimum *dq* current references are set according to converter current rating, in order to limit the fault current, which will be further detailed in chapter 4.

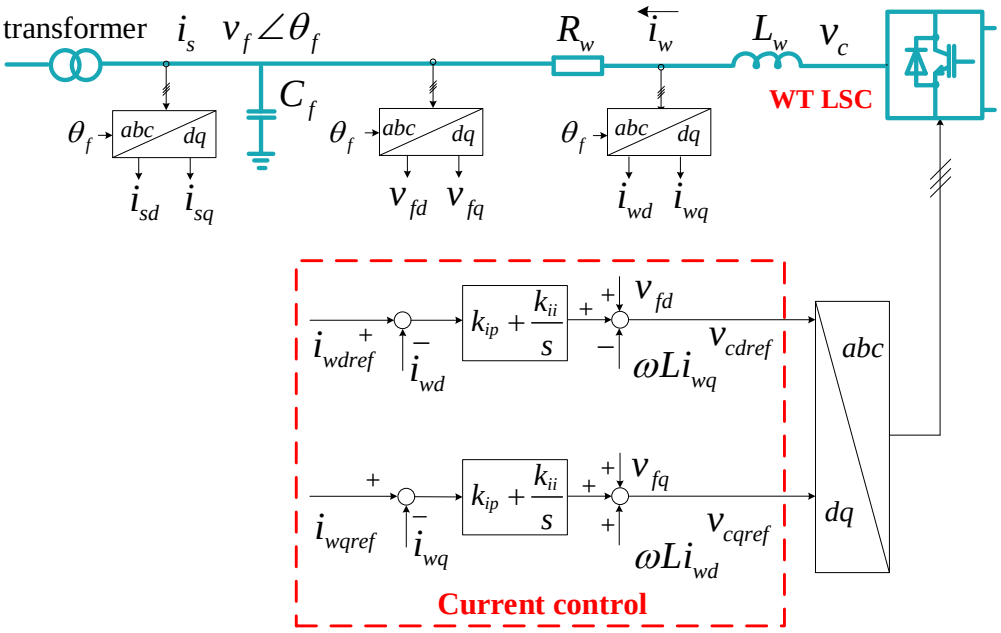

Fig. 3. 3 Diagram of current control.

On the other hand, the voltage dynamics of the WT LSC in the *dq* reference frame are described as

$$C_f \frac{dv_{fd}}{dt} = i_{wd} - i_{sd} + \omega C_f v_{fq} \tag{3.3}$$

$$C_f \frac{dv_{fq}}{dt} = i_{wq} - i_{sq} - \omega C_f v_{fd} \tag{3.4}$$

By regulating the converter output current, the voltage at the VSC filter capacitor terminal v_f can be controlled to follow its reference. The control diagram of the voltage loop is shown in Fig. 3. 4. The maximum *d*-axis voltage references are set in order to limit the offshore overvoltage, which will be further detailed in chapter 4.

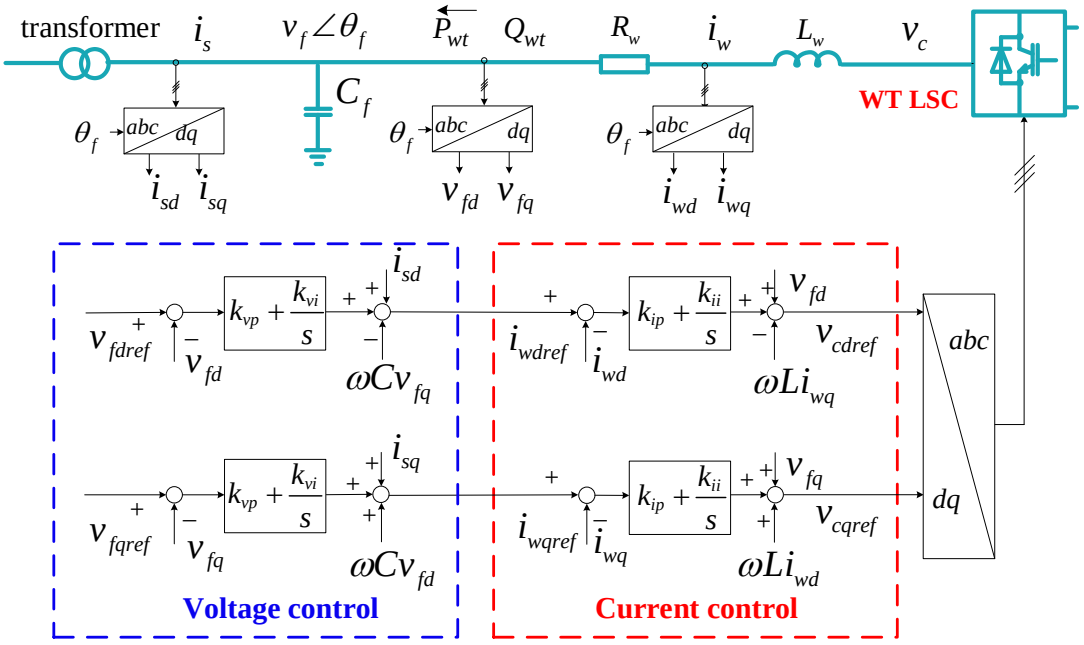

Fig. 3. 4 Diagram of voltage control.

3.3 Distributed PLL-based frequency control

Due to the uncontrollability of the diode rectifier, the system needs to ensure that large numbers of WTs work autonomously to provide frequency control for the offshore system. To tackle this problem, a distributed PLL-based frequency control is

proposed for each turbine LSC, as illustrated in Fig. 3. 5. In addition to frequency controllability, the proposed control ensures plug-and-play capability, providing automatic synchronization of offline WTs and minimum impact during disconnection of turbines from the offshore AC network. Such issues have not been considered previously [83, 85, 98, 101, 104].

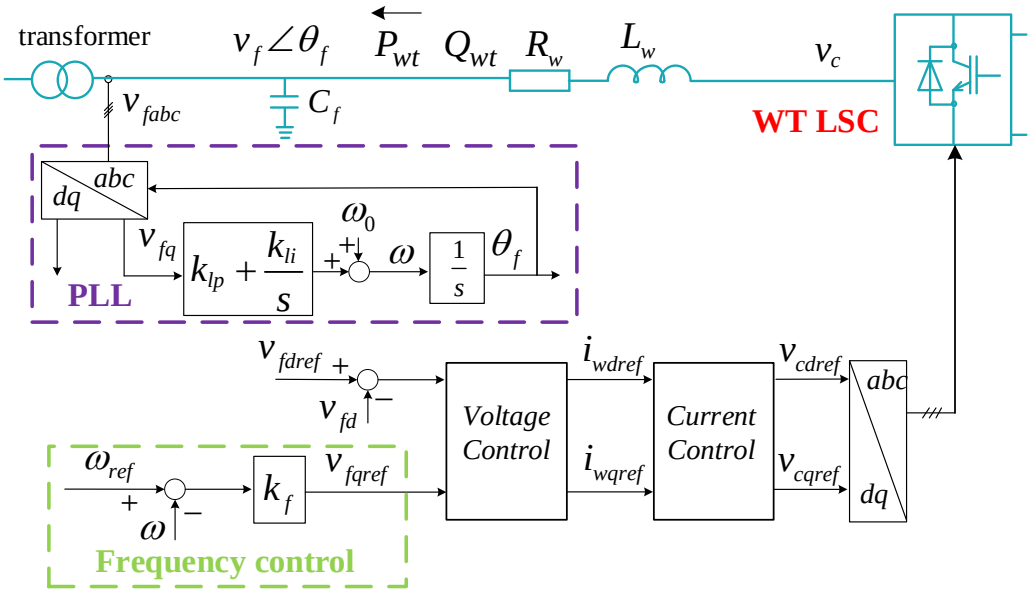

Fig. 3. 5 Diagram of PLL-based frequency control.

In the existing voltage control for converter based isolated networks, the voltage amplitude of the network is regulated by the *d*-axis voltage reference v_{fdref} while the *q*-axis reference v_{fqref} is normally set at zero [112-114]. On the other hand, the PLL takes v_{fq} as the input and regulates the frequency output to ensure the *q*-axis voltage v_{fq} to zero [113], as shown in Fig. 3. 5. For example, if the measured v_{fq} is slightly larger than zero as shown in Fig. 3. 6, the detected frequency of the voltage vector will increase as

$$\omega = k_{lp} v_{fq} + k_{li} \int v_{fq} dt + \omega_0 \tag{3.5}$$

Since the frequency and phase angle measured by the PLL will also drive (synchronize) the output of the converter connected to the offshore AC network, the frequency of the offshore system will increase under such conditions. This indicates

that the q-axis voltage reference v_{fqref} can be used to control the offshore AC frequency and thus an additional PLL-based frequency loop, as shown in Fig. 3. 5, is proposed to generate the desired v_{fqref}, as

$$v_{fqref} = k_f \left(\omega_{ref} - \omega \right) \tag{3.6}$$

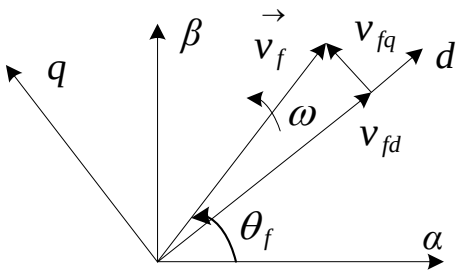

Fig. 3. 6 Voltage vector in dq reference frame

When $\omega < \omega_{ref}$ (i.e. $v_{fqref} > 0$), the PLL-based frequency control produces a positive v_{fqref} feeding to the AC voltage controller, as seen in Fig. 3. 5. The voltage and current loops ensure the converter to generate the required v_{fq} according to its reference value produced by the frequency loop. Consequently, the frequency measured by the PLL is increased (due to $v_{fq} > 0$) until it becomes identical to the reference ($\omega = \omega_{ref}$). Similarly, when $\omega > \omega_{ref}$ (i.e. $v_{fqref} < 0$), the proposed frequency control produces a negative v_{fq} so the frequency is reduced accordingly. Such frequency control can be implemented at each WT LSC and is able to operate autonomously to contribute to the overall frequency regulation of the offshore AC network.

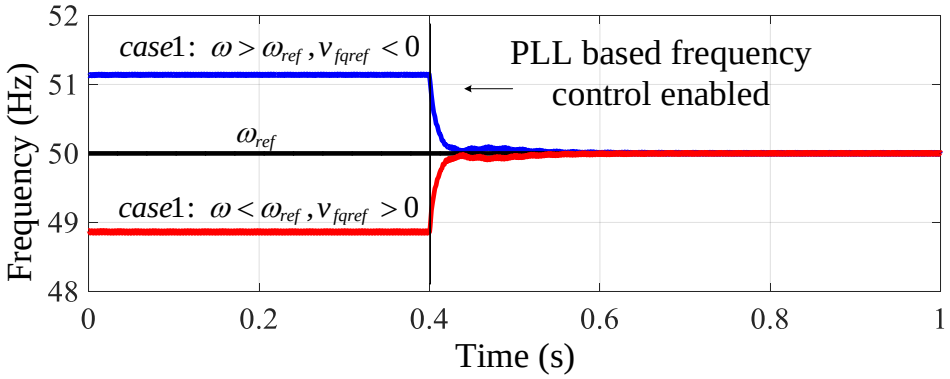

Fig. 3. 7 Frequency regulation using the proposed PLL-based frequency control.

Fig. 3. 7 shows the frequency regulation of the proposed PLL-based frequency control enabled at 0.4 s for a 5 MW converter. For case 1, the initial frequency is higher than the reference frequency of 50 Hz, whereas for case 2, it is lower than 50 Hz. As can be seen, both frequencies quickly follow the reference after enabling the proposed frequency control at 0.4 s (k_f steps from 0 to 0.01skV/rad).

3.4 Active power control and reactive power sharing control

As the DC voltage of the DR-HVDC link is controlled at the rated value by the onshore MMC, the transmitted active power is largely determined by the DC voltage produced by the diode rectifier (V_{dcr}, Fig. 3. 1). The DC voltage produced by the diode rectifier is given as [83]

$$V_{dcr} = 2(1.35T_{dr}V_{pcc} - \frac{3}{\pi}X_{dr}I_{dcr}) \tag{3.7}$$

where T_{dr} and X_{dr} are the turn ratio and reactance of the diode rectifier transformer. Thus, the active power transmitted from the wind farms to the onshore converter is mainly determined by the offshore AC grid voltage V_{pcc}. Therefore, a WT active power control loop can be implemented as shown in Fig. 3. 8, whose output is the amplitude of the *d*-axis voltage reference, i.e. magnitude of the produced offshore AC voltage. v_{f0} is the AC voltage set point of the offshore WT converters.

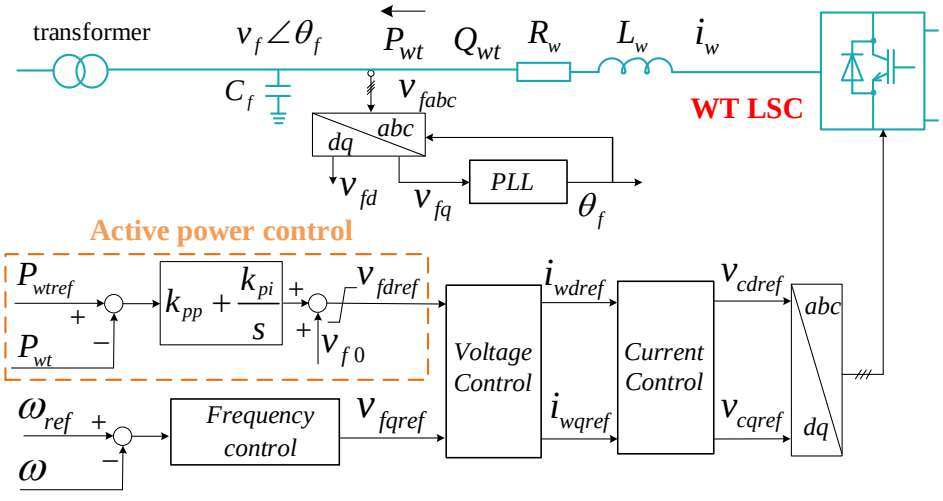

Fig. 3. 8 Diagram of active power control.

When a large number of WTs are connected to DR-HVDC, the reactive power needs to be shared among the WTs to avoid overcurrent and reactive current circulation. As AC voltage is selected as the control variable to regulate the WT active power, reactive power / frequency droop control shown in Fig. 3. 9 is designed. Such droop control ensures steady state reactive power to be shared among WT converters due to the same steady state frequency across the whole offshore network. The adopted reactive power sharing control is expressed as

$$\omega_{ref} = k_q \left(Q_{wt} - Q_{wtref} \right) + \omega_0 \tag{3.8}$$

If Q_{wt} is represented as per unit value (positive Q_{wt} defined as WTs providing capacitive reactive power to the offshore AC network) where the power rating of the respective WT is used as the based power, same k_q and Q_{wtref} can be used for all the WTs to achieve equal reactive power sharing (based on their respective power rating). Q_{wtref} can be set according to the system operation requirements. In this thesis, Q_{wtref} is set at 0 to ensure that each WT exported or absorbed reactive power is 0 when the DR-HVDC systems operates at the rated power.

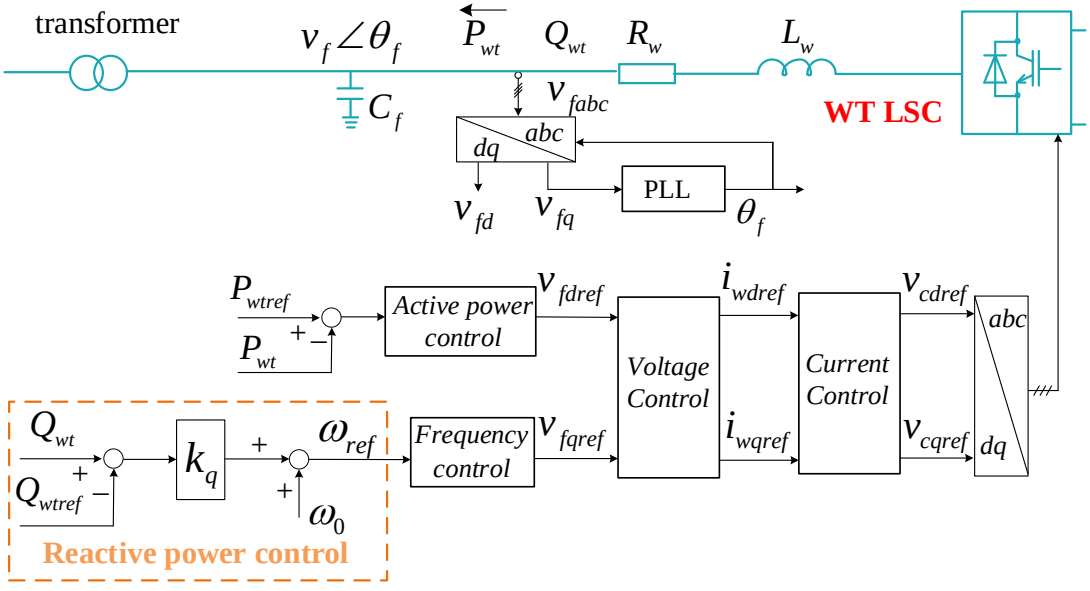

Fig. 3. 9 Diagram of reactive power control.

3.5 Simulation results

The systems shown in Fig. 3. 10 are simulated in PSCAD/EMTDC to verify the proposed control of the DR-HVDC systems during the start-up, with parameters listed in Table 3. 1. Detailed model is used for the diode rectifier while the equivalent MMC model from PSCAD library containing 256 submodules per arm is used for the onshore inverter [115-117]. The wind farm model includes the followings: ten 5 MW WTs representing one WT string, an aggregate 150 MW WT (equivalent to 3 WT strings), an aggregate 200 MW WT (equivalent to a WT cluster with 4 strings) and an aggregate 600 MW WT (equivalent to 3 WT clusters). WTs' mechanical parts, GSCs, transformers' shunt branches and inrush currents are not modelled [83, 85] while the LSCs use detailed switching models and are connected to constant DC voltage sources.

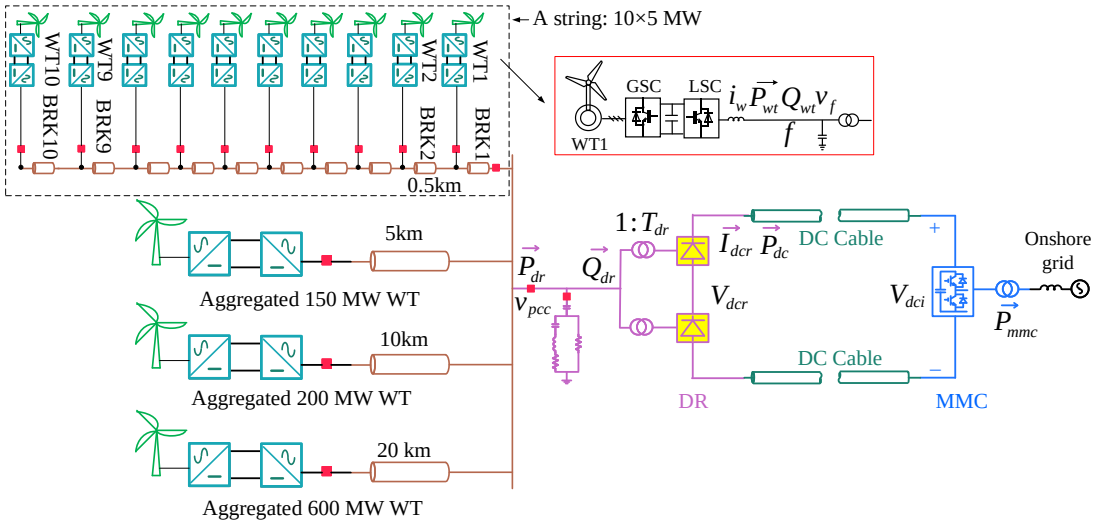

Fig. 3. 10 Diagram of the tested systems for start-up.

Table 3. 1 Parameters of the tested DR-HVDC systems for start-up

Components	Parameters	Values
DR-HVDC link	Power	1000 MW
	DC voltage	±320 kV
12-pulse diode rectifier	Transformer (Y/Y/Δ)	66/261.8/261.8 kV,
	Leakage inductance	0.18 pu

	Reactive power compensation	0.3 pu
Onshore MMC	Submodule capacitance	8000 uF
	Submodule number per arm *N*	256
	Submodule capacitor voltage	2.5 kV
	Arm inductance	0.067 pu
	Transformer (Y/Δ)	400/330 kV
WT converters	Rating of individual WT	5 MW
	Rating of a WT string	5 MW×10
	Rating of a WT cluster	200 MW
	Transformer (Y/Δ) Leakage inductance	0.69/66 kV 0.08 pu
	Filter capacitor C Filter resistance	0.1pu 0 pu
	Converter reactance *L*	0.15 pu
	DC voltage	1.1 kV
	Switching frequency	2 kHz
	AC cable length between two 5MW WTs	0.5 km
	AC cable length (for each aggregate converter)	5 km, 10 km, 20 km

The performances of WTs connected with DR-HVDC systems during start-up are illustrated in Fig. 3. 11, with the assumption that the WT DC link initial energy is provided by WT internal energy storage. The time line of the simulation is listed in Table 3. 2.

Table 3. 2 Sequence of start-up

Time	**Events**
0s	Breaker BRK1 (seen in Fig. 3. 10) is closed.
0-0.5s	WT1 establishes AC voltage and frequency, operating in islanded mode.
1.0s	Breaker BRK2 closed, WT2 filter and transformer energized.

1.2s	WT2 enabled, operating in islanded mode.
…	…
9s	Breaker BRK10 closed, WT10 filter and transformer energized.
9.2s	WT10 enabled, operating in islanded mode.
10s	Breaker of the aggregated 150 MW WT closed, filter and transformer of WT energized.
10.2s	Aggregated 150 MW WT enabled, operating in islanded mode.
11s	Breaker of the aggregated 200 MW WT closed, filter and transformer of WT energized.
11.2s	Aggregated 200 MW WT enabled, operating in islanded mode.
12s	Diode rectifier and transformer energized and connected, 150 MVAr filter connected and energized.
12.5-12.8s	WT1 starts power production.
13-13.3s	WT2 starts power production.
13.5-13.8s	WT3 starts power production.
14-14.3s	WT4--WT10 starts power production.
14.5-14.8s	Aggregated 150 MW WT starts power production.
15-15.3s	Aggregated 200 MW WT starts power production.
15.5s	Breaker of aggregate 600 MW WT closed.
16-16.3s	Aggregated 600 MW WT enabled and increase power production to 300 MW.
16.5s	A 150 MVAr diode rectifier filter added.
17-17.3s	Aggregated 600 MW WT increases power production from 300 MW to 600 MW.

At the beginning, the first 5 MW WT1 (seen in Fig. 3. 10) is connected to its WT string, while the DR-HVDC DC link voltage is established by the onshore MMC. During 0-0.5 s, the voltage and frequency control of WT1 increases its output AC voltage (v_{f1}) and the offshore voltage (v_{pcc}) to 0.86 pu with AC frequency at 50Hz, as shown in Fig. 3. 11 (a), (h) and (g). At 1 s, breaker BRK2 is closed to connect WT2 to the WT string, with the WT2 filter and transformer being energized.

At 1.2 s, the proposed PLL-based control enables WT2 to synchronize automatically with the WT string. As seen from Fig. 3. 11 (c) and (d), each WT active power output is around 0 (only needs compensate the power loss of the cables) while reactive power is shared between these two WTs (-0.33 MVAr each). During 2-9.2 s, WT3--WT10 are enabled and synchronized with the WT string sequentially after closing each AC breaker. As seen in Fig. 3. 11 (b), no overcurrent is observed during the WT connection and synchronization.

At 10 s, the breaker of the aggregated 150 MW WT (equivalent to 3 WT strings) is closed and the corresponding WT filter and transformer are energized. At 10.2 s, the 150 MW WT is enabled and synchronized with the offshore network. At 11 s, the breaker of the aggregated 200 MW WT (equivalent to a WT cluster) is closed to energize the corresponding WT filter and transformer, and at 11.2 s, the 200 MW WT is enabled and synchronized with the offshore network. As can be seen in Fig. 3. 11 (a), (b), (g) and (h), the synchronization is very smooth even with such large lumped converters and the offshore AC voltage and frequency are well controlled.

At 12 s, the breaker of the diode rectifier is closed. Thus, the diode rectifier, transformer and the 150 MVAr filter are energized. From 12.5 s to 12.8 s, first WT starts power production, ramping active power from 0 to its rated value of 5 MW as seen in Fig. 3. 11 (c). After the conduction of the diode rectifier, the offshore AC voltage increases to 0.9 pu in order to transmit active power. From 13 s to 13.3 s and 13.5 s to 13.8 s, WT2 and WT3 increase active power production to its rated value respectively. From 14-14.3 s, WT4-WT10 increase active power production to rated value at the same time. After 14.3 s, all the ten WTs in this string operate at the rated active power, with the offshore frequency being regulated at around 50 Hz and reactive power well shared among the WTs (-1.8 MVAr each).

During 14.5-14.8 s, the generated active power from the aggregated 150 MW WT increases from 0 to 150 MW, as shown in Fig. 3. 11 (e). Meanwhile, the diode rectifier reactive power consumption grows to 33 MVAr, as shown in Fig. 3. 11 (j). During 15-15.3 s, the generated active power from the aggregated 200 MW WT increases from 0 to 200 MW with the growth of diode rectifier reactive power consumption to 97

MVAr. As a result, the reactive power absorbed by the WTs decreases accordingly to achieve the offshore network reactive power balance, as shown in Fig. 3. 11 (d) and (f). When these WTs operate at the full rated power (at t=15.3 s in Fig. 3. 11), the total transmitted active power is 400 MW, as shown in Fig. 3. 11 (i) and the offshore voltage V_{pcc} is increased to 0.94 pu with frequency largely remained at 50 Hz.

At 15.5 s, the breaker of the aggregate 600 MW WT (equivalent to 3 WT clusters) is closed and the corresponding WT filter and transformer are energized. During 16-16.3 s, its output power is increased from 0 to 300 MW. Meanwhile, all the WTs start to export reactive power to compensate the increased reactive power consumption by the diode rectifier (227 MVAr). At 16 s, a 150 MVAr filter is added. During 17-17.3 s, the aggregated 600 MW WT further increases its active power from 300 MW to 600 MW.

From 17.3 s, the DR-HVDC system operates at the rated active power with DC current and onshore active power at rated value, as shown in Fig. 3. 11 (l) and (k). The offshore voltage V_{pcc} is now approximately 1 pu and frequency controlled at around 50 Hz. The diode rectifier consumes 400 MVAr reactive power. As can be seen from Fig. 3. 11 (d) and (f), under steady state, the reactive power is shared equally (in per unit terms with respect to their respective rated power) among the WTs. During the whole start-up and WT connection process, the DC voltage is well controlled by the onshore MMC, as shown in Fig. 3. 11 (m). The total harmonic distortion (THD) of the offshore voltage V_{pcc} is lower than 1.5% throughout the wind power range of 0 to 1 pu, as shown in Table 3. 3.

As seen from Fig. 3. 11, the offshore network shows an excellent behaviour during the start-up and synchronization. Offline WT converters synchronize seamlessly with the offshore network during the connection process, and the overall offshore network frequency is also well controlled by the distributed WT converters.

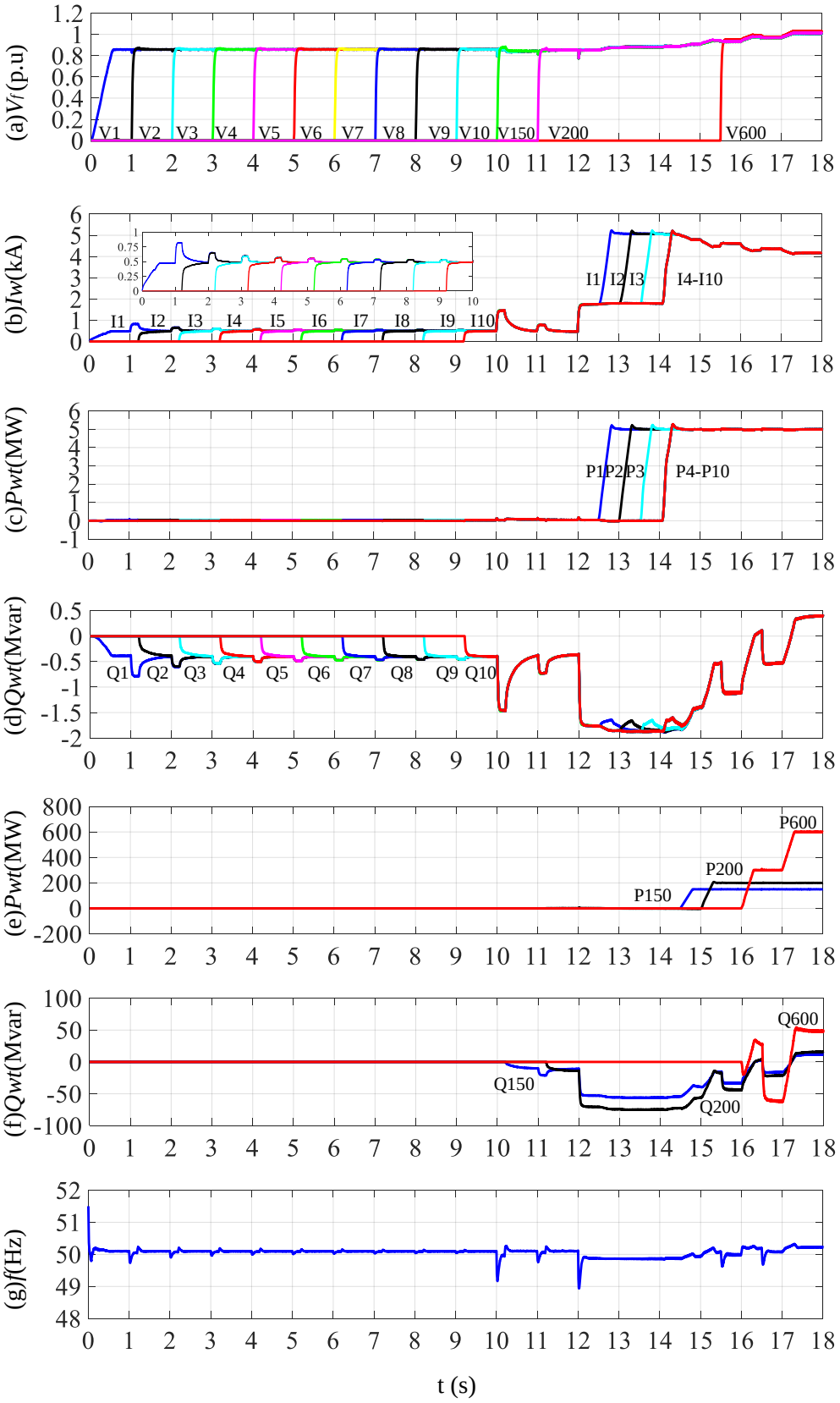
(a)Vf(p.u)
V1
V2
V3
V4
V5
V6
V7
V8
V9
V10
V150
V200
V600
(b)Iw(kA)
I1
I2
I3
I4
I5
I6
I7
I8
I9
I10
I1
I2
I3
I4-I10
(c)Pwt(MW)
P1
P2
P3
P4-P10
(d)Qwt(Mvar)
Q1
Q2
Q3
Q4
Q5
Q6
Q7
Q8
Q9
Q10
(e)Pwt(MW)
P600
P200
P150
(f)Qwt(Mvar)
Q600
Q150
Q200
(g)f(Hz)
t (s)

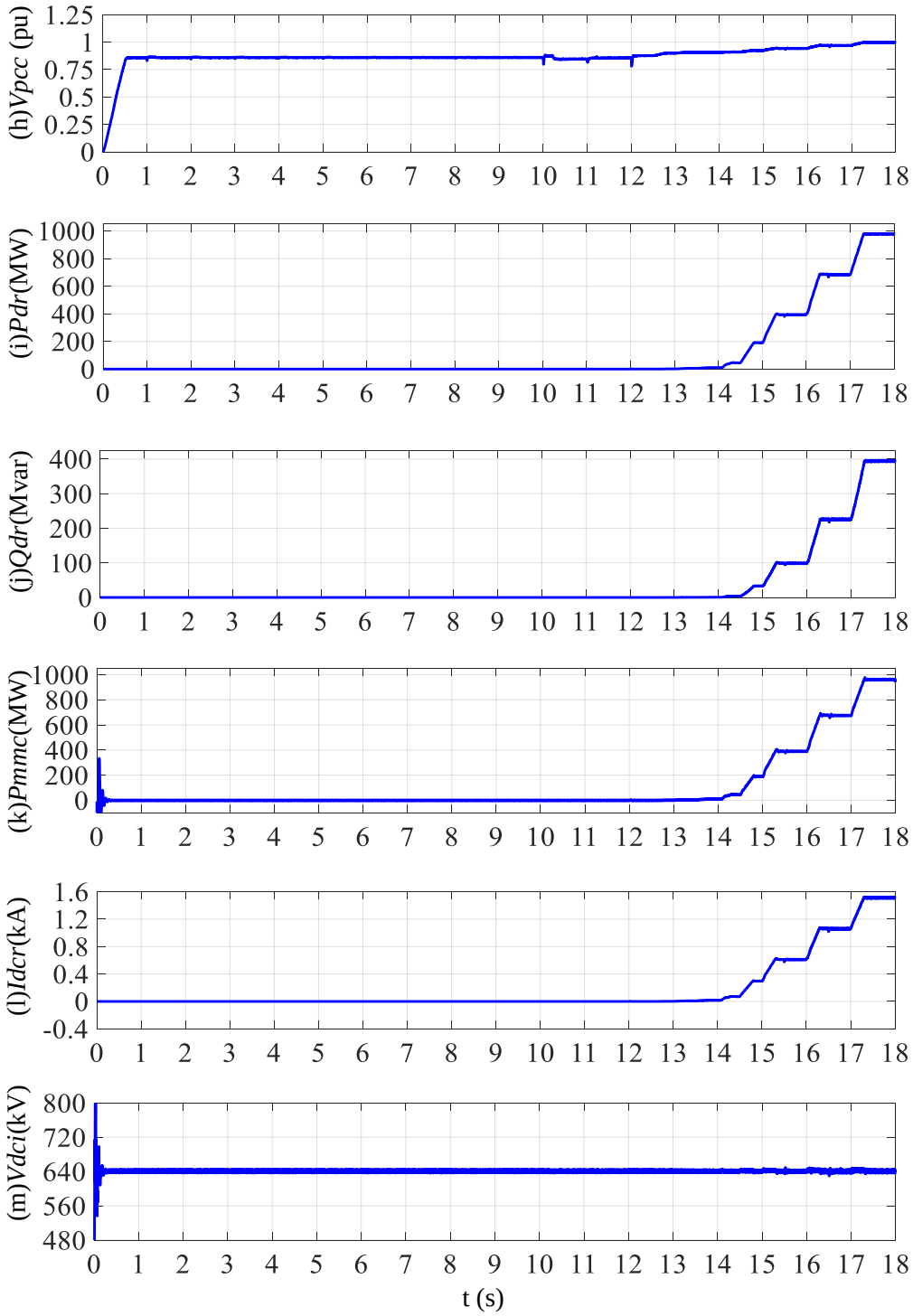

Fig. 3. 11 Performance of start-up and synchronization: (a) WT voltage (RMS); (b) WT current (RMS); (c) WT active power; (d) WT reactive power; (e) aggregated WT power;(f) aggregated WT reactive power; (g) offshore frequency; (h) offshore voltage; (i) diode rectifier transmitted active power; (j) diode rectifier reactive power consumption; (k) onshore transmitted active power; (l) DC current; (m) DC voltage.

Table 3. 3 THD of the offshore voltage at PCC

Power (pu)	0	0.1	0.2	0.3	0.4	0.5
THD	0.55%	0.68%	0.7%	0.8%	0.9%	1.37%
Power (pu)	0.6	0.7	0.8	0.9	1.0	
THD	1.06%	1.1%	0.84%	0.96%	1.1%	

3.6 Summary

This chapter proposes a distributed control of WT LSC for offshore wind farms connected with DR-HVDC system, which includes the current control, voltage control, PLL-based frequency control, WT active power and reactive power control. The proposed method uses an additional PLL-based frequency loop to set the reference of the *q*-axis voltage for frequency regulation. The proposed control enables each WT converter to operate as a grid-forming source and autonomously contribute to the overall offshore voltage and frequency regulation, which provides WTs with plug-and-play capability for synchronizing offline WTs to the offshore network. Simulation results in PSCAD/EMTDC during system start-up and WT synchronization verify the voltage, frequency and power controllability and plug-and-play feature of WTs with the proposed control.

Chapter 4 Small-signal analysis of offshore wind farms connected with DR-HVDC systems

This chapter develops a small-signal state-space model of WTs connected with DR-HVDC systems, where the detailed sub-section models of the complete systems are presented. Based on the small-signal model, the wind farm level analysis is conducted to investigate the interactions among active and reactive powers, offshore AC voltage and frequency. The WT level analysis is carried out to reveal the mechanism when each individual WT transmits power to offshore AC network and the coupling between WT active power and reactive power, with the adopted *P*-*V* and *Q*-*f* control scheme. In order to reduce the coupling between WT active power and reactive power, an angle compensation control is proposed where an additional phase shift is directly added to the WT output voltage based on its active power output. The effectiveness of the proposed control is verified by frequency domain analysis in Matlab and time domain simulations in PSCAD/EMTDC. Finally, the stability of the proposed control during variations of different parameters is analysed using the developed small-signal model.

4.1 Small-signal model of WTs connected with DR-HVDC

In order to conduct the stability analysis, the 1000 MW DR-HVDC connected offshore wind farm systems, which consists of 40 aggregated WTs (each rated at 25 MW), AC cables, diode rectifier filters, diode rectifier, HVDC cables (all shown in Fig. 4. 1) and the distributed control of WT LSC (shown in Fig. 4. 2), are linearized at an operation point based on *dq* rotating reference.

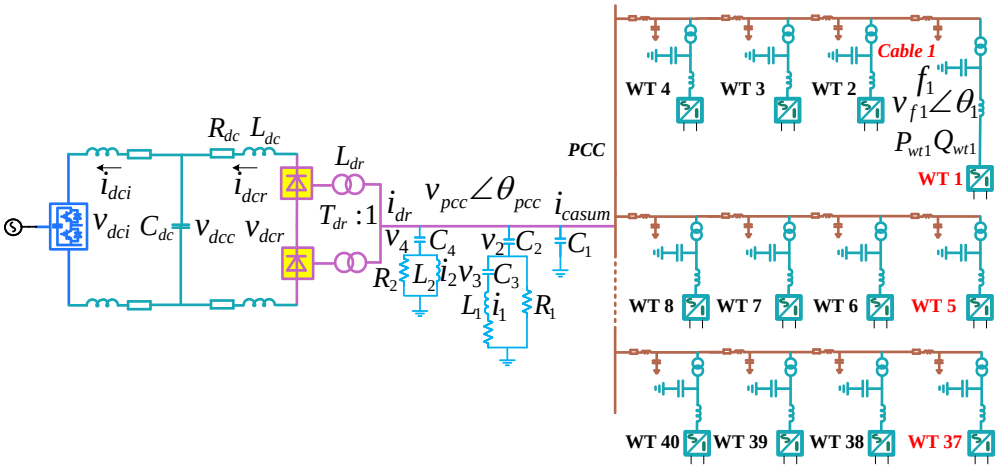

Fig. 4. 1 Structure of offshore wind farms connected with DR-HVDC.

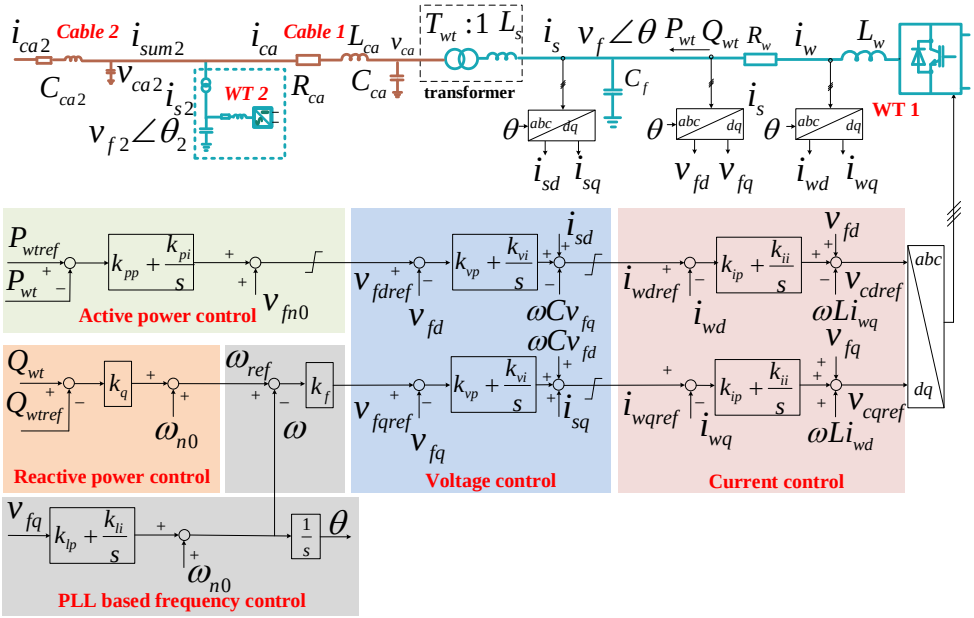

Fig. 4. 2 Distributed control of WT LSCs connected with DR- HVDC.

4.1.1 Small-signal model of WT LSC control

As presented in chapter 3 and shown in Fig. 4. 2, WT LSC control includes current control, voltage control, PLL based frequency control, active power and reactive power control. The small-signal model of each control is derived in this sub-section.

A. Current control

The current control as shown in Fig. 4. 2 is expressed as

$$\begin{cases} v_{cdref} = k_{ip}\left(i_{wdref} - i_{wd}\right) + k_{ii}\int\left(i_{wdref} - i_{wd}\right)dt - \omega L_w i_{wq} + v_{fd} \\ v_{cqref} = k_{ip}\left(i_{wqref} - i_{wq}\right) + k_{ii}\int\left(i_{wqref} - i_{wq}\right)dt + \omega L_w i_{wd} + v_{fq} \end{cases}. \tag{4.1}$$

Defining new states as [112]

$$\begin{aligned} \frac{d\gamma_{\_iwd}}{dt} &= i_{wdref} - i_{wd} \\ \frac{d\gamma_{\_iwq}}{dt} &= i_{wqref} - i_{wq} \end{aligned} \tag{4.2}$$

the linearized small-signal state space form of the current control is described as

$$\begin{bmatrix} \dot{\Delta\gamma}_{\_iwd} \\ \dot{\Delta\gamma}_{\_iwq} \end{bmatrix} = \begin{bmatrix} 0 & 0 \\ 0 & 0 \end{bmatrix}\begin{bmatrix} \Delta\gamma_{\_iwd} \\ \Delta\gamma_{\_iwq} \end{bmatrix} + \begin{bmatrix} 1 & 0 & -1 & 0 & 0 & 0 \\ 0 & 1 & 0 & -1 & 0 & 0 \end{bmatrix}\begin{bmatrix} \Delta i_{wdref} \\ \Delta i_{wqref} \\ \Delta i_{wd} \\ \Delta i_{wq} \\ \Delta v_{fd} \\ \Delta v_{fq} \end{bmatrix} \tag{4.3}$$

$$\begin{aligned} \begin{bmatrix} \Delta v_{cdref} \\ \Delta v_{cqref} \end{bmatrix} &= \begin{bmatrix} k_{ii} & 0 \\ 0 & k_{ii} \end{bmatrix}\begin{bmatrix} \Delta\gamma_{\_iwd} \\ \Delta\gamma_{\_iwq} \end{bmatrix} \\ &+ \begin{bmatrix} -L_w i_{wq0} & k_{ip} & 0 & -k_{ip} & -\omega_0 L_w & 1 & 0 \\ L_w i_{wd0} & 0 & k_{ip} & \omega_0 L_w & -k_{ip} & 0 & 1 \end{bmatrix}\begin{bmatrix} \Delta\omega \\ \Delta i_{wdref} \\ \Delta i_{wqref} \\ \Delta i_{wd} \\ \Delta i_{wq} \\ \Delta v_{fd} \\ \Delta v_{fq} \end{bmatrix}. \end{aligned} \tag{4.4}$$

B. Voltage control

The voltage control as shown in Fig. 4. 2 is expressed as

$$\begin{cases} i_{wdref} = k_{vp}\left(v_{fdref} - v_{fd}\right) + k_{vi}\int\left(v_{fdref} - v_{fd}\right)dt - \omega C_f v_{fq} + i_{sd} \\ i_{wqref} = k_{vp}\left(v_{fqref} - v_{fq}\right) + k_{vi}\int\left(v_{fqref} - v_{fq}\right)dt + \omega C_f v_{fd} + i_{sq} \end{cases} . \quad (4.5)$$

Defining

$$\begin{aligned} \frac{d\gamma_{\_vfd}}{dt} &= v_{fdref} - v_{fd} \\ \frac{d\gamma_{\_vfq}}{dt} &= v_{fqref} - v_{fq} \end{aligned} \quad (4.6)$$

the linearized small-signal state space form of the voltage control is described as

$$\begin{bmatrix} \dot{\Delta\gamma}_{\_vfd} \\ \dot{\Delta\gamma}_{\_vfq} \end{bmatrix} = \begin{bmatrix} 0 & 0 \\ 0 & 0 \end{bmatrix}\begin{bmatrix} \Delta\gamma_{\_vfd} \\ \Delta\gamma_{\_vfq} \end{bmatrix} + \begin{bmatrix} 1 & 0 & -1 & 0 & 0 & 0 \\ 0 & 1 & 0 & -1 & 0 & 0 \end{bmatrix}\begin{bmatrix} \Delta v_{fdref} \\ \Delta v_{fqref} \\ \Delta v_{fd} \\ \Delta v_{fq} \\ \Delta i_{sd} \\ \Delta i_{sq} \end{bmatrix} \quad (4.7)$$

$$\begin{bmatrix} \Delta i_{wdref} \\ \Delta i_{wqref} \end{bmatrix} = \begin{bmatrix} k_{vi} & 0 \\ 0 & k_{vi} \end{bmatrix}\begin{bmatrix} \Delta\gamma_{\_vfd} \\ \Delta\gamma_{\_vfq} \end{bmatrix} + \begin{bmatrix} -C_f v_{fq0} & k_{vp} & 0 & -k_{vp} & -\omega_0 C_f & 1 & 0 \\ C_f v_{fd0} & 0 & k_{vp} & \omega_0 C_f & -k_{vp} & 0 & 1 \end{bmatrix}\begin{bmatrix} \Delta\omega \\ \Delta v_{fdref} \\ \Delta v_{fqref} \\ \Delta v_{fd} \\ \Delta v_{fq} \\ \Delta i_{sd} \\ \Delta i_{sq} \end{bmatrix} . \quad (4.8)$$

C. PLL based frequency control

The PLL based frequency control as shown in Fig. 4. 2 is expressed as

$$v_{fqref} = k_f\left(\omega_{ref} - k_{lp}v_{fq} - k_{li}\int v_{fq}dt - \omega_{n0}\right) . \quad (4.9)$$

Setting

$$\frac{d\gamma_{\_pll}}{dt} = v_{fq} \quad (4.10)$$

the linearized small-signal state space form of the PLL based frequency control can be described as

$$\dot{\Delta\gamma}_{\_pll} = 0 \cdot \Delta\gamma_{\_pll} + \Delta v_{fq} \tag{4.11}$$

$$\Delta v_{fqref} = -k_f k_{li} \Delta\gamma_{\_pll} + \begin{pmatrix} k_f & -k_f k_{lp} \end{pmatrix} \begin{pmatrix} \Delta\omega_{ref} \\ \Delta v_{fq} \end{pmatrix} . \tag{4.12}$$

D. Active power control

The active power control in Fig. 4. 2 is expressed as

$$v_{fdref} = k_{pp} \left(P_{wtref} - P_{wt} \right) + k_{pi} \int \left(P_{wtref} - P_{wt} \right) dt + v_{fn0} \tag{4.13}$$

where the instantaneous active power P is expressed as

$$P_{wt} = 1.5(v_{fd} i_{wd} + v_{fq} i_{wq}) . \tag{4.14}$$

Linearizing (4.14) yields the expression of the active power deviation

$$\Delta P_{wt} = 1.5(\Delta v_{fd} i_{wd0} + v_{fd0} \Delta i_{wd} + \Delta v_{fq} i_{wq0} + v_{fq0} \Delta i_{wq}) \tag{4.15}$$

Defining

$$\frac{d\gamma_{\_P}}{dt} = P_{wtref} - P_{wt} \tag{4.16}$$

the linearized small-signal state space form of the active power control is expressed as

$$\dot{\Delta\gamma}_{\_P} = 0\Delta\gamma_{\_P} + \begin{pmatrix} 1 & -1.5 i_{wd0} & -1.5 i_{wq0} & -1.5 v_{fd0} & -1.5 v_{fq0} \end{pmatrix} \Delta B_P \tag{4.17}$$

$$\Delta v_{fdref} = k_{pi} \Delta\gamma_{\_P} + D_p \Delta B_P \tag{4.18}$$

where

$$\Delta B_P = \begin{pmatrix} \Delta P_{wtref} & \Delta v_{fdq} & \Delta i_{wdq} \end{pmatrix}^T \tag{4.19}$$

$$D_p = \begin{pmatrix} k_{pp} & -1.5k_{pp}i_{wd0} & -1.5k_{pp}i_{wq0} & -1.5k_{pp}v_{fd0} & -1.5k_{pp}v_{fq0} \end{pmatrix} . \tag{4.20}$$

E. Reactive power control

The reactive power control as shown in Fig. 4. 2 is expressed as

$$\omega_{ref} = k_q (Q_{wt} - Q_{wtref}) + \omega_{no} \tag{4.21}$$

where the instantaneous reactive power Q_{wt} is described as

$$Q_{wt} = 1.5(-v_{fd}i_{wq} + v_{fq}i_{wd}) . \tag{4.22}$$

Linearizing (4.22) yields the expression of the reactive power deviation

$$\Delta Q_{wt} = 1.5(-\Delta v_{fd}i_{wq0} - v_{fd0}\Delta i_{wq} + \Delta v_{fq}i_{wd0} + v_{fq0}\Delta i_{wd}) . \tag{4.23}$$

The linearized small-signal state space form of the reactive power control is expressed as

$$\Delta\omega_{ref} = \begin{pmatrix} -k_q & -1.5k_q i_{wq0} & 1.5k_q i_{wd0} & 1.5k_q v_{fq0} & -1.5k_q v_{fd0} \end{pmatrix} \Delta B_q \tag{4.24}$$

where

$$\Delta B_q = \begin{pmatrix} \Delta Q_{wtref} & \Delta v_{fdq} & \Delta i_{wdq} \end{pmatrix}^T . \tag{4.25}$$

4.1.2 Small-signal model of WT converters

The WT LSC is modelled as a first-order delay considering pulse width modulation (PWM) and the time constant of the delay is half of the PWM switching period [118]. The output *LC* filter and transformer reactor (as shown in Fig. 2. 2) dynamics can be expressed as

$$
\begin{aligned}
L_w \frac{di_w}{dt} &= -j\omega L_w i_w + v_c - v_f - R_w i_w \\
C_f \frac{dv_f}{dt} &= -j\omega C_f v_f + i_w - i_s \\
L_s \frac{di_s}{dt} &= -j\omega L_s i_s + v_f - \frac{v_{ca}}{T_{wt}}
\end{aligned} \quad . \tag{4.26}
$$

The corresponding small-signal state space form of the *LC* filter and transformer reactance in the *dq* reference is expressed as

$$
\begin{bmatrix} \dot{\Delta i}_{wd} \\ \dot{\Delta i}_{wq} \\ \dot{\Delta v}_{fd} \\ \dot{\Delta v}_{fq} \\ \dot{\Delta i}_{sd} \\ \dot{\Delta i}_{sq} \end{bmatrix} = A_{con} \begin{bmatrix} \Delta i_{wd} \\ \Delta i_{wq} \\ \Delta v_{fd} \\ \Delta v_{fq} \\ \Delta i_{sd} \\ \Delta i_{sq} \end{bmatrix} + B_{con} \begin{bmatrix} \Delta\omega \\ \Delta v_{cd} \\ \Delta v_{cq} \\ \Delta v_{cad} \\ \Delta v_{caq} \end{bmatrix} \tag{4.27}
$$

where

$$
A_{con} = \begin{bmatrix}
-\frac{R_w}{L_w} & \omega_0 & -\frac{1}{L_w} & 0 & 0 & 0 \\
-\omega_0 & -\frac{R_w}{L_w} & 0 & -\frac{1}{L_w} & 0 & 0 \\
\frac{1}{C_f} & 0 & 0 & \omega_0 & -\frac{1}{C_f} & 0 \\
0 & \frac{1}{C_f} & -\omega_0 & 0 & 0 & -\frac{1}{C_f} \\
0 & 0 & \frac{1}{L_w} & 0 & 0 & \omega_0 \\
0 & 0 & 0 & \frac{1}{L_w} & -\omega_0 & 0
\end{bmatrix} \tag{4.28}
$$

$$B_{con}=\begin{bmatrix} i_{wq0} & \frac{1}{L_w} & 0 & 0 & 0 \\ -i_{wd0} & 0 & \frac{1}{L_w} & 0 & 0 \\ v_{fq0} & 0 & 0 & 0 & 0 \\ -v_{fd0} & 0 & 0 & 0 & 0 \\ i_{sq0} & 0 & 0 & -\frac{1}{L_s T_{wt}} & 0 \\ -i_{sd0} & 0 & 0 & 0 & -\frac{1}{L_s T_{wt}} \end{bmatrix}. \tag{4.29}$$

4.1.3 Small-signal model of AC cables

AC cables are represented with *R-L-C* π sections. When the π sections of the AC cables are connected in series, it is equivalent to use Γ sections as two parallel capacitors at a same point can be regarded as one capacitor with twice the original value [119], as shown in Fig. 4. 2. The AC cables in Fig. 4. 2 are represented as

$$\begin{aligned} C_{ca}\frac{dv_{ca}}{dt} &= -j\omega C_{ca}v_{ca}+\frac{i_s}{T_{wt}}-i_{ca} \\ L_{ca}\frac{di_{ca}}{dt} &= -j\omega L_{ca}i_{ca}+v_{ca}-v_{ca2\_1}-R_{ca}i_{ca} \end{aligned}. \tag{4.30}$$

Linearizing at the operating point, the small-signal model of AC cables in the *dq* reference is expressed as

$$\begin{bmatrix} \dot{\Delta v}_{cad} \\ \dot{\Delta v}_{caq} \\ \dot{\Delta i}_{cad} \\ \dot{\Delta i}_{caq} \end{bmatrix} = \begin{bmatrix} 0 & \omega_0 & -\frac{1}{C_{ca}} & 0 \\ -\omega_0 & 0 & 0 & -\frac{1}{C_{ca}} \\ \frac{1}{L_{ca}} & 0 & -\frac{R_{ca}}{L_{ca}} & \omega_0 \\ 0 & \frac{1}{L_{ca}} & -\omega_0 & -\frac{R_{ca}}{L_{ca}} \end{bmatrix} \begin{bmatrix} \Delta v_{cad} \\ \Delta v_{caq} \\ \Delta i_{cad} \\ \Delta i_{caq} \end{bmatrix}$$
$$+ \begin{bmatrix} v_{caq0} & \frac{1}{C_{ca}T_{wt}} & 0 & 0 & 0 \\ -v_{cad0} & 0 & \frac{1}{C_{ca}T_{wt}} & 0 & 0 \\ i_{caq0} & 0 & 0 & -\frac{1}{L_{ca}} & 0 \\ -i_{cad0} & 0 & 0 & 0 & -\frac{1}{L_{ca}} \end{bmatrix} \begin{bmatrix} \Delta\omega \\ \Delta i_{sd} \\ \Delta i_{sq} \\ \Delta v_{ca2\_1d} \\ \Delta v_{ca2\_1q} \end{bmatrix} . \quad (4.31)$$

4.1.4 Complete small-signal model of the offshore wind farms

Due to distributed control of the WT LSC, the small-signal model of each WT converter and control is based on the rotating *dq* reference fixed to its own filter bus voltage. When two WT converters are connected to a common point, the two *dq* frames can have a phase shift as shown in Fig. 4. 3. Therefore, it is necessary to transform the individual rotating reference to a common reference for stability analysis [112].

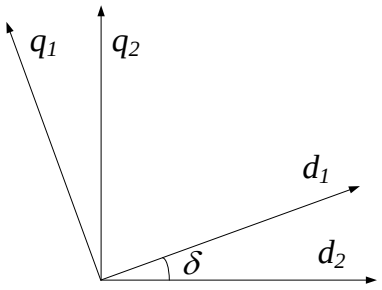

Fig. 4. 3 Reference frames used by two converters.

As shown in Fig. 4. 2, the transformer of WT2 is directly connected to AC cable 1. The current injected into AC cable 2 i_{sum2} is the total current from both WT2

transformer i_{s2}/T_{wt} and AC cable 1 i_{ca}, which should be based on the same rotating reference. Thus, the current of AC cable1 i_{cadq} in d_1q_1 reference frame is transformed to that based on d_2q_2 reference i_{ca1_2dq} , which can be expressed as

$$\begin{aligned} i_{ca1\_2d} &= i_{cad}\cos\delta - i_{caq}\sin\delta \\ i_{ca1\_2q} &= i_{caq}\cos\delta + i_{cad}\sin\delta \end{aligned} . \tag{4.32}$$

Linearizing (4.32) at the operating point, the expression of the current deviation can be obtained

$$\begin{bmatrix} \Delta i_{ca1\_2d} \\ \Delta i_{ca1\_2q} \end{bmatrix} = \begin{bmatrix} \cos\delta_0 & -\sin\delta_0 \\ \sin\delta_0 & \cos\delta_0 \end{bmatrix} \begin{bmatrix} \Delta i_{cad} \\ \Delta i_{caq} \end{bmatrix} + \begin{bmatrix} -i_{cad0}\sin\delta_0 - i_{caq0}\cos\delta_0 \\ -i_{caq0}\sin\delta_0 + i_{cad0}\cos\delta_0 \end{bmatrix} \left[\Delta\delta\right]. \tag{4.33}$$

On the other hand, as shown in (4.31), the input of the AC cable 1 small-signal model is the voltage of the connection point v_{ca2}, which is expressed in the d_2q_2 reference frame. Thus, the voltage needs to be converted to that based on d_1q_1 reference v_{ca2_1dq} using the reversed transformation, expressed as

$$\begin{bmatrix} \Delta v_{ca2\_1d} \\ \Delta v_{ca2\_1q} \end{bmatrix} = \begin{bmatrix} \cos\delta_0 & \sin\delta_0 \\ -\sin\delta_0 & \cos\delta_0 \end{bmatrix} \begin{bmatrix} \Delta v_{ca2d} \\ \Delta v_{ca2q} \end{bmatrix} + \begin{bmatrix} -v_{ca2d0}\sin\delta_0 + v_{ca2q0}\cos\delta_0 \\ -v_{ca2q0}\sin\delta_0 - v_{ca2d0}\cos\delta_0 \end{bmatrix} \left[\Delta\delta\right]. \tag{4.34}$$

4.1.5 Small-signal model of diode rectifier filters

The diode rectifier filters shown in Fig. 4. 1 are represented as

$$
\begin{aligned}
C_1\frac{dv_1}{dt} &= -\frac{(R_2+R_3)v_1}{R_2R_3} + \frac{v_2}{R_2} + \frac{v_4}{R_3} - j\omega_{dr}C_1v_1 - i_1 - i_2 + i_{casumd} - i \\
C_2\frac{dv_2}{dt} &= \frac{v_1}{R_2} - \frac{v_2}{R_2} + i_1 - j\omega_{dr}C_2v_2 \\
C_3\frac{dv_3}{dt} &= i_{1d} - j\omega_{dr}C_3v_3 \\
C_4\frac{dv_4}{dt} &= i_2 + \frac{v_1}{R_3} - \frac{v_4}{R_3} - j\omega_{dr}C_4v_4 \\
L_1\frac{di_1}{dt} &= v_1 - v_2 - v_3 - Ri_1 - j\omega_{dr}L_1i_1 \\
L_2\frac{di_2}{dt} &= v_1 - v_4 - j\omega_{dr}L_2i_2
\end{aligned}
\quad . \qquad (4.35)
$$

Linearizing at the operating point, the small-signal model in the *dq* reference is expressed as

$$
\begin{aligned}
&\left[\dot{\Delta v}_{1d} \quad \dot{\Delta v}_{1q} \quad \dot{\Delta v}_{2d} \quad \dot{\Delta v}_{2q} \quad \dot{\Delta v}_{3d} \quad \dot{\Delta v}_{3q} \quad \dot{\Delta v}_{4d} \quad \dot{\Delta v}_{4q} \quad \dot{\Delta i}_{1d} \quad \dot{\Delta i}_{1q} \quad \dot{\Delta i}_{2d} \quad \dot{\Delta i}_{2q}\right]^T = \\
&A_{drf}\left[\Delta v_{1d} \quad \Delta v_{1q} \quad \Delta v_{2d} \quad \Delta v_{2q} \quad \Delta v_{3d} \quad \Delta v_{3q} \quad \Delta v_{4d} \quad \Delta v_{4q} \quad \Delta i_{1d} \quad \Delta i_{1q} \quad \Delta i_{2d} \quad \Delta i_{2q}\right]^T \\
&+B_{drf}\left[\Delta\omega_{dr} \quad \Delta i_{casumd} \quad \Delta i_{casumq} \quad \Delta i_d \quad \Delta i_q\right]^T
\end{aligned}
\qquad (4.36)
$$

where

$$A_{drf}=\begin{bmatrix}
-\frac{R_2+R_3}{R_2R_3C_1} & \omega_{dr0} & \frac{1}{R_2C_1} & 0 & 0 & 0 & \frac{1}{R_3C_1} & 0 & -\frac{1}{C_1} & 0 & \frac{1}{C_1} & 0 \\
-\omega_{dr0} & -\frac{R_2+R_3}{R_2R_3C_1} & 0 & \frac{1}{R_2C_1} & 0 & 0 & 0 & \frac{1}{R_3C_1} & 0 & -\frac{1}{C_1} & 0 & \frac{1}{C_1} \\
\frac{1}{R_2C_2} & 0 & -\frac{1}{R_2C_2} & \omega_{dr0} & 0 & 0 & 0 & 0 & \frac{1}{C_2} & 0 & 0 & 0 \\
0 & \frac{1}{R_2C_2} & -\omega_{dr0} & -\frac{1}{R_2C_2} & 0 & 0 & 0 & 0 & 0 & \frac{1}{C_2} & 0 & 0 \\
0 & 0 & 0 & 0 & 0 & -\omega_{dr0} & 0 & 0 & \frac{1}{C_3} & 0 & 0 & 0 \\
0 & 0 & 0 & 0 & \omega_{dr0} & 0 & 0 & 0 & 0 & \frac{1}{C_3} & 0 & 0 \\
\frac{1}{R_3C_4} & 0 & 0 & 0 & 0 & 0 & -\frac{1}{R_3C_4} & \omega_{dr0} & 0 & 0 & \frac{1}{C_4} & 0 \\
0 & \frac{1}{R_3C_4} & 0 & 0 & 0 & 0 & \omega_{dr0} & -\frac{1}{R_3C_4} & 0 & 0 & 0 & \frac{1}{C_4} \\
\frac{1}{L_1} & 0 & -\frac{1}{L_1} & 0 & -\frac{1}{L_1} & 0 & 0 & 0 & -\frac{R_1}{L_1} & \omega_{dr0} & 0 & 0 \\
0 & \frac{1}{L_1} & 0 & -\frac{1}{L_1} & 0 & -\frac{1}{L_1} & 0 & 0 & -\omega_{dr0} & -\frac{R_1}{L_1} & 0 & 0 \\
\frac{1}{L_2} & 0 & 0 & 0 & 0 & 0 & -\frac{1}{L_2} & 0 & 0 & 0 & 0 & \omega_{dr0} \\
0 & \frac{1}{L_2} & 0 & 0 & 0 & 0 & 0 & -\frac{1}{L_2} & 0 & 0 & -\omega_{dr0} & 0
\end{bmatrix} \quad (4.37)$$

$$B_{drf}=\begin{bmatrix}
v_{1q0} & -v_{1d0} & v_{2q0} & -v_{2d0} & v_{3q0} & -v_{3d0} & v_{4q0} & -v_{4d0} & i_{1q0} & -i_{1d0} & i_{2q0} & -i_{2d0} \\
\frac{1}{C_1} & 0 & 0 & 0 & 0 & 0 & 0 & 0 & 0 & 0 & 0 & 0 \\
0 & \frac{1}{C_1} & 0 & 0 & 0 & 0 & 0 & 0 & 0 & 0 & 0 & 0 \\
-\frac{1}{C_1} & 0 & 0 & 0 & 0 & 0 & 0 & 0 & 0 & 0 & 0 & 0 \\
0 & -\frac{1}{C_1} & 0 & 0 & 0 & 0 & 0 & 0 & 0 & 0 & 0 & 0
\end{bmatrix}^T \quad .(4.38)$$

4.1.6 Small-signal model of the diode rectifier

The offshore DC voltage v_{dcr} is expressed as [85]

$$v_{dcr}=6\sqrt{3}T_{dr}\frac{\left(v_{pccd}{}^2+v_{pccq}{}^2\right)^{0.5}}{\pi}-\frac{6\omega_{dr}L_{dr}i_{dcr}}{\pi} \quad (4.39)$$

where ω_{dr} is the offshore AC frequency, v_{pccd} and v_{pccq} are the d- and q-axis components of the offshore PCC voltage v_{pcc}. i_{dcr} is the DC current, T_{dr} and L_{dr} are the turn ratio and inductance of the diode rectifier transformer, respectively.

Linearizing (4.39) yields the offshore DC voltage deviation

$$\Delta v_{dcr} = k_i \Delta\omega_{dr} + k_j \Delta v_{pccd} + k_k \Delta v_{pccq} + k_l \Delta i_{dcr} \tag{4.40}$$

where

$$\begin{aligned} k_i &= \frac{\partial v_{dcr}}{\partial \omega_{dr}} = -\frac{6 L_{dr} i_{dcr0}}{\pi} \\ k_j &= \frac{\partial v_{dcr}}{\partial v_{pccd}} = \frac{6\sqrt{3} T_{dr} v_{pccq0}}{\pi \sqrt{\left({v_{pccd0}}^2 + {v_{pccq0}}^2 \right)}} \\ k_k &= \frac{\partial v_{dcr}}{\partial v_{pccq}} = \frac{6\sqrt{3} T_{dr} v_{pccd0}}{\pi \sqrt{\left({v_{pccd0}}^2 + {v_{pccq0}}^2 \right)}} \\ k_l &= \frac{\partial v_{dcr}}{\partial i_{dcr}} = -\frac{6 \omega_{dr0} L}{\pi} \end{aligned} . \tag{4.41}$$

Neglecting power loss in the diode rectifier, its AC active power equals to the DC power:

$$1.5\left(v_{pccd} i_d + v_{pccq} i_q \right) = v_{dcr} i_{dcr} \tag{4.42}$$

where i_d and i_q are the *d*- and *q*-axis components of diode rectifier AC current i_{dr}. Linearizing (4.42) yields the active power deviation

$$1.5\left(v_{pccd0} \Delta i_d + \Delta v_{pccd} i_{d0} + v_{pccq0} \Delta i_q + \Delta v_{pccq} i_{q0} \right) = \Delta v_{dcr} i_{dcr0} + v_{dcr0} \Delta i_{dcr} . \tag{4.43}$$

Substituting the offshore DC voltage deviation Δv_{dcr} from (4.40) into (4.43), the following equation is derived:

$$\begin{aligned} &1.5\left(v_{pccd0} \Delta i_d + v_{pccq0} \Delta i_q \right) = k_i i_{dc0} \Delta\omega_{dr} + \left(k_j i_{dc0} - 1.5 i_{d0} \right) \Delta v_{pccd} \\ &+ \left(k_k i_{dc0} - 1.5 i_{q0} \right) \Delta v_{pccq} + \left(k_l i_{dc0} + v_{dc0} \right) \Delta i_{dc} \end{aligned} . \tag{4.44}$$

The reactive power consumption of the diode rectifier equals to the reactive power injected from the AC:

$$1.5\left(-v_{pccd} i_q + v_{pccq} i_d \right) = v_{dcr} i_{dcr} g\left(\mu \right) \tag{4.45}$$

where

$$g(\mu)=\frac{2\mu-\sin 2\mu}{1-\cos 2\mu}$$
$$\mu=\arccos\left[1-\frac{2\omega_{dr}L_{dr}i_{dcr}}{\sqrt{3\left(v_{pccd}{}^2+v_{pccq}{}^2\right)}T_{dr}}\right]. \tag{4.46}$$

Linearizing (4.45) yields the reactive power deviation

$$\begin{aligned}1.5\left(v_{pccq0}\Delta i_d-v_{pccd0}\Delta i_q\right)&=\Delta v_{dcr}i_{dcr0}g(\mu_0)+v_{dcr0}\Delta i_{dcr}g(\mu_0)\\&+v_{dcr0}i_{dcr0}\Delta g+1.5i_{q0}\Delta v_{pccd}-1.5i_{d0}\Delta v_{pccq}\end{aligned} \tag{4.47}$$

where

$$\begin{aligned}\Delta g&=z_1\Delta\omega_{dr}+z_2\Delta v_{pccd}+z_3\Delta v_{pccq}+z_4\Delta i_{dcr}\\z_1&=b\frac{\partial\mu}{\partial\omega_{dr}}=\frac{2bL_{dr}i_{dcr0}}{\sqrt{3\left(v_{pccd0}{}^2+v_{pccq0}{}^2\right)}T_{dr}\sin\mu_0}\\z_2&=b\frac{\partial\mu}{\partial v_{pccd}}=\frac{-2b\omega_{dr0}L_{dr}i_{dc0}v_{pccq0}}{\sqrt{3}T_{dr}\sin\mu_0\left(v_{pccd0}{}^2+v_{pccq0}{}^2\right)^{1.5}}\\z_3&=b\frac{\partial\mu}{\partial v_{pccq}}=\frac{-2b\omega_{dr0}L_{dr}i_{dc0}v_{pccd0}}{\sqrt{3}T_{dr}\sin\mu_0\left(v_{pccd0}{}^2+v_{pccq0}{}^2\right)^{1.5}}\\z_4&=b\frac{\partial\mu}{\partial i_{dcr}}=\frac{2b\omega_{dr0}L_{dr}}{\sqrt{3\left(v_{pccd0}{}^2+v_{pccq0}{}^2\right)}T_{dr}\sin\mu_0}\\b&=\frac{\partial g}{\partial\mu}=\left[2-\frac{2\left(2\mu_0-\sin 2\mu_0\right)\sin 2\mu_0}{\left(1-\cos 2\mu_0\right)^2}\right]\end{aligned}. \tag{4.48}$$

Substituting (4.40) into (4.47) and combining with (4.44), the *d*- and *q*-axis components of diode rectifier AC current deviation are expressed as

$$\begin{cases}\Delta i_d=k_a\Delta\omega_{dr}+k_b\Delta v_{pccd}+k_c\Delta v_{pccq}+k_d\Delta i_{dcr}\\\Delta i_q=k_e\Delta\omega_{dr}+k_f\Delta v_{pccd}+k_g\Delta v_{pccq}+k_h\Delta i_{dcr}\end{cases} \tag{4.49}$$

where

$$\begin{cases} k_a = m\left(k_i i_{dcr0} v_{pccd0} + k_i i_{dcr0} g(\mu_0) v_{pccq0} + z_1 v_{dcr0} i_{dc0} v_{pccq0}\right) \\ k_b = m\left(k_j i_{dcr0} v_{pccd0} - 1.5 i_{d0} v_{pccd0} + k_j i_{dcr0} g(\mu_0) v_{pccq0} + z_2 v_{dcr0} i_{dcr0} v_{pccq0} + 1.5 i_{q0} v_{pccq0}\right) \\ k_c = m\left(k_k i_{dcr0} v_{pccd0} - 1.5 i_{q0} v_{pccd0} + k_k i_{dcr0} g(\mu_0) v_{pccq0} + z_3 v_{dcr0} i_{dcr0} v_{pccq0} - 1.5 i_{d0} v_{pccq0}\right) \\ k_d = m\left(k_l i_{dcr0} v_{pccd0} + v_{dcr0} v_{pccd0} + k_l i_{dcr0} g(\mu_0) v_{pccq0} + z_4 v_{dcr0} i_{dcr0} v_{pccq0} + v_{dcr0} g(\mu_0) v_{pccq0}\right) \\ k_e = m\left(k_i i_{dcr0} v_{pccq0} - k_i i_{dcr0} g(\mu_0) v_{pccd0} - z_1 v_{dcr0} i_{dcr0} v_{pccd0}\right) \\ k_f = m\left(k_i i_{dcr0} v_{pccq0} - 1.5 i_{d0} v_{pccq0} - k_l i_{dcr0} g(\mu_0) v_{pccd0} - z_2 v_{dcr0} i_{dcr0} v_{pccd0} - 1.5 i_{q0} v_{pccd0}\right) \\ k_g = m\left(k_k i_{dcr0} v_{pccq0} - 1.5 i_{q0} v_{pccq0} - k_k i_{dcr0} g(\mu_0) v_{pccd0} - z_3 v_{dcr0} i_{dcr0} v_{pccd0} + 1.5 i_{d0} v_{pccd0}\right) \\ k_h = m\left(k_l i_{dcr0} v_{pccq0} + v_{dcr0} v_{pccq0} - k_l i_{dcr0} g(\mu_0) v_{pccd0} - z_4 v_{dcr0} i_{dcr0} v_{pccd0} - v_{dcr0} g(\mu_0) v_{pccd0}\right) \\ m = \left(1.5 {v_{pccd0}}^2 + 1.5 {v_{pccq0}}^2\right)^{-1} \end{cases} . \quad (4.50)$$

From (4.40) and (4.49), the small-signal model of diode rectifier HVDC station is expressed as

$$\begin{bmatrix} \Delta i_d \\ \Delta i_q \\ \Delta v_{dcr} \end{bmatrix} = \begin{bmatrix} k_a & k_b & k_c & k_d \\ k_e & k_f & k_g & k_h \\ k_i & k_j & k_k & k_l \end{bmatrix} \begin{bmatrix} \Delta \omega_{dr} \\ \Delta v_{pccd} \\ \Delta v_{pccq} \\ \Delta i_{dcr} \end{bmatrix} . \quad (4.51)$$

4.1.7 Small-signal model of HVDC cables

The dynamics of HVDC cables in Fig. 4. 1 are expressed as

$$\begin{aligned} L_{eq} \frac{di_{dcr}}{dt} + 2R_{dc} i_{dcr} + v_{dcc} &= v_{dcr} \\ C_{dc} \frac{dv_{dcc}}{dt} &= i_{dcr} - i_{dci} \\ 2L_{dc} \frac{di_{dci}}{dt} + 2R_{dc} i_{dci} + v_{dci0} &= v_{dcc} \end{aligned} \quad (4.52)$$

where

$$L_{eq} = 2L_{dc} + 4L_{dr} . \quad (4.53)$$

Linearizing at the operating point, the small-signal model of the HVDC cable is expressed as

$$\begin{bmatrix} \dot{\Delta i}_{dcr} \\ \dot{\Delta i}_{dci} \\ \dot{\Delta v}_{dcc} \end{bmatrix} = \begin{bmatrix} -2\dfrac{R_{dc}}{L_{eq}} & 0 & -\dfrac{1}{L_{eq}} \\ 0 & -\dfrac{R_{dc}}{L_{dc}} & \dfrac{1}{2L_{dc}} \\ \dfrac{1}{C_{dc}} & -\dfrac{1}{C_{dc}} & 0 \end{bmatrix} \begin{bmatrix} \Delta i_{dcr} \\ \Delta i_{dci} \\ \Delta v_{dcc} \end{bmatrix} + \begin{bmatrix} \dfrac{1}{L_{eq}} \\ 0 \\ 0 \end{bmatrix} \Delta v_{dcr} . \tag{4.54}$$

Fig. 4. 4 shows the complete small-signal model of WT LSCs connected with DR-HVDC.

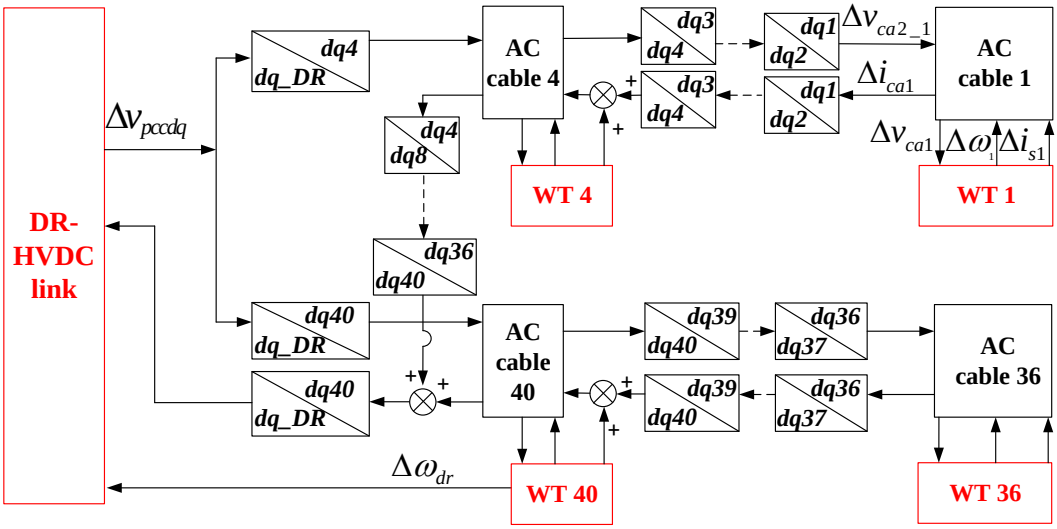

Fig. 4. 4 Complete small-signal model of WT converters with DR-HVDC.

4.2 Validation of the small-signal model

The small-signal model of 40 aggregated WTs connected with DR-HVDC systems (including the control strategies), as shown in Fig. 4. 4, is established in MATLAB. The system parameters and control parameters for the small-signal model are listed in Table 4. 1. In order to validate the small-signal model, the time domain performances of the small-signal model in MATLAB are compared with the time domain simulation results of the nonlinear PSCAD/EMTDC model. In steady state, the generated powers of the 4 WTs in the first string are 25, 18, 15 and 24 MW, respectively, while each of the remaining 36 WT converters operates at full power of 25 MW.

Table 4. 1 Parameters of the tested DR-HVDC systems for small-signal analysis

Components	**Parameters**	**Values**
WT converters	Converter rating	25 MW
	Converter reactance	0.1 pu
	Filter capacitor	0.1 pu
	Transformer ratio	0.69 kV/66 kV
	Leakage inductance	0.08 pu
AC cable	R_{ac}; L_{ac}; C_{ac}	0.6 Ω; 2 mH; 2×0.672 μF
DR filter	C_1; C_2	6.72 μF; 116.98 μF
	C_3; C_4	1300 μF; 116.98 μF
	L_1; L_2	7.8 mH; 0.78 mH
	R_1; R_2; R_3	1.70 Ω; 14.97 Ω; 4.76 Ω
12-pulse DR	Transformer ratio	66 kV/261.8 kV /261.8 kV
	Leakage inductance	0.18 pu
	Power; DC voltage	1000 MW; ±320 kV
DC cable	R_{dc}; L_{dc}; C_{dc}	1.25 Ω; 0.3 H; 26 μH
Control parameters	k_{ip}; k_{ii}; k_{vp}; k_{vi}	0.0057 Ω; 0.909Ω./s; 4.175 Ω^{-1}; 278.34$\Omega^{-1}s^{-1}$
	k_{lp}; k_{li}; k_{pp}; k_{pi}	448.2 rad/(sv); 7052 rad/(s^2v); 0.5 kV/MW; 1 kV/(sMW)
	k_f; k_q	0.1 (skV)/rad; 1 rad/(sMVAr)

Fig. 4. 5 compares the responses between the nonlinear PSCAD model and the linearized small-signal MATLAB model. In the simulation, the active power order of WT1 (as shown in Fig. 4. 1) decreases from its original operating point of 25 MW by -0.25 MW at 0.1 s and WT2 reactive power order increases from its original operating point of 0 by 0.05 MVAr at 0.2 s. As can be seen, the performances of the small-signal model are in good agreements with the results of the PSCAD/EMTDC simulation, indicating that the developed model accurately reproduces the system behaviours.

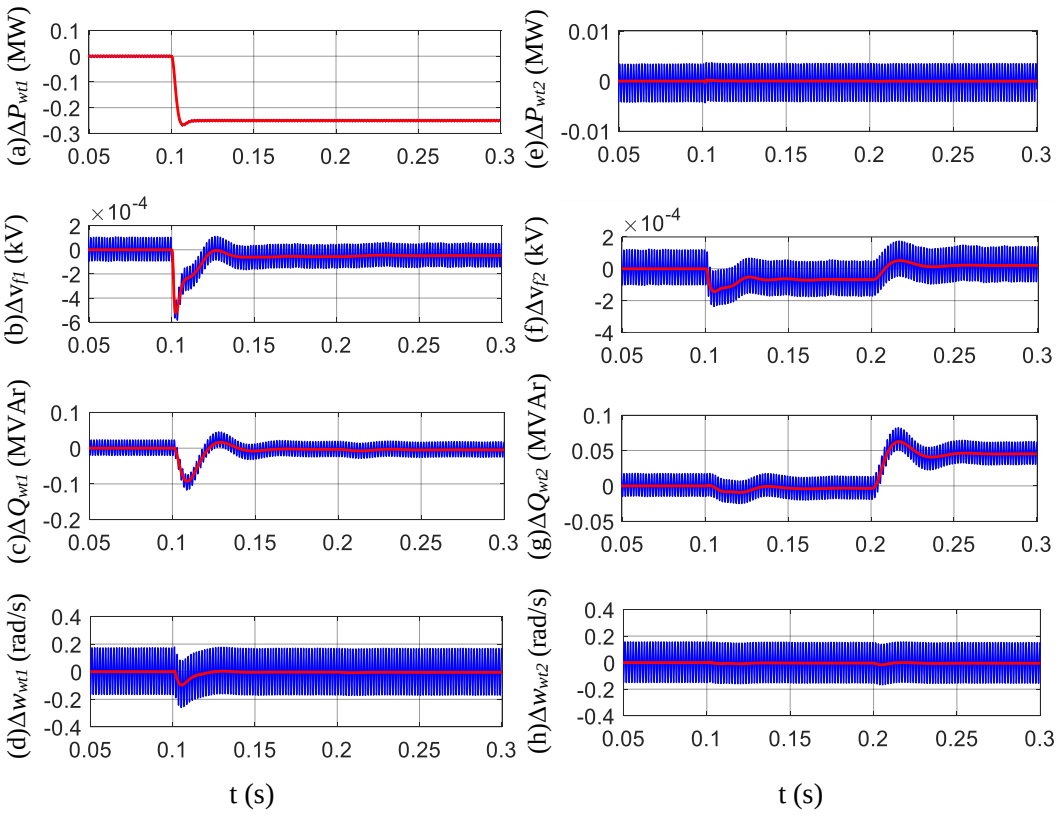

Fig. 4. 5 Comparison between small-signal model (red) and PSCAD model (blue) during active power and reactive power change: (a) WT1 active power change; (b) WT1 AC voltage change; (c) WT1 reactive power change; (d) WT1 frequency change; (e) WT2 active power change; (f)WT2 AC voltage change; (g) WT2 reactive power change; (h) WT2 frequency change.

4.3 Wind farm level analysis of *P* and *Q* interactions with *V* and *f*

In AC grids with high *X*/*R* ratio (inductive), *P*-*f* and *Q*-*V* controls are commonly used to share active and reactive power among converters [112-114]. When wind power is transmitted through a DR-HVDC link, *P*-*V* and *Q*-*f* controls have shown adequate system performance, as described in chapter 3. However, more detailed theoretical analysis is required on the rationales behind such a control design and how does the design affect the system response. Based on the developed small-signal model, this section conducts the wind farm level analysis, where the offshore wind farms are simplified as a lumped WT converter (as shown in Fig. 4. 6), to reveal the interactions between different control variables.

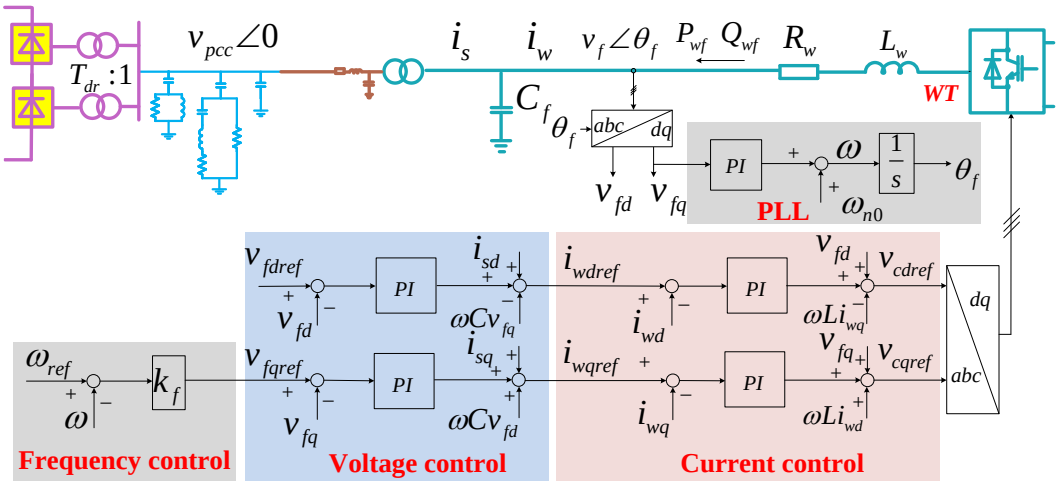

Fig. 4. 6 Frequency, voltage and current control of a lumped WT converter.

To study the interactions of wind farms' active and reactive power with the AC voltage and frequency, relevant transfer functions are derived from the developed linearized small-signal model of the DR-HVDC systems. Fig. 4. 7 (a)-(d) show the respective Bode plots of wind farm active power P_{wf} and reactive power Q_{wf} with reference to variations of AC voltage reference v_{fdref} and frequency reference ω_{ref} variation for three different power levels (P=1 pu, 0.5 pu and 0.1 pu).

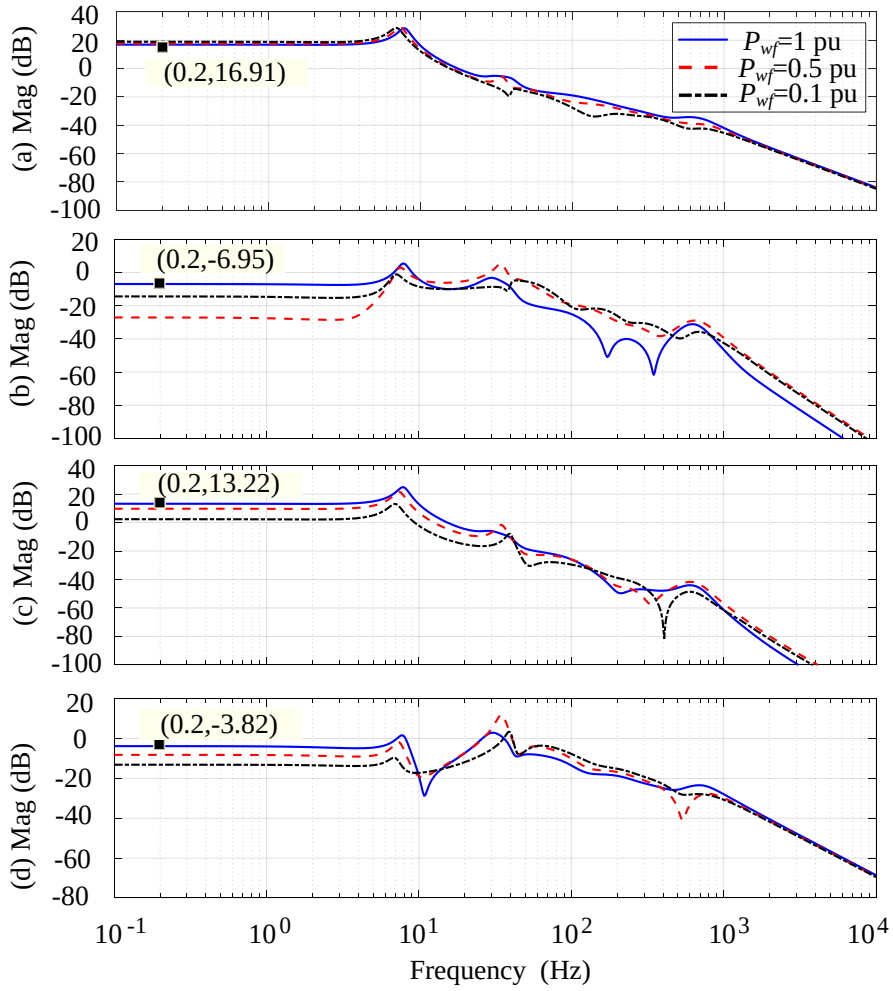

Fig. 4. 7 Bode responses from v_{fdref} and ω_{ref} to P_{wf} and Q_{wf}: (a) Gain from v_{fdref} to P_{wf}; (b) Gain from ω_{ref} to P_{wf}; (c) Gain from v_{fdref} to Q_{wf}; (d) Gain from ω_{ref} to Q_{wf}.

The accuracy of Fig. 4. 7 is validated by the comparison between the low-frequency Bode responses and the DC gains obtained from the time domain model, presented in Table 4. 2. For the system operating at P=1 pu, the gain from ω_{ref} to P_{wf} around DC in the Bode plot is -6.95 dB ($10^{-6.95/20}$ = 0.45), as shown in Fig. 4. 7 (b). In the time domain model, when the offshore network frequency increases by 0.001 pu (from 50 Hz to 50.05 Hz), the transmitted active power increases by 0.00045 pu (from 1000 MW to 1000.45 MW). Therefore, from the time domain results, it can be derived that the DC gain from ω_{ref} to P_{wf} is also around 0.45. As can be seen, the DC gain from the time domain model is in a good agreement with the Bode response in Fig. 4. 7 (b). Same

conclusions can be derived by comparing Fig. 4. 7 (a), (c), and (d) with the DC gains from the time domain model, as listed in Table 4. 2.

Table 4. 2 Comparison between the Bode responses and time domain responses

	DC gains	DC gains from Bode responses	DC gains from time domain model*
P=1 pu	M (v_{dref} *to* P_{wf})	16.91dB ($10^{16.91/20}$=7.00)	0.00680 / 0.001 = 6.80
	M (v_{dref} *to* Q_{wf})	13.22 dB ($10^{13.22/20}$=4.58)	0.00453 / 0.001 = 4.53
	M (ω_{ref} *to* P_{wf})	-6.95 dB (0.45)	0.00045 / 0.001 = 0.45
	M (ω_{ref} *to* Q_{wf})	-3.82 dB (0.64)	0.00063 / 0.001 = 0.63
P=0.5 pu	M (v_{dref} *to* P_{wf})	17.65 dB (7.63)	0.00790 / 0.001 = 7.90
	M (v_{dref} *to* Q_{wf})	9.72 dB (3.06)	0.00311 / 0.001 = 3.11
	M (ω_{ref} *to* P_{wf})	-27.1 dB (0.05)	0.00006 / 0.001 = 0.06
	M (ω_{ref} *to* Q_{wf})	-8.20 dB (0.39)	0.00038 / 0.001 = 0.38
P=0.1 pu	M (v_{dref} *to* P_{wf})	18.96 dB (8.87)	0.00927 / 0.001 = 9.27
	M (v_{dref} *to* Q_{wf})	2.364 dB (1.31)	0.00125 / 0.001 = 1.25
	M (ω_{ref} *to* P_{wf})	-14.43 dB (0.19)	0.00019 / 0.001 = 0.19
	M (ω_{ref} *to* Q_{wf})	-13.13 dB (0.22)	0.00022 / 0.001 = 0.22

*Note: Base value P_{wf}=1000 MW, Q_{wf}=1000 MVar, V_{dref}=56 kV, ω_{ref}=100π rad/s.

From the Bode responses at low-frequency range shown in Fig. 4. 7 (a) and (b), it can be seen that the gains from wind farm output voltage reference v_{fdref} to wind farm active power P_{wf} (16.91 dB when P=1 pu, 17.65 dB when P=0.5 pu, 18.96 dB when P=0.1 pu) are much larger than the gains from frequency reference ω_{ref} to active power P_{wf} (-6.95 dB when P=1 pu, -27.1 dB when P=0.5 pu, -14.43 dB when P=0.1 pu). This indicates that, at wind farm level, the active power is predominantly determined by the AC voltage magnitude while AC frequency variation is weakly linked to wind farm active power when DR-HVDC system is used.

Similarly, Fig. 4. 7 (c) and (d) show that, at low frequency range, the gains from wind farm AC reference voltage v_{fdref} to reactive power Q_{wf} (13.22 dB when P=1 pu, 9.72 dB when P=0.5 pu, 2.364 dB when P=0.1 pu) are much greater than the gains from frequency reference ω_{ref} to reactive power Q_{wf} (-3.82 dB when P=1 pu, -8.2 dB when P=0.5 pu, -13.13 dB when P=0.1 pu). This indicates that the wind farm reactive power is also predominantly regulated by the AC voltage while wind farm AC frequency variation has small impact on the wind farm reactive power output.

From the above analysis and discussion, it can be concluded that AC voltage magnitude has a significant effect on both active and reactive power in DR-HVDC connected wind farms.

As the gains from wind farm AC voltage to active power are greater than those from AC voltage to reactive power across the wide power variation range, as shown in Fig. 4. 7 (a) and (b), wind farm AC voltage is selected as the control variable to regulate the wind farm active power as illustrated in chapter 3 and again illustrated in Fig. 4. 8 (a), where a PI controller is used to eliminate the steady state error.

For controlling / sharing the reactive power of the wind farms, the relationship between reactive power and frequency as demonstrated in Fig. 4. 7 (d) is utilised, and reactive power / frequency droop control shown in Fig. 4. 8 (b) is designed. Such droop control ensures steady state reactive power to be shared among WT converters due to the same steady state frequency across the whole offshore network.

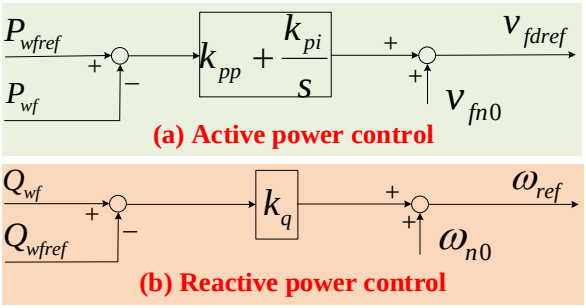

Fig. 4. 8 Wind farm *P*-*V* and *Q*-*f* control.

4.4 WT level analysis of the DR-HVDC connected wind farm systems

The wind farm level analysis shows DR-HVDC active power is predominantly determined by the AC voltage magnitude which leads to the previously used *P-V* and *Q-f* control. However, when such a control scheme is applied for each WT converter, how it affects the transmitted active and reactive power from each WT to the offshore wind farm AC network has not been properly addressed. This section presents the WT level analysis based on the time-domain simulation results in PSCAD/EMTDC when one of the 40 WTs (WT5 in string 2 as shown in Fig. 4. 1) changes its active power, to explore the potential problems in the existing design.

During 0.02 s to 0.03 s, WT5 in string 2 ramps down its active power from 1 pu to 0.2 pu. Due to the action of the *P-V* controller, WT5 AC voltage v_{fd5} decreases from 1.04 pu to 0.99 pu, as shown in Fig. 4. 9 (b). The reduction of v_{fd5} increases the inductive reactive power absorption of WT5 Q_{wt5} (shown as negative) shown in Fig. 4. 9 (c) from -0.03 pu to -0.31 pu at 0.03s. Due to the action of the *Q-f* droop controller, WT5 frequency f_{wt5} decreases from 0.998 pu to 0.978 pu during 0.02 s - 0.03 s while the PCC frequency f_{pcc} and WT1 frequency f_{wt1} remain largely unchanged during this period, as shown in Fig. 4. 9 (d). Consequently, the phase difference between WT5 output voltage vector and PCC voltage vector ($\theta_{5\text{-}pcc}$) decreases from 0.096 rad. (5.44^o) to 0.07 rad. (4.01^o) at 0.03 s, as shown in Fig. 4. 9 (e).

After 0.03 s, the phase difference $\theta_{5\text{-}pcc}$ continues to decrease from 0.07 rad. (4.01^o) and eventually settles at 0.03 rad. (1.72^o), as shown in Fig. 4. 9 (e). This leads to further reduction of active power from WT5 (P_{wt5} becomes slightly less than 0.2 pu) and consequently, the active power controller now starts to increase the AC voltage v_{fd5} from 0.99 pu to 1.03 pu as can be seen in Fig. 4. 9 (b). This results in the recovery of inductive reactive power absorption Q_{wt5} from -0.31 pu to -0.032 pu while the transmitted active power of WT5 P_{wt5} maintains at 0.2 pu.

As seen from the WT level analysis in Fig. 4. 9 (a) and (e), the change of WT transmitted active power is mainly dependent on the variation of phase difference as

in a conventional power network, although the wind farm level analysis shows the transmitted active power of DR depends on the variation of wind farm PCC AC voltage magnitude. Overall, active power change of WTs is achieved through the interaction upon the AC voltage, reactive power, frequency and phase angle.

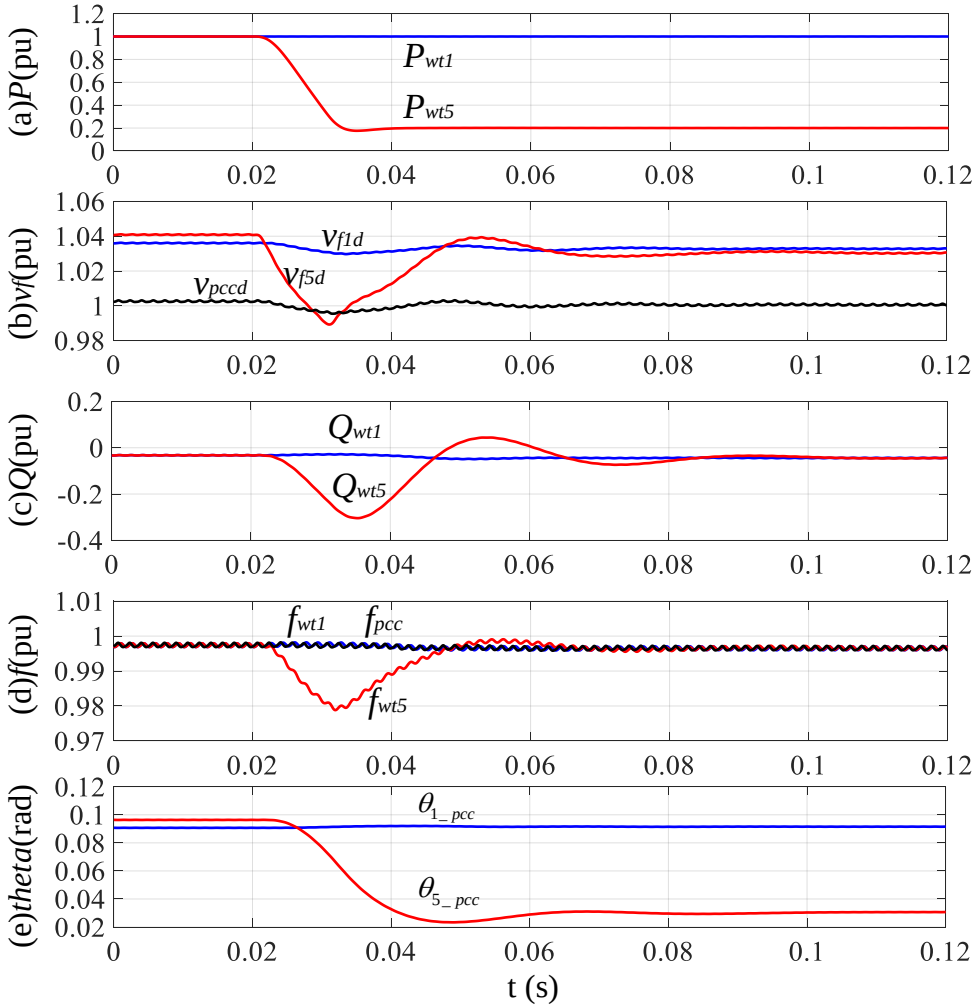

Fig. 4. 9 Performances of system when WT5 active power order changes: (a) WT1 and WT5 active power; (b) WT1, WT5 and PCC d-axis AC voltage; (c) WT1 and WT5 reactive power; (d) WT1, WT5 and PCC frequency; (e) phase difference between WT1 and PCC ($\theta_{1\text{-}pcc}$); WT5 and PCC ($\theta_{5\text{-}pcc}$).

As *P-f* and *Q-V* controls are commonly used for converters when the transmission impedance is mainly inductive in AC grids, Fig. 4. 10 compares the performances of DR-HVDC connected WTs, using the *P-f* and *Q-V* droop control and the proposed *P-*

V and *Q-f* droop control. As seen, when the active power order of WT5 in string 2 decreases from 1 pu to 0.2 pu during 0.2 - 0.21 s, the *P-f* and *Q-V* droop control results in severe oscillation and long settling times, caused by the strong coupling between active power and AC voltage as described in the wind farm level analysis.

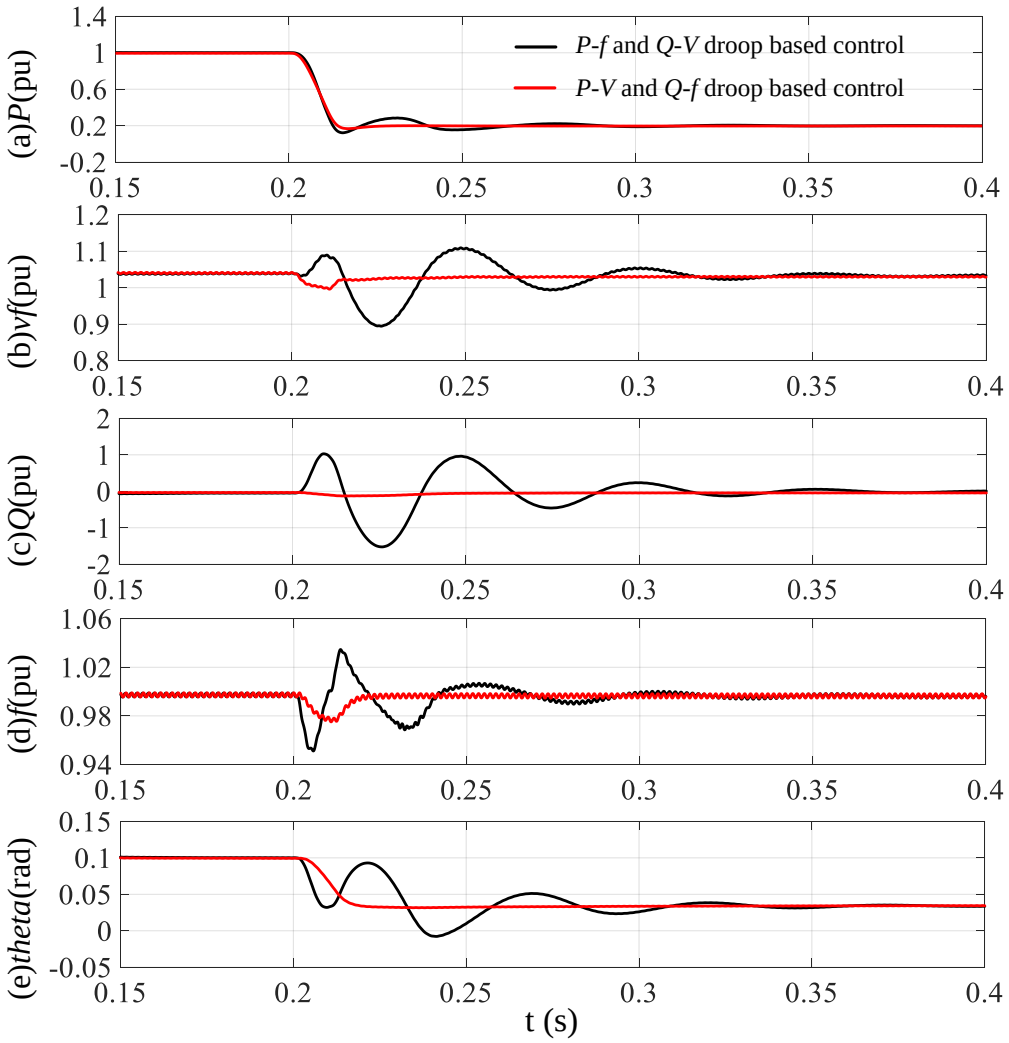

Fig. 4. 10 Performance of system when WT5 active power order changes with *P-V/Q-f* based control and *P-f /Q-V* based control: (a) WT5 active power; (b) WT5 AC voltage; (c) WT5 reactive power; (d) WT5 frequency; (e) phase difference between WT5 and PCC ($\theta_{5\text{-}PCC}$).

4.5 Proposed angle compensation control strategy of WT converters

4.5.1 Coupling between WT active power and reactive power

As can be seen in Fig. 4. 9, due to the use of *P*-*V* and *Q*-*f* control and system interaction, the WT active and reactive power are strongly coupled. During the decrease of WT active power, its reactive power also decreases initially to regulate the WT output phase angle.

In addition to the time domain responses, the coupling between WT active power and reactive power is also analysed in the frequency domain. Fig. 4. 11 shows the Bode response from WT5 active power reference to reactive power. The peak gain of -2.5 dB occurs at around 28 Hz, which is in accordance with the reactive power oscillation frequency during active power change as demonstrated in Fig. 4. 9.

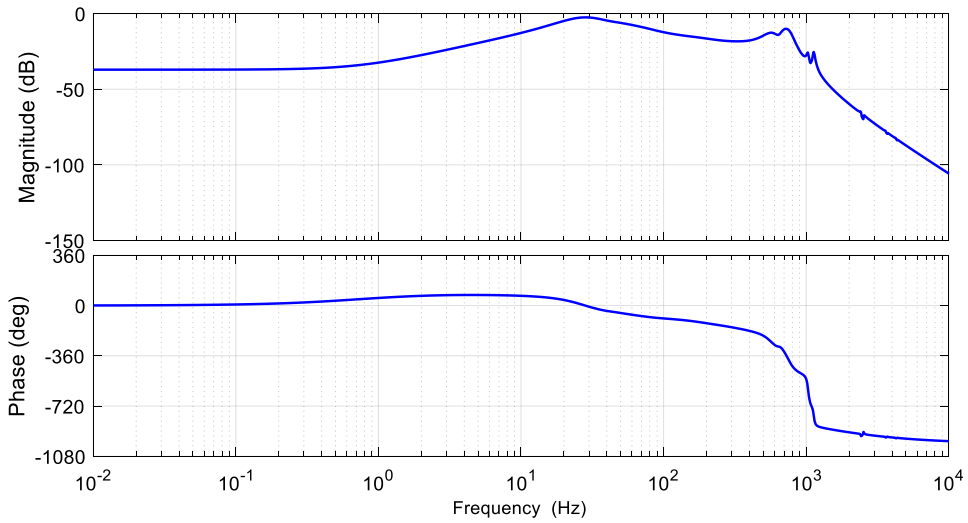

Fig. 4. 11 Bode response from active power reference to reactive power.

4.5.2 Angle compensation control

To reduce the coupling between WT active power and reactive power, an angle compensation control is proposed after the analysis of coupling mechanism.

Considering an individual WT, its steady-state WT active power P_{wtc} and reactive power Q_{wtc} transmitted to the offshore PCC shown in Fig. 4. 12 is expressed as

$$P_{wtc} = \frac{V_{pcc} V_c \sin\theta_c}{X} \tag{4.55}$$

$$Q_{wtc} = \frac{\left(V_c - V_{pcc}\cos\theta_c\right)V_c}{X} \tag{4.56}$$

where θ_c is the phase difference between the offshore PCC voltage and WT converter output voltage and X is equivalent inductance between these two voltages (as the resistance and capacitance are much less than the sum of WT inductance and transformer leakage inductance, and thus are neglected).

During the power change of one single WT, the variation of offshore PCC voltage V_{pcc} is much less than that of converter output voltage V_c (as shown in Fig. 4. 9), and thus, V_{pcc} can be considered to be constant. Accordingly, linearizing (4.55) yields the expression of WT active power variation

$$\triangle P_{wtc} = \frac{V_{pcc0} V_{c0}\cos\theta_{co}}{X}\Delta\theta_c + \frac{V_{pcc0}\sin\theta_{c0}}{X}\Delta V_c \tag{4.57}$$

As $\frac{V_{pcco}V_{co}cos\theta_{co}}{X} \gg \frac{V_{pcco}sin\theta_{co}}{X}$ for a typical small phase shift θ_{co}, phase angle variation at each WT terminal has a much higher impact on WT active power change than the variation of WT AC voltage magnitude.

On the other hand, WT AC voltage output variation has a higher impact on WT reactive power change due to the inductive impedance, described as

$$\Delta Q_{wtc} = \frac{V_{pcc0}\sin\theta_{c0} V_{c0}}{X}\Delta\theta_c + \frac{2V_{c0} - V_{pcc0}\cos\theta_{c0}}{X}\Delta V_c \tag{4.58}$$

However, due to the use of *P-V* and *Q-f* control, active and reactive power of each WT are strongly coupled, as already been demonstrated in Fig. 4. 9 and Fig. 4. 11.

If WT phase angle can be regulated faster during the active power variation, WT terminal AC voltage fluctuation can be effectively reduced, as depicted by (4.57). As a result, WT reactive power dynamics during the transient can be improved, as seen in

(4.58). Based on this observation, an additional angle compensation control as shown in Fig. 4. 12 is proposed to reduce the coupling between WT active and reactive power. The angle compensation control takes the WT active power as the input and regulates the *q*-axis component of the converter output voltage reference v_{cq} through a gain k_{pq} (to directly affect the phase angle) as

$$v_{cqcom} = k_{pq} P_{wt} \tag{4.59}$$

When the WT generated active power increases, the WT output phase angle will quickly increase with the proposed angle compensation control, leading to reduced WT AC voltage and reactive power fluctuation. Similarly, when the WT generated active power decreases, the WT output phase angle will quickly decrease to reduce the variation of WT AC voltage and reactive power. The coupling between WT active and reactive power is thus reduced.

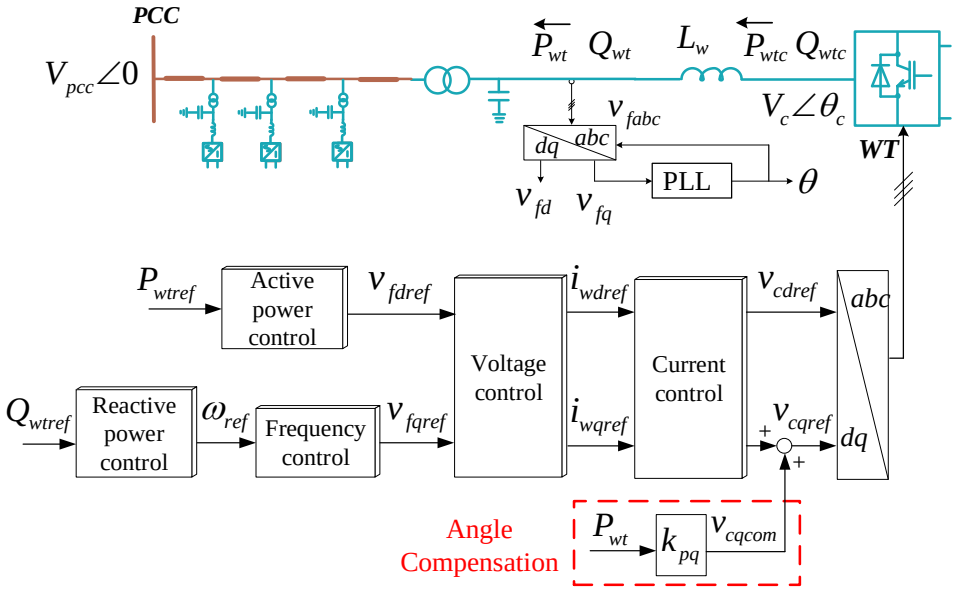

Fig. 4. 12 Proposed WT angle compensation control scheme.

4.5.3 Simulation results of the angle compensation control

Fig. 4. 13 shows the Bode responses from active power reference to reactive power with different gains of the angle compensation control (k_{pq}). As can be seen, the peak gain is effectively decreased from -2.5 dB without angle compensation (i.e. k_{pq}=0) to

-15.5 dB for the proposed control with k_{pq}=0.0015 kV/MW. In low frequency range (f < 5 Hz), the proposed angle compensation control exhibits the same responses as those of conventional control, indicating that the steady state active and reactive power are not affected by the additional angle compenstion loop.

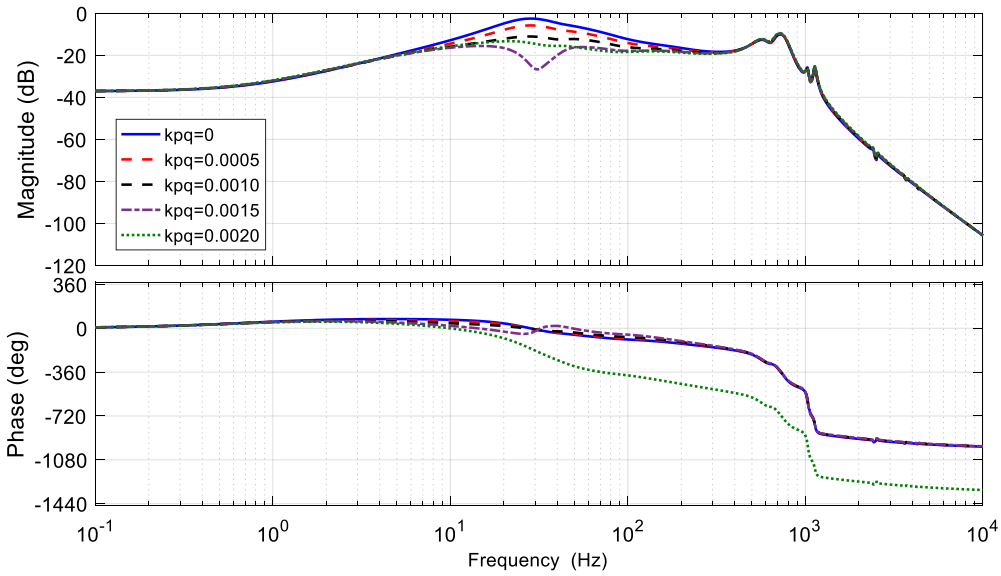

Fig. 4. 13 Bode responses from active power reference to reactive power.

WT responses with and without the proposed angle compensation control are compared in PSCAD/EMTDC simulation, as shown in Fig. 4. 14. In steady state (before 0.2 s), both control methods operate satisfactorily at the same operation point. From 0.2 s to 0.21 s, the active power order of WT5 in string 2 (shown in Fig. 4. 1) decreases from 1 pu to 0.2 pu. As shown in Fig. 4. 14 (d) and (e), the frequency and phase angle decrease faster during active power transient with the proposed control when compared to the conventional design without angle compensation. This leads to lower WT AC voltage variation and significant reduction of reactive power oscillation during the active power change as shown in Fig. 4. 14 (b) and (c).

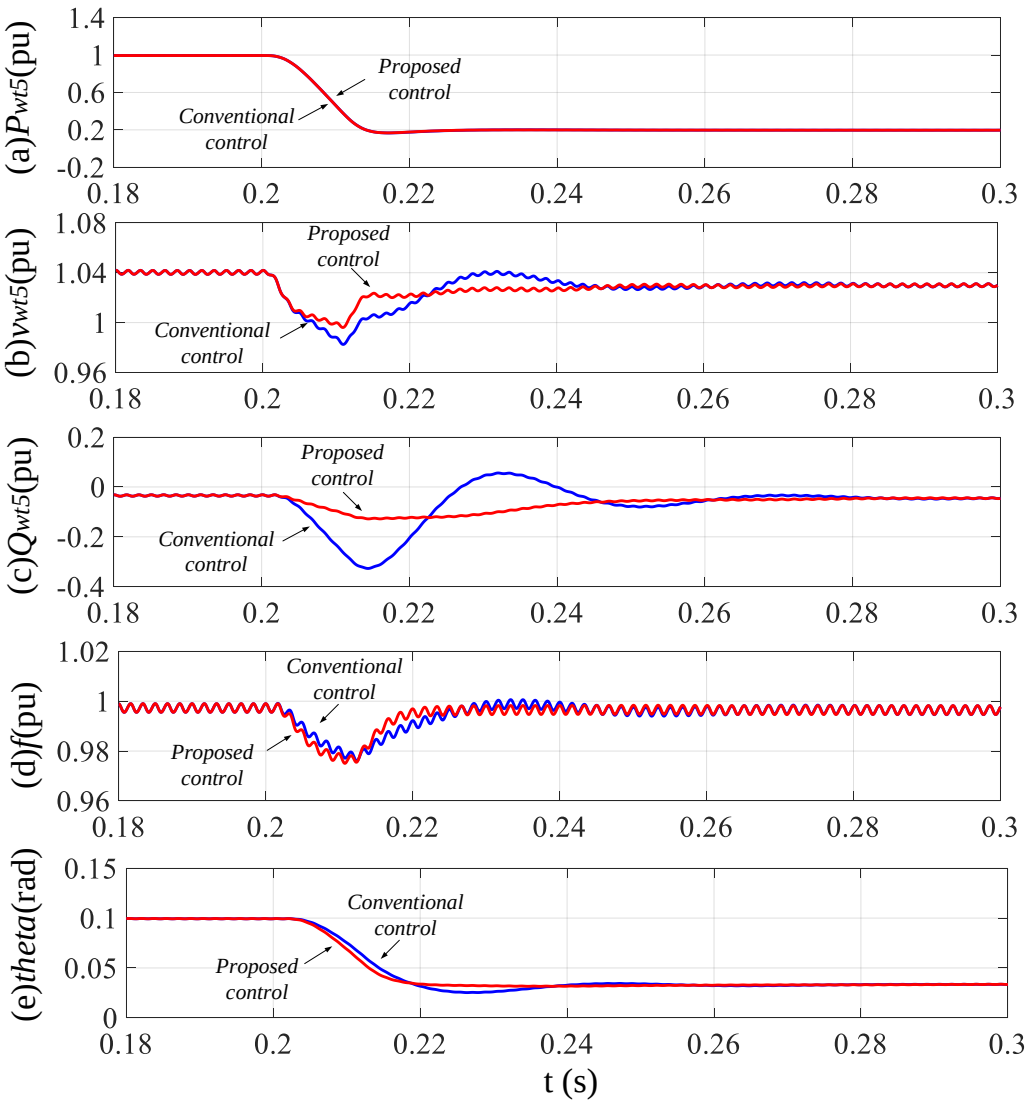

Fig. 4. 14 Performance of system when WT5 active power order changes: (a) WT5 active power; (b) WT5 AC voltage; (c) WT5 reactive power; (d) WT5 frequency; (e) phase difference between WT5 and PCC ($\theta_{5\text{-PCC}}$).

4.6 Stability analysis of the proposed control strategy

To derive the stable range of the angle compensation control parameter, active power control parameter and reactive power control parameter, the stability analysis is carried out based on the frequency domain model in this section. Time domain results from PSCAD non-linear model is used to validate the stable range of the control parameters.

4.6.1 Stability analysis of angle compensation control

Fig. 4. 15 shows the movements of the most affected poles when angle compensation control parameter k_{pq} increases from 0 to 0.06 kV/MW by a step of 0.01 kV/MW. When k_{pq} increases to 0.06 kV/MW, these poles appear on the right-half plane, potentially leading to system instability. Therefore, k_{pq} needs to be less than 0.06 kV/MW to ensure system stability.

Fig. 4. 16 shows the PSCAD simulation results of WT1 with the variation of k_{pq}. The system is unstable when k_{pq} is set at 0.06 kV/MW before 0.45 s but becomes stable after reducing k_{pq} from 0.06 kV/MW to 0.05 kV/MW at 0.45 s. This is in a good agreement with the root locus analysis as presented in Fig. 4. 15.

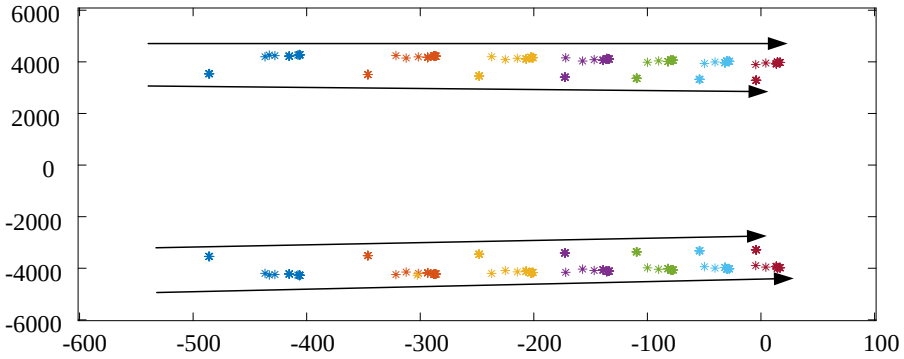

Fig. 4. 15 Root locus when k_{pq} increases from 0 to 0.06 by a step of 0.01.

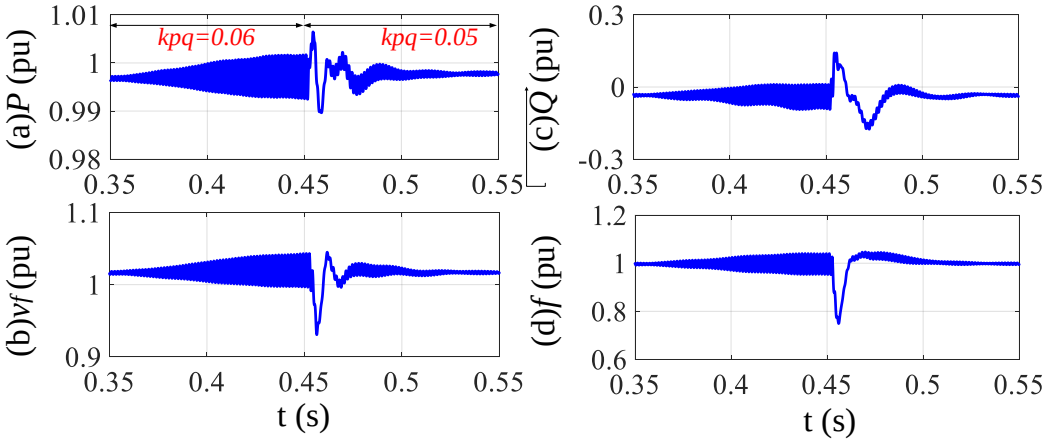

Fig. 4. 16 PSCAD WT1 results when k_{pq} steps from 0.06 to 0.05 at 0.45 s: (a) WT active power; (b) WT AC voltage; (c) WT reactive power; (d) WT frequency.

4.6.2 Stability analysis of active power control

With the integral gain of the WT active power control k_{pi} at 1 kV/(sMW), Fig. 4. 17 shows the movements of the most affected poles when the active power controller proportional gain k_{pp} decreases from 0.51 kV/MW to 0.01 kV/MW by the step of -0.05 kV/MW. When k_{pp} decreases to 0.01 (skV)/rad, some poles appear on the right-half plane, leading to potential system instability.

Fig. 4. 18 shows the PSCAD simulation results of WTs with the variation of k_{pp}. The system is unstable when k_{pp} is set at 0.01 kV/MW before 0.45 s but becomes stable after k_{pp} stepping to 0.11 kV/MW at 0.45 s, which is in a good agreement with root locus analysis in Fig. 4. 17.

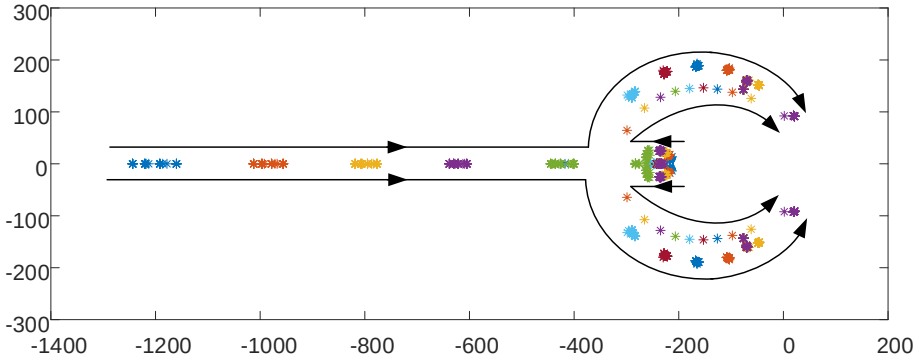

Fig. 4. 17 Root locus when k_{pp} decreases from 0.51 to 0.01 by step of -0.05.

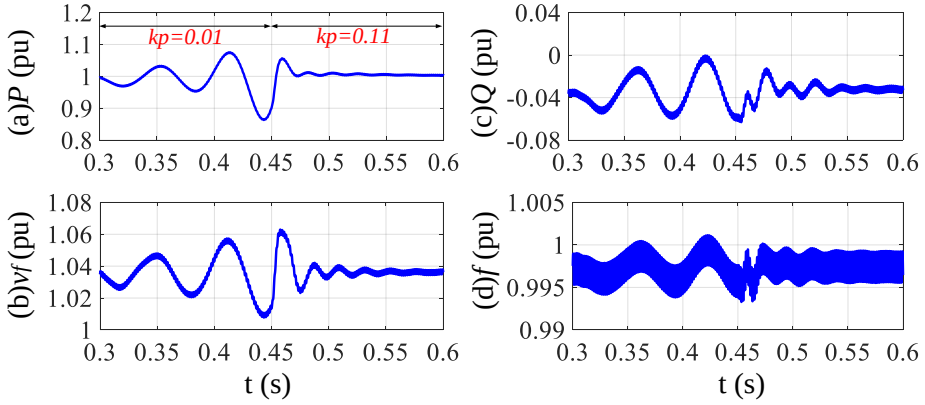

Fig. 4. 18 PSCAD results for WT1 when k_{pp} steps from 0.01 to 0.11 at 0.45 s: (a) WT active power; (b) WT AC voltage; (c) WT reactive power; (d) WT frequency.

4.6.3 Stability analysis of reactive power sharing control

Fig. 4. 19 shows the movements of most affected poles when reactive power / frequency droop control k_q increases from 0.001 rad./(s·MVAr) to 18.001 rad./(s·MVAr) with the step of 2 rad./(s·MVAr). When k_q increases to 18.001 rad./(s·MVAr), some poles are in the right-half plane, indicating potential instability of the system.

Fig. 4. 20 shows the PSCAD simulation results when k_q changes from 18 rad./(s·MVAr) to 16 rad./(s·MVAr) at 0.4s. As can be seen, the system is unstable before 0.4 s but becomes stable after 0.4 s, as agreed with the root locus analysis in Fig. 4. 19.

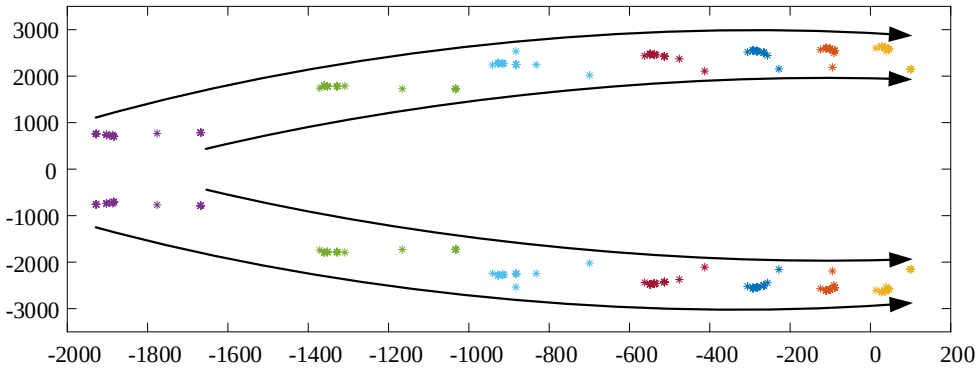

Fig. 4. 19 Root locus when k_q increases from 0.001 to 18.001 by step of 2.

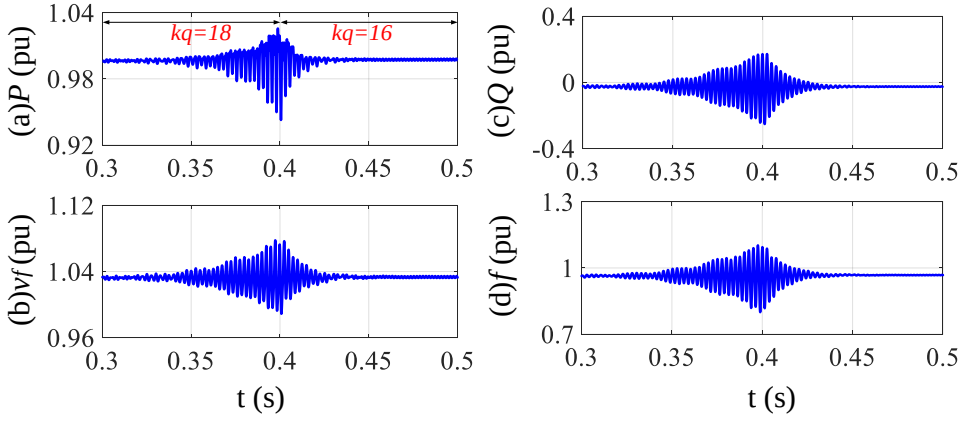

Fig. 4. 20 PSCAD results for WT1 when k_q steps from 18 to 16 at 0.4 s: (a) WT active power; (b) WT AC voltage; (c) WT reactive power; (d) WT frequency.

4.7 Summary

A small-signal state-space model of WTs connected with DR-HVDC systems has been developed in this chapter. Using the developed small-signal model, wind farm level analysis has been conducted to clarify the interactions among active and reactive powers, offshore AC voltage and frequency for better understanding of the system operation and control requirement. It shows that compared with frequency, AC voltage magnitude has a more significant effect on both active and reactive power in DR-HVDC connected wind farms. Therefore, wind farm AC voltage is selected as the control variable to regulate the wind farm active power, while reactive power / frequency droop control is used to share the reactive power among WT converters due to the same steady state frequency across the whole offshore network. Besides, WT level analysis has been carried out to reveal the mechanism of individual WT power transmission to offshore AC network, with the adopted *P*-*V* and *Q*-*f* control scheme. It is found that the change of WT transmitted active power is mainly dependent on the variation of phase angle difference as in a conventional power network, although the wind farm level shows the transmitted active power of DR depends on the variation of wind farm PCC AC voltage magnitude. In addition, the proposed angle compensation control effectively alleviates the coupling between WT active power and reactive power. Frequency-domain Bode responses and time-domain simulations verify the effectiveness of the proposed control. Stability analysis has been carried out to derive the stability range of the angle compensation control, active power control and reactive power control parameters.

Chapter 5 Fault performances of offshore wind farms connected with DR-HVDC systems

This chapter presents the operation of WTs connected with DR-HVDC systems during various faults including onshore AC faults, offshore AC faults and DC faults. Active DC voltage control of onshore MMC combined with a WT overvoltage limiting control is proposed during onshore AC faults, to reduce wind farm active power generation so as to alleviate the MMC submodule capacitor overvoltage. A fault current limiting method is also proposed, not only to ensure the operation of WTs during offshore AC faults but also facilitate the offshore fault detection. A simple and effective offshore AC fault overcurrent protection solution is further proposed to isolate the offshore faults. In addition, system responses after permanent DC pole-to-pole faults are investigated. Simulation results in PSCAD verify the proposed strategy under onshore and offshore AC faults and DC fault conditions.

5.1 Onshore AC fault ride-through

Fig. 5. 1 illustrates the simplified layout of the system and the three different types of faults are referred to onshore AC fault (F1), offshore AC fault at one of the WT clusters (F2) and DC cable pole-to-pole fault (F3). This section presents the behaviours and fault ride-through strategies during onshore faults (F1).

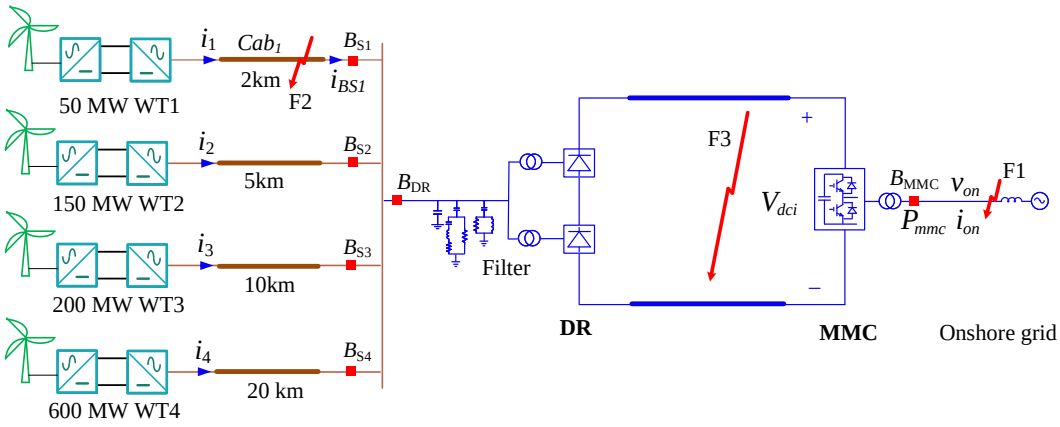

Fig. 5. 1 Onshore faults, offshore faults and DC faults of the DR-HVDC systems.

5.1.1 Onshore AC fault characteristics

When onshore AC faults happen, the onshore AC voltage drops. As a result, the onshore MMC power transmission capability is significantly reduced. Consequently, the MMC might operate on current limiting control. If offshore DR still tries to transfer the generated wind power to the DC link, this can lead to the active power unbalance between the DC and onshore sides. The surplus power can result in overvoltage in the DC cable and onshore MMC submodule capacitors. However, it is desirable that the offshore system and the DR-HVDC can remain operational, continue transmitting active power from WTs (if possible) and support the onshore AC grid [61].

If the DC link voltage of the MMC station is controlled at a constant value by reducing the number of inserted submodules after the faults, WT converters and DR will continue delivering generated active power. This constant active power unbalance can result in excessive overvoltage in the MMC submodules capacitor and potentially lead to system disconnection. Fast communication may need to be used to reduce the WT power generation to achieve active power re-balance between offshore and onshore sides.

An alternative solution is to increase the DC voltage during the onshore faults. As WT converters try to export the generated active power by increasing their terminal AC voltages (the *P*-*V* control), the DC voltage increase is propagated to the offshore AC side, leading to the increase of offshore AC voltage. Thanks to the AC voltage loop designed in each WT control system, the offshore overvoltage can be limited by setting a maximum *d*-axis voltage value $v_{fdref\max}$, as presented in Fig. 3. 4. When the DC voltage is increased to $3.31T_{dr}v_{fdref\max}$ while the offshore AC voltage is limited by the WT controller at $v_{fdref\max}$, the DR ceases conduction. Therefore, the WT active power is reduced automatically until the active power re-balance between the offshore and onshore sides is achieved. Hence, no fault detection, control mode switching or communication is required for the proposed method to ride-through the onshore faults. The $v_{fdref\max}$ used to limit the overvoltage is set as

$$v_{fdref\max} = k_{vo}v_{fd\_rated} \tag{5.1}$$

where v_{fd_rated} is the converter rated *d*-axis voltage and k_{vo} defines the over-voltage capability of the offshore network which is set at 1.1 in this thesis. When the WT converters operate on the overvoltage limiting control mode during onshore faults, the WT active power control loop saturates. The surplus energy at each WT is dealt locally as part of WT fault ride-through requirement, e.g. using DC damping resistors[63].

As can be seen, for the DR-HVDC systems with WT offshore AC overvoltage limiting control, there is an intrinsic negative feedback loop after onshore faults that the unbalanced active power can be automatically curtailed. The amount of power transmitted from the offshore wind farms after the faults is largely determined by the DC voltage of the HVDC system. If the DC voltage can be increased quickly at the initial stage of the fault, WTs will work on the overvoltage limiting control mode more quickly and active power re-balance can be achieved faster, leading to reduced capacitor overvoltage in the MMC submodules. Two different DC voltage increase methods (passive and active) during onshore faults will be further described in the following sub-sections.

5.1.2 Passive MMC DC voltage control

One general solution for the MMC to control the DC voltage, defined as passive MMC DC voltage control, is to keep the total number of inserted upper and lower arm submodules in each phase (N) constant [23, 26, 116, 120]. The number of inserted MMC submodules in the upper arm and lower arms is thus designed as [121, 122]

$$n_{up} = \frac{N}{2} - \frac{N}{2} M \sin wt \tag{5.2}$$

$$n_{dowm} = \frac{N}{2} + \frac{N}{2} M \sin wt \,. \tag{5.3}$$

In this case, its DC voltage is the sum of the inserted submodule capacitor voltage, even during the onshore faults, expressed as

$$V_{dci} = \left(n_{up} + n_{dowm} \right) V_{sm} = N V_{sm} \,. \tag{5.4}$$

As can be seen, the increase of DC link voltage (ΔV_{dci}) is determined by the submodule capacitor voltage increase (ΔV_{sm}) during onshore faults, expressed as

$$\Delta V_{dci} = V_{dci} - V_{dc0} = N\left(V_{sm} - V_{smref}\right) = N\Delta V_{sm} \tag{5.5}$$

where ΔV_{sm} is caused by the energy unbalance between offshore and onshore sides.

5.1.3 Active MMC DC voltage control

As discussed before, faster DC voltage increase leads to faster active power re-balance. Thus, the energy absorbed by the MMC submodule capacitors can be reduced, alleviating excessive overvoltage of the submodules.

If the relation between the DC link voltage increase and submodule capacitor voltage increase can be modified as

$$\Delta V_{dci} = kN\Delta V_{sm}, \qquad k > 1 \tag{5.6}$$

with the same submodule capacitor voltage increase, the DC voltage can be increased faster during the onshore faults. This can be achieved by adding more additional submodules in the upper and lower arms of each phase during the fault period. Based on this observation, an active MMC DC voltage control is proposed to automatically increase the DC voltage after the onshore faults, as shown in Fig. 5. 2.

As the DC voltage under this scheme is

$$V_{dci} = V_{dc0} + \Delta V_{dci} = NV_{smref} + kN\Delta V_{sm} = NV_{smref} + kN\left(V_{sm} - V_{smref}\right) \tag{5.7}$$

to implement this active MMC DC voltage control, the number of inserted MMC submodules in the upper arm and lower arms is modified as

$$n_{up} = \frac{NV_{smref} + kN\left(V_{sm} - V_{smref}\right)}{2V_{sm}} - \frac{N}{2}M\sin wt \tag{5.8}$$

$$n_{dowm} = \frac{NV_{smref} + kN\left(V_{sm} - V_{smref}\right)}{2V_{sm}} + \frac{N}{2} M \sin wt \tag{5.9}$$

As illustrated in Fig. 5. 2, a limiter is used in the proposed control to limit the maximum DC overvoltage of the DR-HVDC link to an acceptable value. After the DC voltage hits the limit, the number of inserted submodules per phase starts to decrease with the increase of submodule capacitor voltage. In this way, the HVDC link overvoltage is regulated at the pre-set maximum value to ensure safe operation of the HVDC link.

After the fault clearance, the onshore AC voltage restores and more active power can be exported from the MMC to the onshore grid. This leads to the reduction of the voltages of the submodule capacitor and DC link. Subsequently, the DR-HVDC systems and offshore wind generation can quickly recover.

It should be noted that the proposed control, when k > 1, also works in normal operation (as both ΔV_{sm} and ΔV_{dci} equal 0) and does not have any negative influence on the normal operation. The passive control in fact is a specific case of the proposed active control where k is set at unity. Hence, no fault detection, control mode switching or communication is required for the proposed control.

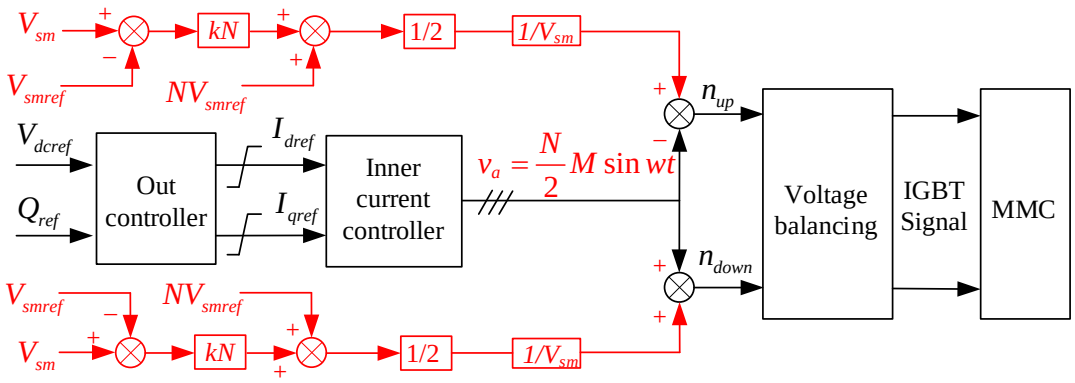

Fig. 5. 2 Active MMC DC voltage control scheme.

5.2 Offshore AC fault ride-through

This section presents the behaviours and fault ride-through strategies during offshore faults (F2, Fig. 5. 1).

5.2.1 Offshore AC fault characteristics

When offshore AC faults happen, the offshore AC voltage drops. With the DC link voltage maintained at the nominal value by the onshore MMC, the offshore diode rectifier will cease conduction when the offshore AC voltage is lower than its minimum conduction voltage of $V_{dci}/2.7T_{dr}$. Consequently, no active power can be transmitted through the DR-HVDC link.

When the offshore AC voltage decreases during the faults, both WT active power control loop and *d*-axis AC voltage control loop saturate, thus the WTs operate on the current limiting control mode.

5.2.2 Fault current limiting control

To ensure the WT converter current does not exceed its maximum value and provide the protection system with the capability of offshore fault detection, WTs should provide sufficient offshore fault current instead of reducing the currents to 0. The maximum and minimum limits for the *d*-axis (active) and *q*-axis (reactive) currents are set as

$$i_{wqref\,\max} = k_o I_{rated}, \qquad i_{wqref\,\min} = -k_o I_{rated} \tag{5.10}$$

$$i_{wdref\,\max} = \sqrt{\left(k_o I_{rated}\right)^2 - \left(i_{wqref}\right)^2}, \qquad i_{wdref\,\min} = 0 \tag{5.11}$$

where I_{rated} is the converter rated current and k_o defines the over-load capability of the WT converters, which is set 1.3 pu in this chapter. As seen in (5.10), the reactive current is set as priority, in order to ensure the offshore frequency remains around 1 pu during the offshore faults [85, 89]. With the increase of *q*-axis current reference i_{wqref}, the *d*-axis current reference i_{wdref} reduces according to the dynamic limit depicted

by (5.11) to avoid converter overcurrent. As the active power can only flow from WTs to the offshore network, the minimum limit of the *d*-axis current $i_{wdref\,\min}$ is set at zero in (5.11) in order to avoid active power circulation among WT converters.

5.2.3 Offshore AC fault overcurrent protection

A. Layout of offshore protection circuit breakers

The offshore protection breakers are arranged as shown in Fig. 5. 1, to examine the coordination of the WT control and offshore fault detection scheme. Each aggregated WT is connected to the PCC through circuit breaker B_{Sj} (j=1, 2, 3, 4) for isolating the fault branch from the rest of the healthy offshore network. For example, the fault case F2 at the aggregated 50 MW WT1 should lead to the opening of breaker B_{S1}, isolating the faulty WT1 from the rest of the offshore network.

B. Overcurrent protection for the offshore AC faults

Although WT LSCs have the limited capability in terms of overcurrent (e.g. 1.3 pu), during offshore faults at one of the cables, substantial overcurrent can still be present as all the turbines will feed currents to the fault point. For example, when fault F2 applies at the cable Cab_1 as shown in Fig. 5. 1, all other healthy aggregated 150 MW WT2, 200MW WT3 and 600MW WT4 provide fault currents for breaker $B_{S1.}$ The fault current of circuit breaker B_{S1} during the faults is

$$i_{BS1} = -i_2 - i_3 - i_4. \tag{5.12}$$

The current flowing through B_{S1} is much higher than its nominal current. Thus, overcurrent protection can be adopted to detect the fault and open B_{S1} for fault isolation. The breakers on the healthy strings (B_{S2}-B_{S4}) do not experience overcurrent and thus remain unaffected:

$$i_{BSj} = i_j, \qquad j = 2, 3, 4. \tag{5.13}$$

Under the low wind conditions when many WTs are disconnected with the offshore network, backup protection [123] operates to detect the fault and leads to the opening of the breakers, but is not investigated here.

5.3 Response to DC pole-to-pole permanent faults

After solid pole-to-pole DC faults (F3, Fig. 5. 1), the DC voltage of DR-HVDC collapses. The onshore MMC will be blocked immediately when the overcurrent is detected. However, due to the current flowing from onshore AC grid to the fault point through the diodes in the MMC submodules, DC current will continue increasing. The onshore AC breaker B_{MMC} is then opened to disconnect the MMC with the AC grid.

Due to the use of diode rectifier, the DC faults are also propagated to the offshore AC network. The faults on the DC side of the DR-HVDC appear similar as short-circuits for the offshore AC grid, leading to a significant drop of offshore AC voltage. The operation of the WTs during the DC faults is thus similar to that during offshore AC faults as described in Section 5.2. Both the WT LSC active power and *d*-axis voltage control loops saturate. Meanwhile, the *q*-axis WT LSC currents are increased to their maximum values whilst the *d*-axis currents are reduced to limit the fault currents. In several-ten milliseconds after the disconnection between onshore MMC and the onshore grid, and if offshore AC voltage does not recover, the WT converters may be blocked, as pole-to-pole DC cable faults are usually permanent and require the complete shutdown of the system.

5.4 Simulation results

The various fault performances of WTs connected DR-HVDC, and the corresponding proposed control and protection methods are assessed in PSCAD/EMTDC based on the model shown in Fig. 5. 1.

5.4.1 Onshore fault ride-through performances

A. Solid onshore fault ride-through performance

The performance of the active DC voltage control during a solid onshore fault is compared to that of the passive DC voltage control method, as shown in Fig. 5. 3.

During normal operation, both control methods operate satisfactorily. At 0.05 s, a solid three-phase onshore fault occurs at the transformer gird side and the onshore AC voltage v_{on} rapidly decreases to 0, as shown in Fig. 5. 3 (a). During the fault, the active current of the MMC is reduced using a voltage dependent current order limit (VDCOL) while its reactive current is increased [20], limiting the onshore current i_{on} at 1.1 pu, as shown in Fig. 5. 3 (b). The onshore transmitted active power P_{mmc} quickly reduces to 0 as shown in Fig. 5. 3 (h), whilst the WT and diode rectifier still try to transmit the generated active power, as shown in Fig. 5. 3 (f) and (g). This unbalanced active power leads to the charge of MMC submodule capacitors and consequently their voltages increase. Fig. 5. 3 (e) shows the average value of all the submodule capacitor voltages.

With the conventional passive DC voltage control method, both the average submodule voltage of the 6 arms V_{sm} and the DC link voltage V_{dci} increase from 1.0 pu to 1.29 pu within 0.04 s, as shown in Fig. 5. 3 (d) and (e). The increase of the DC voltage reduces the offshore diode rectifier AC power P_{dr} and transmitted DC power P_{dc}, as can be seen in Fig. 5. 3 (f) and (g). When the DC voltage reaches 1.29 pu, the offshore AC voltage reaches the maximum value at 1.1 pu controlled by the WT converters, and thus no active power can be generated and transmitted to the DC. The excess power in individual WT is dealt as part of WT fault ride-through strategy, e.g. using DC damping resistors so is not investigated here.

Using the proposed active DC voltage control method, the DC link voltage increases to 1.29 pu within the first 0.01 s as shown in Fig. 5. 3 (d), while the offshore AC voltage v_{pcc} hit the voltage limit of 1.1 pu more quickly, as shown in Fig. 5. 3 (c). The faster DC voltage increase yields faster reduction of wind power generation and the energy absorbed by the MMC submodules is decreased. As a result, the submodule overvoltage is only 1.12 pu with the proposed active control compared to 1.29 pu using conventional passive control, as shown in Fig. 5. 3 (e). At 0.2 s, the fault is cleared and the onshore AC voltage recovers, leading to the increase of onshore transmitted active power. As seen from Fig. 5. 3 (f), the wind power generation is also quickly restored.

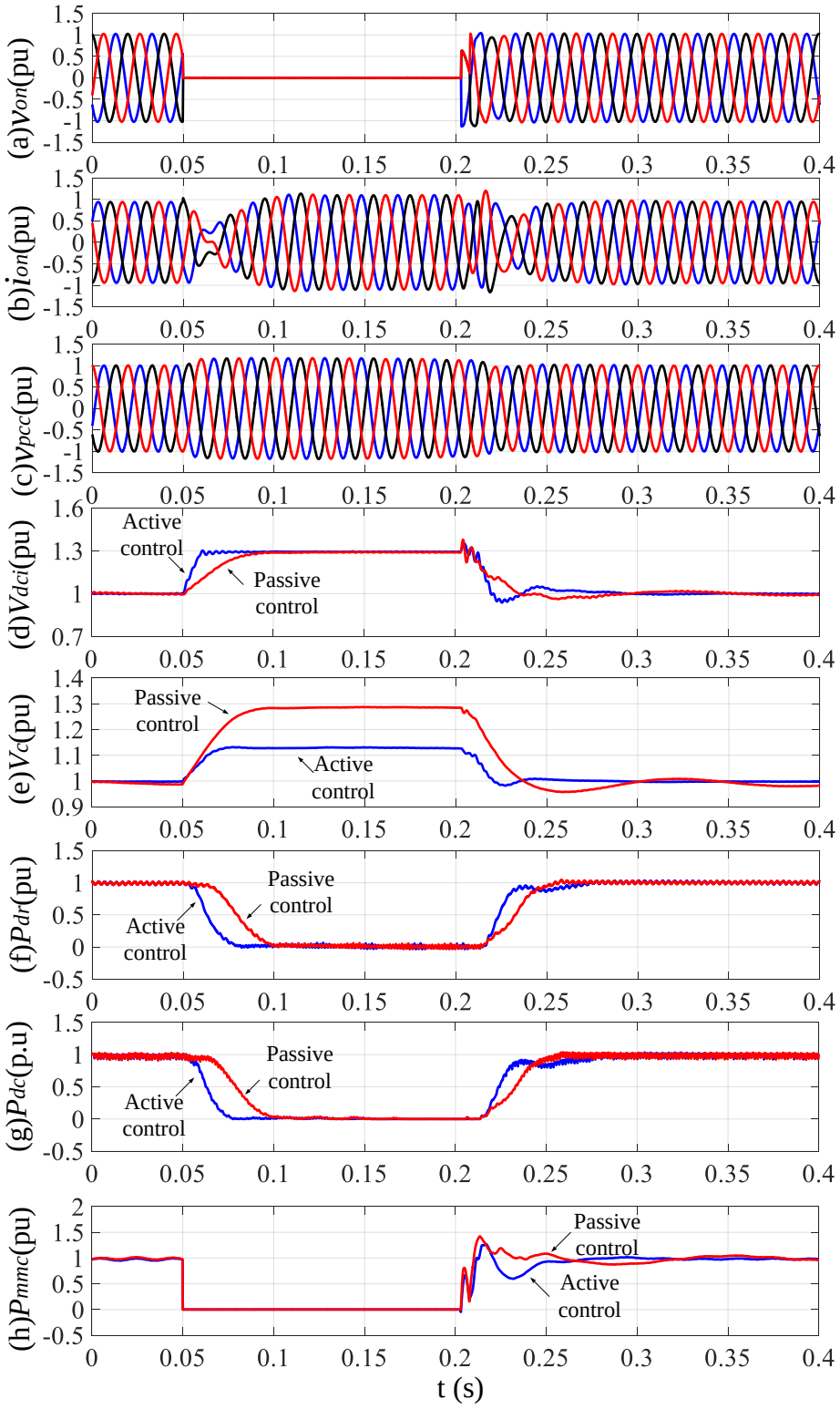

Fig. 5. 3 Performance of the DR-HVDC systems during a solid onshore fault: (a) onshore AC voltage; (b) onshore AC current; (c) offshore AC voltage; (d) DC voltage; (e) average MMC submodule capacitor voltage of six arms; (f) total WT transmitted active power; (g) DC power; (h) onshore transmitted active power.

B. Remote onshore fault ride-through performance

Fig. 5. 4 compares the two different control methods during a remote onshore fault (simulated with a 10Ω fault resistance). At 0.1 s, the remote onshore fault happens and the onshore AC voltage decreases to 0.5 pu, as shown in Fig. 5. 4 (a). During this fault, the onshore MMC limits its current at 1.1 pu, as shown in Fig. 5. 4 (b), while the active current of the MMC is reduced to 0.4 pu and its reactive current is increased to 1.025 pu to support the onshore voltage. The active power between the offshore and onshore side is unbalanced at the initial stage of the fault, as seen in Fig. 5. 4 (f) and (h), leading to the increase of MMC submodule capacitor voltage.

With the conventional passive DC voltage control method, both the average submodule voltage of the 6 arms V_{sm} and the DC link voltage V_{dci} increase from 1.0 pu to 1.2 pu, as shown in Fig. 5. 4 (d) and (e). The increase of the DC voltage reduces the diode rectifier AC power P_{dr} and transmitted DC power P_{dc} as can be seen in Fig. 5. 4 (f) and (g). When the DC voltage reaches 1.2 pu, the offshore AC voltage reaches the maximum value set by the WT converters (set at 1.1 pu) and thus active power between the offshore and onshore sides is re-balanced.

Using the proposed active DC voltage control method, the DC link voltage also increases to 1.2 pu, as shown in Fig. 5. 4 (d) and the offshore AC voltage v_{pcc} is quickly hitting the overvoltage limit of 1.1 pu, as shown in Fig. 5. 4 (c). The faster DC voltage increase yields faster reduction of wind power generation and thus the energy absorbed by the MMC submodules is decreased. As a result, the submodule average voltage is only 1.05 pu with the proposed active control compared to 1.2 pu using conventional passive control, as shown in Fig. 5. 4 (e).

At 0.25 s, the fault is cleared and the onshore AC voltage recovers, leading to the increase of onshore transmitted active power. As seen from Fig. 5. 4 (f), the wind power generation is also quickly restored.

The results presented in Fig. 5. 3 and Fig. 5. 4 show that the active DC voltage control method lead to lower submodule capacitor overvoltage during onshore faults when compared to the passive control method.

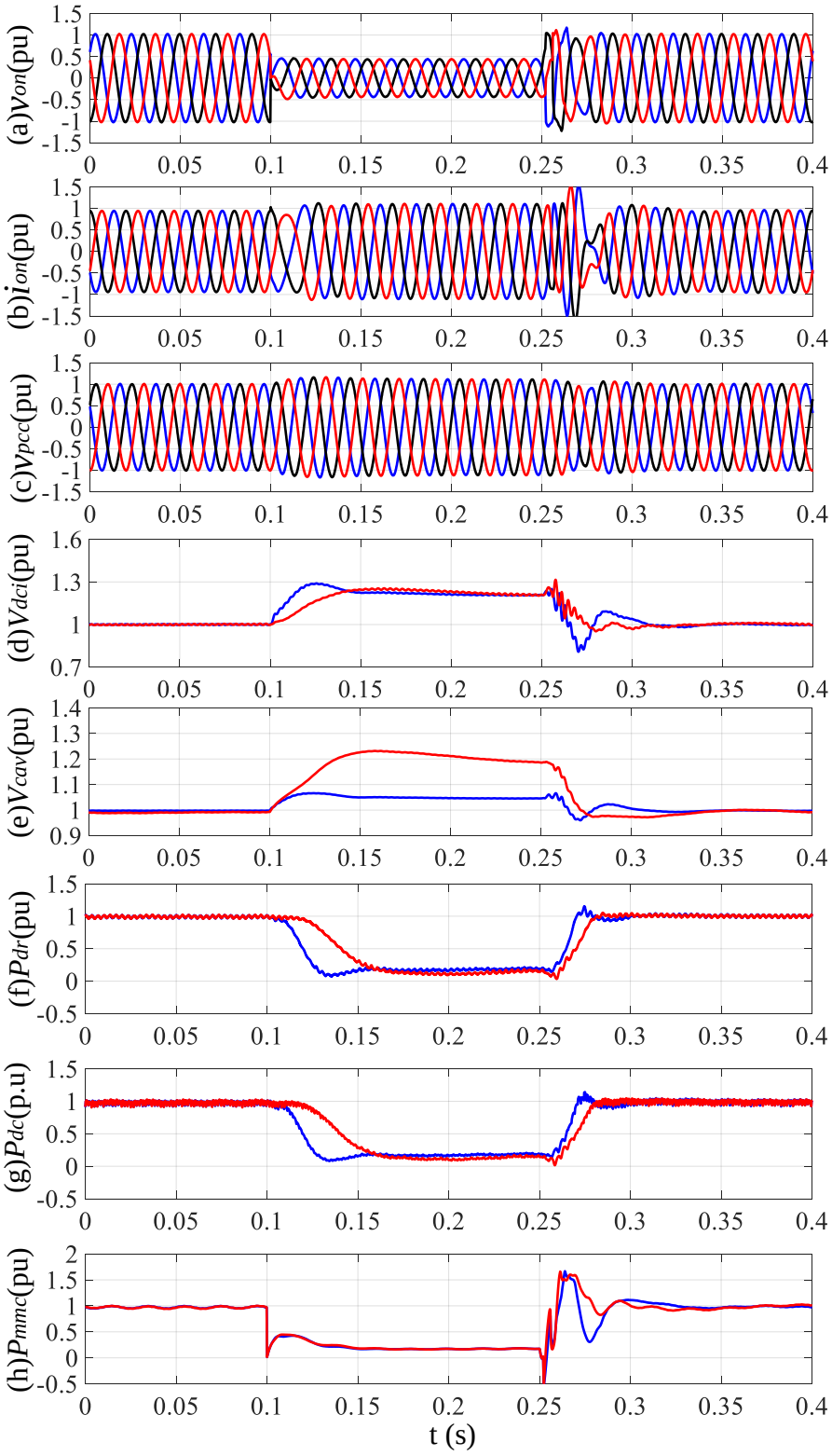

Fig. 5. 4 Performance of the DR-HVDC system during a remote onshore fault: (a) onshore AC voltage; (b) onshore AC current; (c) offshore AC voltage; (d) DC voltage; (e) average MMC submodule capacitor voltage of six arms; (f) total WT transmitted active power; (g) DC power; (h) onshore transmitted active power.

5.4.2 Offshore fault ride-through performances

A. Performance evaluation of the control strategy

To test the proposed control during an offshore AC fault, a solid three-phase fault F2 is applied at the cable Cab_1 at t=0.3 s and isolated by breaker B_{S1} at t=0.55 s.

As shown in Fig. 5. 5 (a), the offshore AC voltage collapses after the fault. The active power from the WT converters decreases immediately to 0, as shown in Fig. 5. 5 (d). As a result, the converters operate on current limiting mode where the q-axis current i_{wq} of each converter is quickly increased to provide fault current whereas the d-axis current i_{wd} reduces accordingly, as displayed in Fig. 5. 5 (f) and (g). Fig. 5. 5 (b) and (c) show the fault currents of WT1 and WT2, which are well controlled at the maximum currents by the WT controller assuming 30% overcurrent capability. During the entire simulation scenario, the reactive power is shared among the WT converters and the offshore frequency is largely controlled around the rated value of 50 Hz, as shown in Fig. 5. 5 (e) and (h), respectively. The DC power of the DR-HVDC decreases to 0 during the fault while the DC voltage slightly drops after the fault as no power is being transmitted from the diode rectifier, as can be seen in Fig. 5. 5 (i) and (j).

At 0.55 s, the fault is isolated by opening breaker B_{S1}, WT1 is then blocked and its current drops to 0 as seen from Fig. 5. 5 (b), while the offshore voltage is restored as seen in Fig. 5. 5 (a). Meanwhile, the currents and powers of other healthy WTs start to recover to rated values, as shown in Fig. 5. 5 (c) and (d). As seen from the Fig. 5. 5 (j), the wind power transmission through the DR-HVDC is also quickly restored.

Fig. 5. 5 demonstrates the WT converters automatically operate on current limiting mode during the offshore fault and can provide fault currents. It will enable the offshore overcurrent protection to detect and isolate the faults, without the use of communication between the WTs and the offshore protection breakers, as will be demonstrated in the next sub-section.

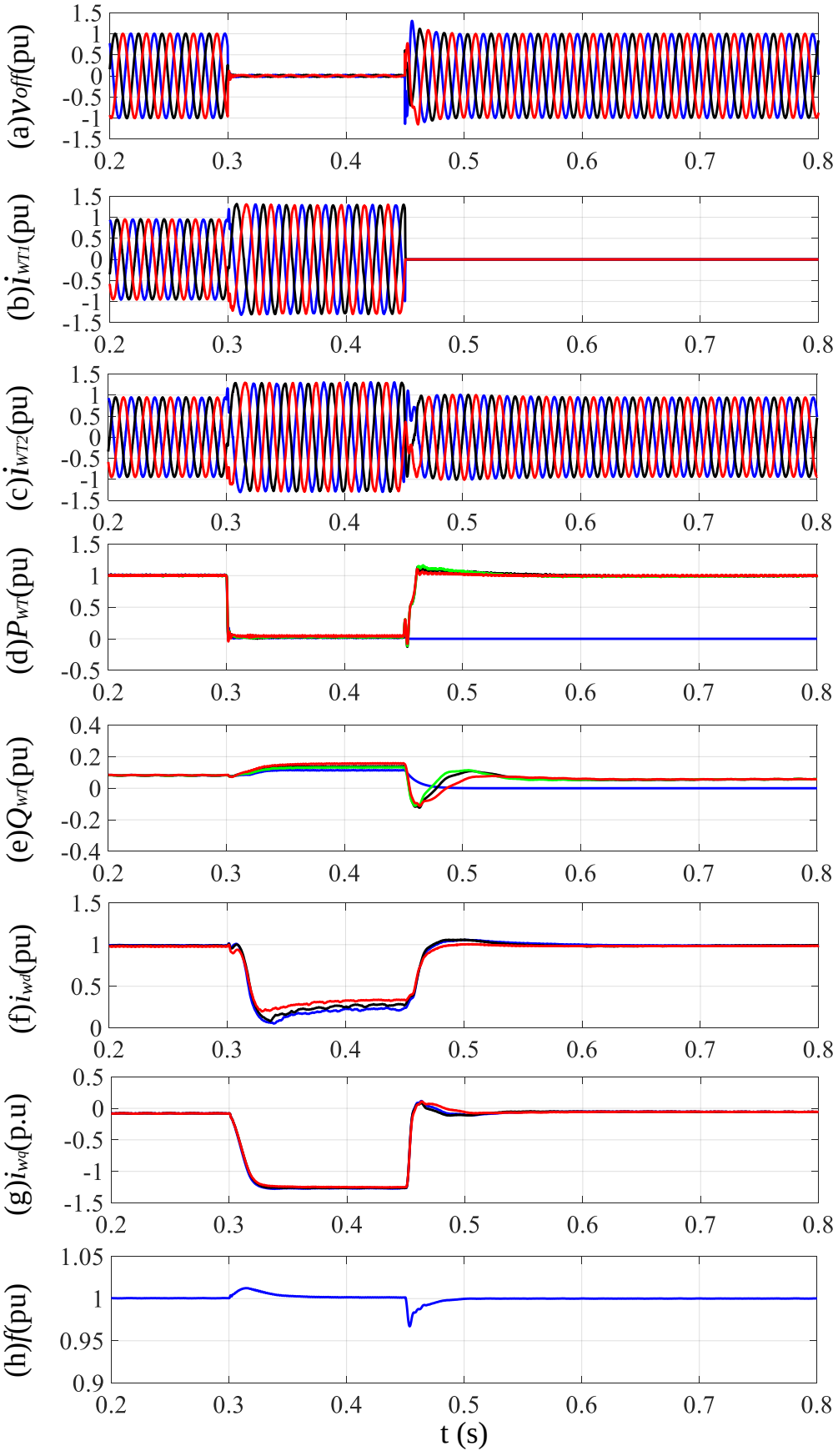
(a)v_{off}(pu)
(b)i_{WT1}(pu)
(c)i_{WT2}(pu)
(d)P_{WT}(pu)
(e)Q_{WT}(pu)
(f)i_{wd}(pu)
(g)i_{wq}(p.u)
(h)f(pu)
t (s)

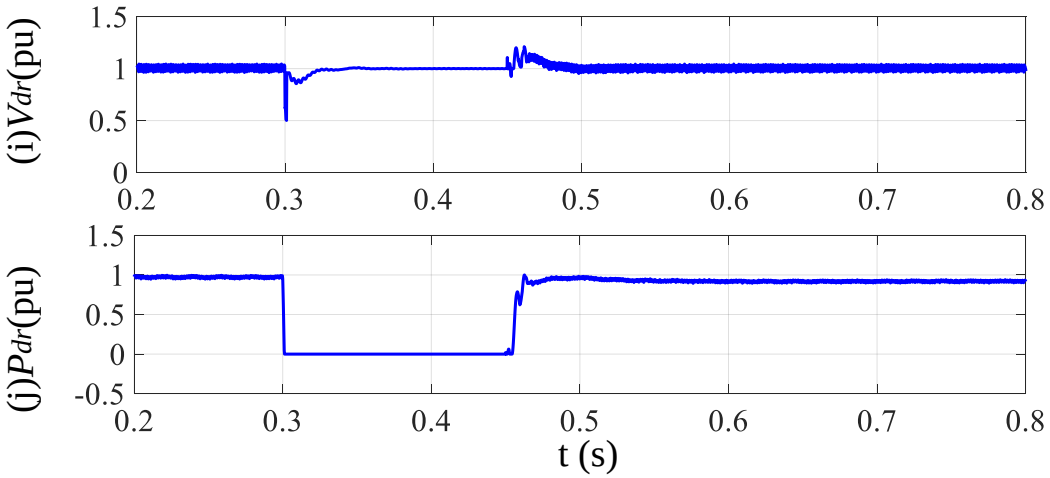

Fig. 5. 5 Simulation results during a solid offshore fault F2: (a) three-phase voltage, (b) three-phase current of WT 1, (c) three-phase current of WT 2, (d) WT active power, (e) WT reactive power, (f) d-axis current, (g) q-axis current, (h) frequency, (i) DR-HVDC link voltage, (j) DR-HVDC link power.

B. Performance evaluation of proposed protection scheme

After the offshore fault F2, each WT current is controlled at 1.3 pu (based on their respective power rating), as previously presented in Fig. 5. 5. WT 2, 3 and 4 feed currents through respective circuit breaker B_{S2}, B_{S3} and B_{S4} to the fault point. Thus, the currents of B_{S2}, B_{S3} and B_{S4} are at 1.3 pu respectively, as shown in Fig. 5. 6 (b), (c) and (d). On the other hand, B_{S1} experiences high overcurrent, as shown in Fig. 5. 6 (a). When instantaneous overcurrent relay is used to detect the fault, which operates instantaneously when the absolute value of one phase current exceeds the pickup value, the fault can be isolated by opening breakers B_{S1} in several tens of milliseconds. To clearly demonstrate the system behaviours during the offshore fault, circuit breakers are opened in 150 ms after the fault initiation in this study. According to overcurrent fault detection, breaker B_{S1} is opened at t=0.45 s while all other breakers do not experience overcurrent and thus remain closed.

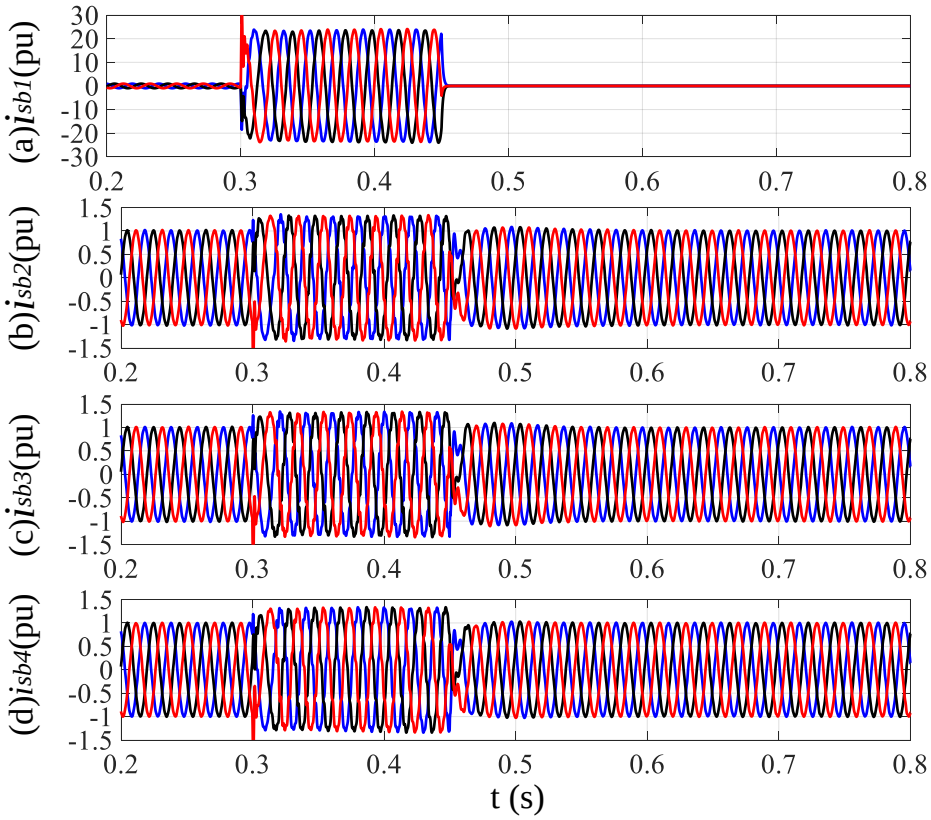

Fig. 5. 6 Three phase currents flowing through circuit breakers during a solid offshore fault F2: (a) breaker B_{S1} on the faulty cable, (b) breaker B_{S2} on the healthy cable, (c) breaker B_{S3} on the healthy cable(b) breaker B_{S4} on the healthy cable.

5.4.3 Performance during pole-to-pole DC faults

The system performance is assessed in this sub-section when a permanent solid pole-to-pole DC fault (F3, Fig. 5. 1) is applied at the middle of the DC cable at 0.3 s.

The DC link voltage drops to zero immediately after the fault, as shown in Fig. 5. 7 (a). 3 ms after the fault happens, MMC is blocked to prevent the half-bridge submodule discharge. However, the MMC DC current still increases to 5 pu, as shown in Fig. 5. 7 (b), due to the current from onshore AC grid feeding into the fault point through the diode bridges in the blocked MMC. At 0.35 s, the onshore AC breaker is opened, and thus the DC current of the MMC gradually reduces to 0. Similar to the DC voltage decrease of the MMC side after the DC fault, the DC voltage of diode rectifier also drops to 0, as shown in Fig. 5. 7 (c). Consequently, the diode rectifier DC

current is increased and transmitted active power is decreased to 0, as shown in Fig. 5. 7 (d) and (e).

Due to the use of diode rectifier, the DC fault is propagated to the offshore AC network. As a result, the offshore AC voltage drops to around 0.2 pu, as shown in Fig. 5. 7 (f). The active powers of WT converters decrease immediately to 0, as shown in Fig. 5. 7 (h) and the converters operate on current limiting mode. The *q*-axis current i_{wq} of each converter is quickly increased whereas the *d*-axis current i_{wd} reduces to avoid converter overcurrent damage, as shown in Fig. 5. 7 (j) and (k). As displayed in Fig. 5. 7 (g), the fault current of each WT converter is well controlled at the maximum current of 1.3 pu. During the DC fault, the reactive power is also well shared among the WTs and the offshore frequency is still around 50 Hz, as shown in Fig. 5. 7 (i) and (l).

Fifty milliseconds after the onshore AC breaker is tripped and offshore AC voltage does not recover (at 0.4 s in this simulation), the WT converters are blocked and the offshore AC network is de-energized considering the DC fault is permanent.

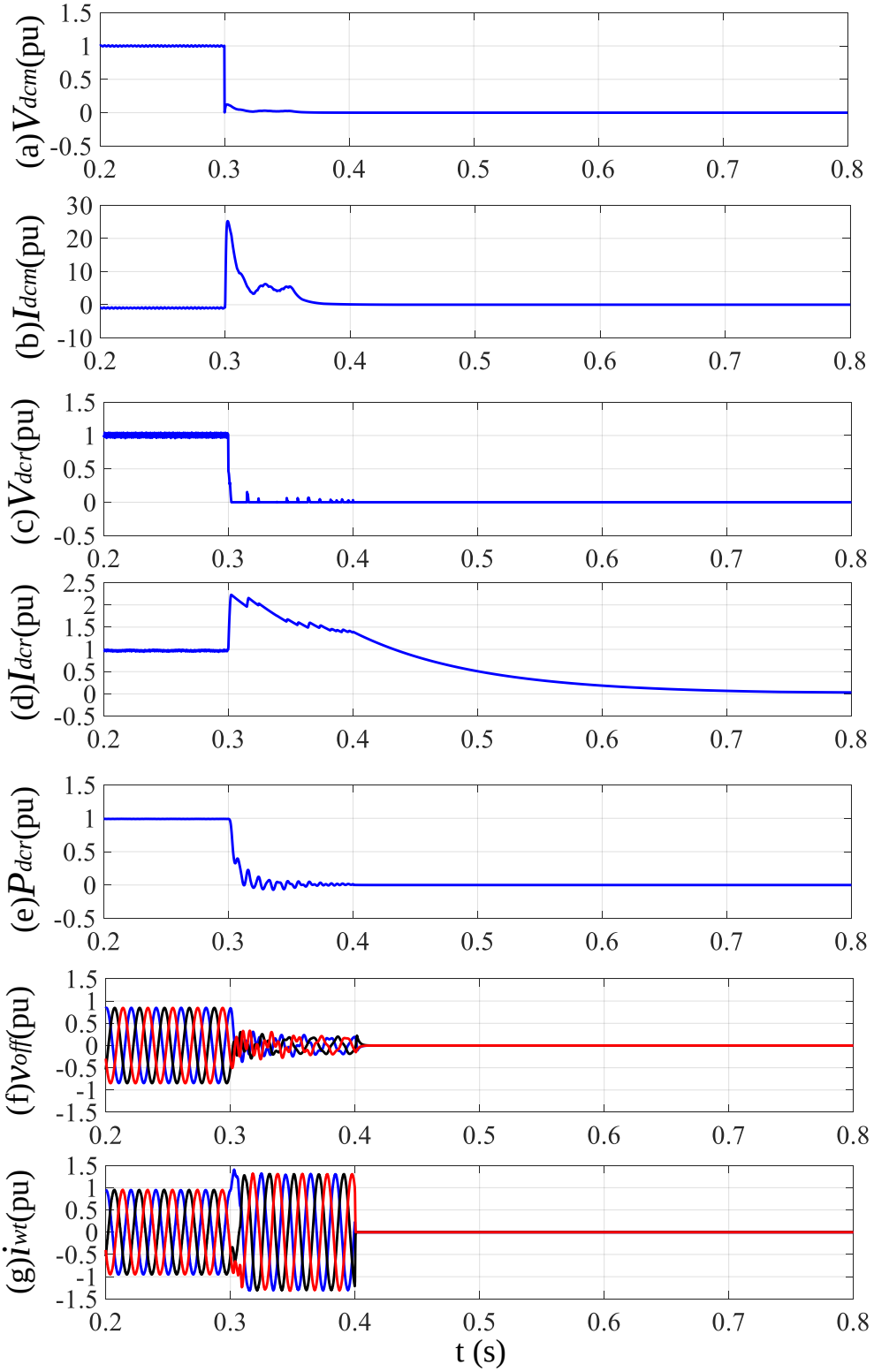
(a)V_{dcm}(pu)
(b)I_{dcm}(pu)
(c)V_{dcr}(pu)
(d)I_{dcr}(pu)
(e)P_{dcr}(pu)
(f)v_{off}(pu)
(g)i_{wt}(pu)
t (s)

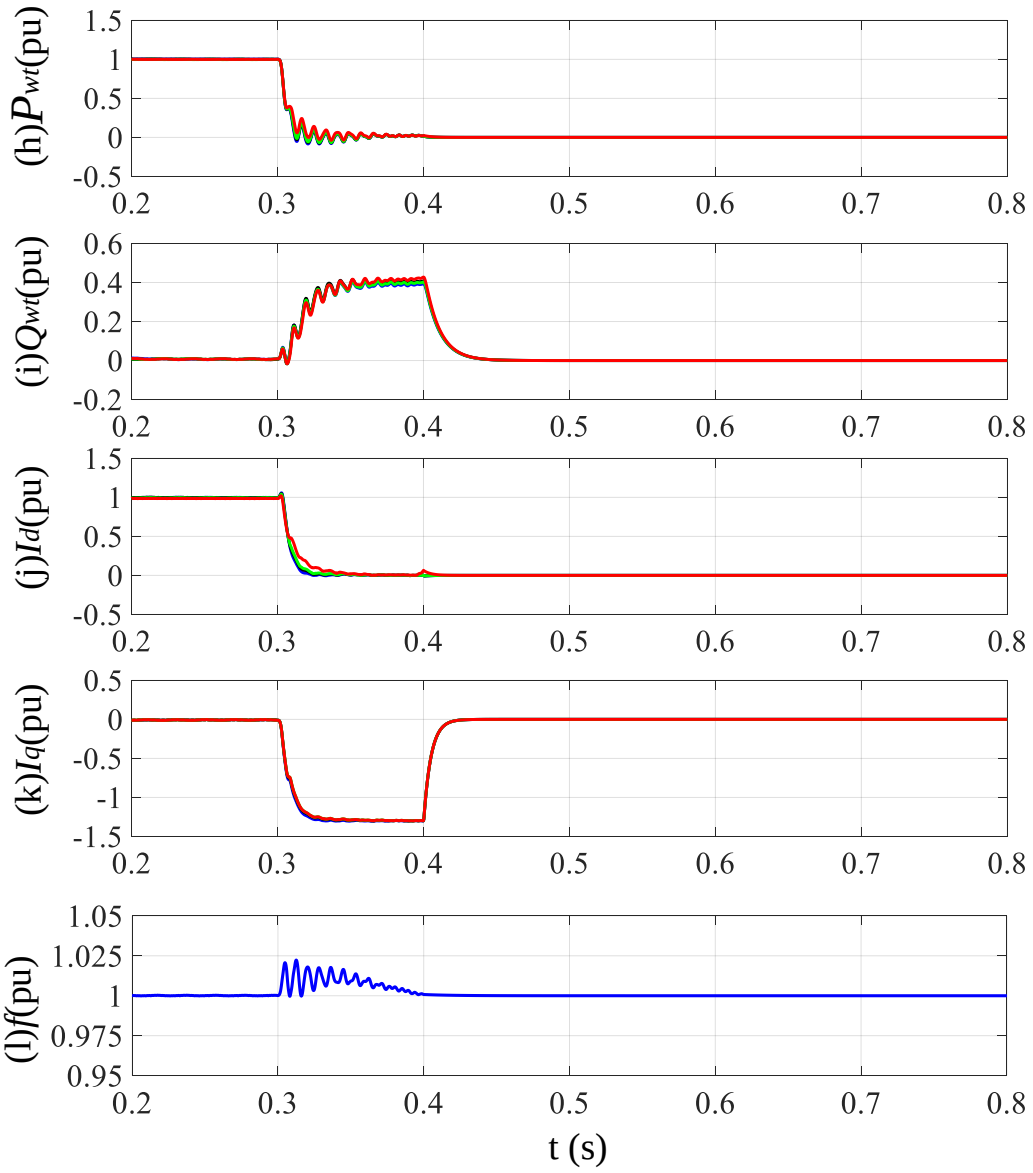

Fig. 5. 7 Simulation results of the system during a pole-to-pole DC cable fault: (a) MMC DC votlage, (b) MMC DC current, (c) diode rectifier DC voltage, (d) diode rectifier DC current, (e) diode rectifier active power, (f) offshore PCC voltage, (g) WT current, (h) WT active power, (i) WT reactive power, (j) WT active current, (k) WT reactive current, (l) offshore frequency.

5.5 Summary

The performances and control strategies of WTs connected with DR-HVDC during onshore AC faults, offshore AC faults and DC faults have been investigated in this

chapter. To ride-through onshore AC faults, an active onshore MMC DC voltage control method combining with a WT overvoltage limiting control is proposed. By inserting additional MMC submodules to temporarily increase the DC link voltage, the WTs quickly operate on offshore AC overvoltage limiting control mode and thus power transmission from offshore wind farms through the diode rectifier can be reduced more quickly. Active power re-balance between the offshore and onshore side is thus achieved faster and the MMC submodule capacitor overvoltage is reduced. During offshore AC faults, a fault current limiting method is proposed to ensure the safe operation of WTs where the reactive current is set as priority to ensure offshore frequency control while the active current reduces accordingly in order to avoid converter overcurrent. A simple and effective offshore AC fault overcurrent protection solution is proposed to detect and isolate the offshore AC faults. In addition, the system response during permanent DC pole-to-pole faults have been investigated. Due to the use of diode rectifier, the DC faults are propagated to the offshore AC network. The WT performances during the DC faults are similar to those under offshore AC faults. Simulation results verify the performances with the proposed control strategy of DR-HVDC connected WTs during different fault conditions.

Chapter 6 Parallel operation of DR-HVDC link and HVAC link

This chapter investigates the operation of offshore wind farms under different modes, i.e. DR-HVDC mode when offshore wind farms are only connected with DR-HVDC link, HVAC mode when offshore wind farms are only connected with HVDC link, and parallel mode when offshore wind farms are connected with both links. A WT LSC hierarchical control structure, which consists of primary control, secondary voltage control, secondary frequency control, phase angle control and tertiary power flow control, is proposed to ensure the operation under different modes and the smooth transition between them. With the secondary voltage control, the offshore AC voltage amplitude is able to match that of the HVAC link through the regulation of the DR-HVDC link DC voltage. With the secondary frequency control and phase angle control, the offshore PCC frequency and phase angle are able to synchronize to those of the HVAC link. Therefore, seamless transition from DR-HVDC mode to parallel mode can be achieved. With the tertiary power control, the active power flow distribution between DR-HVDC and HVAC links on parallel mode is controlled through the regulation of PCC phase angle. With the virtual DC power control, the virtual DC power is controlled at zero prior to the connection of the DR-HVDC link, to ensure smooth transition from HVAC mode to parallel mode. A small-signal model of the parallel system is developed and the stability analysis is carried out for the proposed control scheme. Simulation results in PSCAD/EMTDC verify the proposed control under normal and fault conditions.

6.1 Parallel operation of the systems

DR-HVDC provides a potential solution for offshore wind power transmission due to its attractive advantages of significantly reduced losses, capital cost and volume as presented in chapter 2. However, initial energization of the offshore wind farms during the start-up is a challenge due to the unidirectional of the DR-HVDC link. To overcome this problem, umbilical AC cables operating in parallel with the DR-HVDC link are used to energize the offshore network [15]. In addition, parallel operation of

an additional DR-HVDC link with an existing HVAC link is proposed to test of the new grid connection solution [110]. Thus, in case of any problem, the DR-HVDC link can be disconnected during the test while the offshore wind power can still be transmitted through the HVAC link. Besides, the future may see the interconnection of neighbouring offshore wind farms in the North Sea and Baltic Sea, similar to 'Kriegers flak-combined grid solution' project [124, 125]. Such interconnection may result in the parallel operation of HVDC and HVAC links for offshore wind power transmission to two independent onshore grids.

6.1.1 System structure

Fig. 6. 1 shows the layout of DR-HVDC and HVAC links connected offshore wind farms, which consists of 150 WTs each rated at 8 MW. The DR-HVDC link is rated at 800 MW (two-third of the total wind power) and ±320 kV DC, while the HVAC link is rated at 150 kV and one-third (400MW) of the total wind power, and connected with the wind farms via an offshore AC transformer.

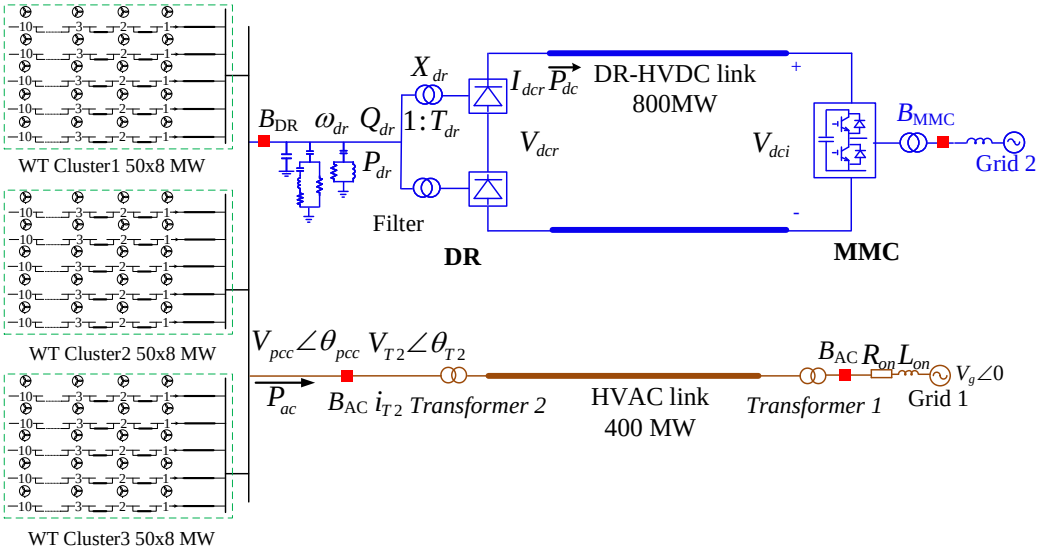

Fig. 6. 1 Diagram of the offshore wind farms connected with DR-HVDC and HVAC transmission systems.

6.1.2 Operation modes

Depending on the connection of transmission links, the system operation modes can be classified as:

- HVAC mode: wind power is only transmitted through the HVAC link while the DR-HVDC link is disconnected from the offshore wind farms.
- DR-HVDC mode: wind power is only transmitted through the DR-HVDC link while the HVAC link is disconnected from the offshore wind farms.
- Parallel mode: the offshore wind farms are connected to both DR-HVDC and HVAC links. Wind power can be transmitted through both links according to operation requirements.

6.1.3 Control functions

To ensure efficient operation under different modes, the control functions of the parallel system include:

- Wind power generation according to WT operation requirements under all system operation modes.
- WTs establishing offshore voltage and frequency under DR-HVDC mode.
- Power flow control between DR-HVDC link and HVAC link under parallel mode.
- Smooth transition between DR-HVDC mode to parallel mode.
- Smooth transition between HVAC mode to parallel mode.

In order to meet the aforementioned operation requirements, a hierarchical control structure which includes primary, secondary and tertiary controls, is proposed in this chapter. The primary control provides WT with active power and reactive power control under all operation modes and maintains the offshore voltage and frequency on DR-HVDC mode. The secondary control regulates the offshore voltage magnitude, frequency and phase angle to achieve smooth transition from HVAC mode to parallel

mode. The tertiary control adjusts the power flow between DR-HVDC link and HVAC link on parallel mode. The virtual DC power control regulates the virtual DC power at zero prior to the connection of the DR-HVDC link, to ensure smooth transition from HVAC mode to parallel mode. The detailed function and control will be described in the following sections.

6.1.4 Primary control

The primary control is designed in each WT converter to provide plug and play capability without the use of communication, as presented in chapter 3. In order to achieve smooth transition between different operation modes and to avoid primary control switching, the same WT converter primary control, as presented in chapter 3, is used for all the operation modes.

6.2 Secondary control

During the transition from DR-HVDC mode to parallel mode, it is important to ensure the matching of the voltage magnitude, frequency and phase angle between the offshore PCC voltage $V_{pcc}\angle\theta_{pcc}$ and HVAC link voltage $V_{T2}\angle\theta_{T2}$ (shown in Fig. 6. 1), which will be investigated in this section.

6.2.1 Voltage and frequency deviation under DR-HVDC mode

Under DR-HVDC mode, the relationship between the offshore AC voltage V_{pcc}, the DC current I_{dcr} and offshore DC voltage V_{dcr} is expressed as [83]

$$V_{pcc} = \frac{V_{dcr}}{2.7T_{dr}} + \frac{3X_{dr}I_{dcr}}{1.35T_{dr}\pi} \tag{6.1}$$

where X_{dr} and T_{dr} are the reactance and turn ration of the diode rectifier transformer, respectively. The offshore DC voltage V_{dcr} and current I_{dcr} are expressed as

$$V_{dcr} = R_{dct} I_{dcr} + V_{dci}$$
$$I_{dcr} = \frac{P_{dr}}{V_{dcr}} \tag{6.2}$$

where P_{dr}, V_{dci} and R_{dct} are the DR transmitted wind power, onshore DC voltage and total DC resistance, respectively.

Combining (6.1) and (6.2), the offshore PCC voltage is rewritten as

$$V_{pcc} = \frac{V_{dci}}{2.7T_{dr}} + \frac{\left(R_{dct}\pi + 6X_{dr}\right)\left(-V_{dci} + \sqrt{V_{dci}^{\ 2} + 4R_{dct}P_{dr}}\right)}{5.4T_{dr}\pi R_{dct}} \ . \tag{6.3}$$

As can be seen, V_{pcc} is mainly determined by the generated active power P_{dr} and onshore MMC DC voltage V_{dci}, and V_{pcc} increases when the DR-HVDC transmitted wind power P_{dr} increases. The minimum offshore PCC voltage when the DR starts conducting is $V_{dci}/2.7T_{dr}$.

As the diode rectifier reactive power consumption Q_{dr} is coupled with its transmitted active power, expressed as [126]

$$Q_{dr} = P_{dr}\frac{\left(2\mu - \sin 2\mu\right)}{\left(1 - \cos 2\mu\right)}$$
$$\mu = \arccos\left(1 - \frac{2X_{dr}i_{dcr}}{T_{dr}V_{pcc}}\right) \tag{6.4}$$

the reactive power consumption of the diode rectifier varies with the generated wind power. As discussed in chapter 3, *Q-f* droop control is adopted in the WT primary control to regulate WT reactive power output. This results in the slight frequency deviation from the rated value during wind power variation under DR-HVDC mode.

6.2.2 Secondary offshore voltage control

As described in (6.3), offshore PCC voltage V_{pcc} under DR-HVDC mode is dependent on the transmitted active power P_{dr} and onshore MMC DC voltage V_{dci}. However, the DR-HVDC transmitted active power P_{dr} varies according to wind speed.

Thus, in order to ensure that the offshore PCC voltage magnitude V_{pcc} matches that of the HVDC link V_{T2} before switching to parallel mode (i.e. connecting the HVAC cables to the offshore wind farms), the onshore MMC DC voltage V_{dci} is adjusted. The proposed secondary offshore voltage control (shown in Fig. 6. 2), is expressed as

$$V_{dciref} = k_{svp}\left(V_{T2} - V_{pcc}\right) + k_{svi}\int\left(V_{T2} - V_{pcc}\right)dt + V_{dci0} \tag{6.5}$$

where V_{dci0} is the rated onshore MMC DC voltage, k_{svp} and k_{svi} are the control parameters of the secondary offshore voltage control. The onshore DC voltage reference V_{dciref} generated by the secondary voltage control is then sent to the onshore MMC by low bandwidth communication to adjust the DC voltage accordingly.

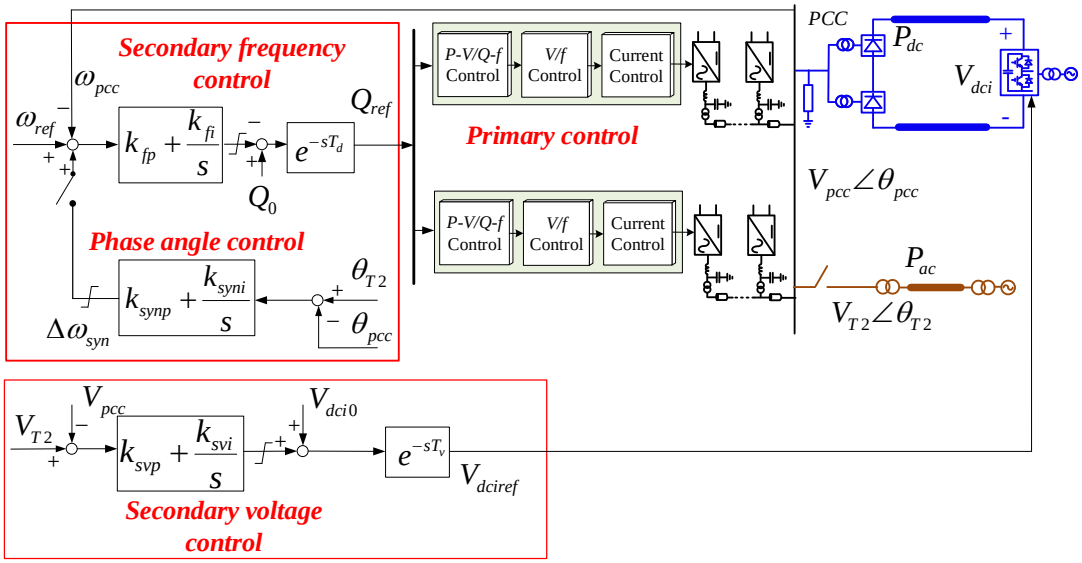

Fig. 6. 2 Proposed secondary control of WT converters.

6.2.3 Secondary offshore frequency control

Due to the use of *Q-f* droop in the WT primary control as presented in chapter 3, the reactive power reference Q_{ref} in the primary control shown in Fig. 6. 2 is adjusted to regulate the offshore frequency, as

$$Q_{ref} = -k_{fp}\left(\omega_{ref} - \omega_{pcc}\right) - k_{fi}\int\left(\omega_{ref} - \omega_{pcc}\right)dt + Q_0 \tag{6.6}$$

where k_{fp} and k_{fi} are the control parameters of the secondary frequency control. ω_{pcc} is the offshore PCC frequency and ω_{ref} is the desired offshore frequency equalling to the HVAC link frequency. When $\omega_{pcc} < \omega_{ref}$, the secondary frequency control produces a reduced Q_{ref} in the centralized controller, which is then sent to all the WT converters by low bandwidth communication. Consequently, the *Q-f* droop loop in the WT primary control leads to the frequency increase of each WT output. As a result, offshore PCC frequency ω_{pcc} is also increased until becoming identical to the reference ($\omega_{pcc} = \omega_{ref}$). Similarly, when $\omega_{pcc} > \omega_{ref}$, offshore PCC frequency is decreased to the reference by the combined functions of secondary frequency control and *Q-f* droop in the primary control.

6.2.4 Phase angle control

A secondary phase angle control is proposed by adding an adjustment term $\Delta\omega_{syn}$ to the frequency reference in the secondary offshore frequency control block (shown in Fig. 6. 2), as

$$\Delta\omega_{syn} = k_{synp}\left(\theta_{T2} - \theta_{pcc}\right) + k_{syni}\int\left(\theta_{T2} - \theta_{pcc}\right)dt \tag{6.7}$$

where k_{synp} and k_{syni} are the control parameters of the active synchronization control, θ_{T2} and θ_{pcc} are the voltage phase angles at the HVAC link and offshore PCC, respectively. As seen, when $\theta_{T2} > \theta_{pcc}$, the phase angle control produces a positive $\Delta\omega_{syn}$, leading to the increase of offshore PCC frequency ω_{pcc}. Consequently, θ_{pcc} is also increased until becoming identical to the reference ($\theta_{pcc} = \theta_{T2}$). Similarly, when $\theta_{T2} < \theta_{pcc}$, offshore PCC phase angle θ_{pcc} is decreased until $\theta_{pcc} = \theta_{T2}$.

6.3 Tertiary control

For the parallel transmission system, one particular challenge is power flow distribution between the two links. In [79], a phase-angle based active power control is implemented in offshore MMC to control the power flow when an MMC-HVDC link operates in parallel with an HVAC link. For the parallel operation of DR-HVDC and HVAC links, the diode rectifier is unable to provide the power flow control like

the MMC does. Thus, power distribution between the two links is controlled by the WT centralized controller, designed as a tertiary control to actively adjust phase angle difference between the offshore and onshore AC voltages connected by the HVAC link.

6.3.1 Active power control under parallel mode

As illustrated in Fig. 6. 3, the tertiary power flow control objective can either be HVAC link power or DR-HVDC power, as

$$\text{AC power control: } \omega_{ref} = k_{acp}\left(P_{acref} - P_{ac}\right) + k_{aci}\int\left(P_{acref} - P_{ac}\right)dt + \omega_0 \tag{6.8}$$

$$\text{DC power control: } \omega_{ref} = k_{dcp}\left(P_{dc} - P_{dcref}\right) + k_{dci}\int\left(P_{dc} - P_{dcref}\right)dt + \omega_0 \tag{6.9}$$

where P_{acref} and P_{ac} are the reference and measured HVAC link active power, P_{dcref} and P_{dc} are the reference and measured HVDC link active power, respectively. ω_0 is the rated offshore frequency while k_{acp}, k_{aci}, k_{dcp} and k_{dci} are the control parameters of the AC active power and DC active power control. In order to achieve smooth transition between AC active power control and DC active power control, the output of DC active power control is used as the lower limit of the AC active power control mode.

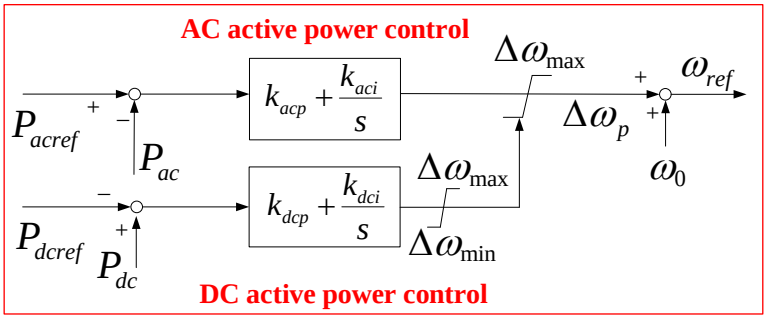

Fig. 6. 3 Proposed AC active power control and DC active power control.

A. AC active power control under parallel mode

Under low wind conditions when the total generated wind power is smaller than the rated power of DR-HVDC link, DC power control saturates (its output is $\Delta\omega_{min}$ during saturation) and the tertiary control works on AC active power control mode. Through the regulation of the offshore PCC phase angle, the HVAC link power is controlled to follow its reference P_{acref} at 0, so all the wind power is transmitted through the DR-HVDC link. During the change of the generated wind power, the controller keeps the offshore PCC phase angle largely unchanged meanwhile the offshore PCC voltage magnitude changes automatically to adjust the DR-HVDC active power transmission. If required, P_{acref} can also be set at a desired value to ensure certain power sharing between the two links.

B. DC active power control under parallel mode

Under high wind conditions, when the generated power exceeds the capacity of the DR-HVDC link, DC active power control starts to de-saturate while AC active power control saturates. With the DC active power control reference P_{dcref} at rated value, any overload of DR-HVDC link can be effectively avoid. During the change of the wind power, the DC active power controller regulates the offshore PCC phase angle to ensure the surplus wind energy is transmitted through the HVAC link. Similarly, P_{dcref} can also be set at a lower value to achieve certain power sharing between the AC and DC links if needed.

6.3.2 Virtual DC power control

During the transition from HVAC mode to parallel mode, active power transmitted through DR-HVDC link should remain largely unchanged before and immediately after the mode change so as to minimize any transients to the offshore networks. On HVAC mode operation, the DR-HVDC link is disconnected and does not transmit any power. Therefore, to ensure smooth transition, DR-HVDC active power should remain at 0 at the moment when the DR-HVDC link is connected.

According to (6.1) and (6.2), the transmitted active power through DR-HVDC link P_{dc} after the connection of DR-HVDC link is

$$P_{dc}=\frac{\left(2.7T_{dr}V_{pcc}R_{dct}+\frac{6}{\pi}X_{dr}V_{di}\right)\left(2.7T_{dr}V_{pcc}-V_{di}\right)}{(R_{dct}+\frac{6}{\pi}X_{dr})^{2}} \tag{6.10}$$

To ensure DC power remains at 0 after the mode transition, the "virtual DC power" concept is proposed, which considers a virtual DR-HVDC link is connected with the offshore network under HVAC mode. Thus, the virtual DC power can also be described by (6.10), which resembles the DR-HVDC transmitted power when the DC link is switched in. A virtual DC power control can then be designed, similar to the one in the tertiary control shown in Fig. 6. 3, with its power reference at 0 and feedback from the virtual DC power calculated by (6.10). Through the adjustment of WT reactive power output on HVAC mode, the PCC voltage is reduced to ensure the virtual DC power is 0. That means the DC power after the mode transition will also remain at 0, ensuring a smooth mode transition.

6.4 Stability analysis of the parallel systems

In order to analyse the system stability with the hierarchical control, a small-signal model is established and eigenvalues are derived to identify the impact of control parameters on the critical modes.

6.4.1 Small-signal modelling of the parallel systems

The offshore wind farms modelling and DR-HVDC link modelling have been presented in chapter 4, so only HVAC link modelling is described here. It mainly includes three parts: onshore grid with transformer 1, HVAC cable and offshore transformer 2, as shown in Fig. 6. 4.

The onshore grid with transformer 1 is represented as

$$\begin{cases}\left(L_{on}+L_{T1}\right)\dfrac{di_{ond}}{dt}=\omega\left(L_{on}+L_{T1}\right)i_{onq}+\dfrac{v_{ca1d}}{T_{ac1}}-v_{ond}-R_{on}i_{ond}\\ \left(L_{on}+L_{T1}\right)\dfrac{di_{onq}}{dt}=-\omega\left(L_{on}+L_{T1}\right)i_{ond}+\dfrac{v_{ca1q}}{T_{ac1}}-v_{onq}-R_{on}i_{onq}\end{cases} \tag{6.11}$$

where R_{on}, L_{on} and L_{T1} are the resistance, grid inductance and transformer 1 inductance; i_{ond} and i_{onq} are the d- and q-axis components of HVAC connected onshore grid current; v_{ca1d}, v_{ca1q}, v_{ond} and v_{onq} are the d- and q-axis components of HVAC cable capacitor voltage and grid voltage. T_{ac1} is the ration of the onshore transformer 1.

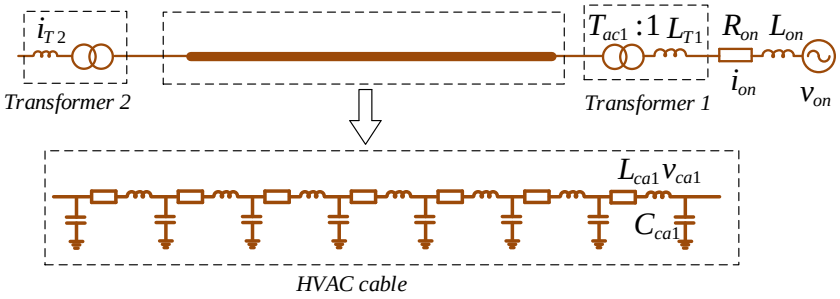

Fig. 6. 4 Diagram of HVAC link.

HVAC cable is represented with 7 R-L-C π sections. The modelling of HVAC cable and transformer 2 can be extended from one AC cable π section. The dynamic of one R-L-C π sections is expressed as

$$\begin{cases} C_{ca1}\dfrac{dv_{ca1d}}{dt} = \omega C_{ca1} v_{ca1q} + \dfrac{i_{ond}}{T_{ac1}} - i_{ca1d} \\ C_{ca1}\dfrac{dv_{ca1q}}{dt} = -\omega C_{ca1} v_{ca1d} + \dfrac{i_{onq}}{T_{ac1}} - i_{ca1q} \end{cases}$$
$$\begin{cases} L_{ca1}\dfrac{di_{ca1d}}{dt} = \omega L_{ca1} i_{ca1q} + v_{ca2d} - v_{ca1d} - R_{ca1} i_{ca1d} \\ L_{ca1}\dfrac{di_{ca1q}}{dt} = -\omega L_{ca1} i_{ca1d} + v_{ca2q} - v_{ca1q} - R_{ca1} i_{ca1q} \end{cases} \quad (6.12)$$

where R_{ca1}, C_{ca1} and L_{ca1} are the resistance, capacitance and inductance of first AC cable π section; i_{ca1d} and i_{ca1q} are the d- and q-axis components of cable inductance current; v_{ca2d} and v_{ca2q} are the d- and q-axis components of second π section cable capacitor voltage.

The dynamics of the DR-HVDC link and HVAC link described above are based on their own rotating dq references, as shown in Fig. 6. 5. In order to analyse the parallel operation when the two links are connected to the PCC, it is necessary to

transform the individual rotating reference to a same reference for stability analysis. In this paper, the rotating reference of the diode rectifier $d_{DR}q_{DR}$ is chosen as the common rotating reference.

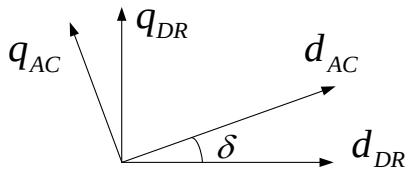

Fig. 6. 5 Diagram of *dq* rotating reference for DR-HVDC link and HVAC link.

Fig. 6. 5 shows the phase angle difference of the *dq* rotating references between the two links. The current of HVAC link transformer 2 i_{T2} in $d_{AC}q_{AC}$ reference frame is transformed to that based on $d_{DR}q_{DR}$ reference i_{T2AC_DR}, which are expressed as

$$\begin{aligned} i_{T2AC\_DRd} &= i_{T2d}\cos\delta - i_{T2q}\sin\delta \\ i_{T2AC\_DRq} &= i_{T2q}\cos\delta + i_{T2d}\sin\delta \end{aligned} \tag{6.13}$$

On the other hand, the offshore PCC voltage v_{pcc} in $d_{DR}q_{DR}$ reference frame is converted to $d_{AC}q_{AC}$ reference v_{pccDR_ACdq} using the reversed transformation, as

$$\begin{aligned} v_{pccDR\_ACd} &= v_{pccd}\cos\delta + v_{pccq}\sin\delta \\ v_{pccDR\_ACq} &= -v_{pccd}\sin\delta + v_{pccq}\cos\delta \end{aligned} \tag{6.14}$$

By linearizing the system at an operating point, the state space model of the parallel system is obtained. Fig. 6. 6 shows the complete small-signal model of WT converters connected with DR-HVDC link and HVAC link.

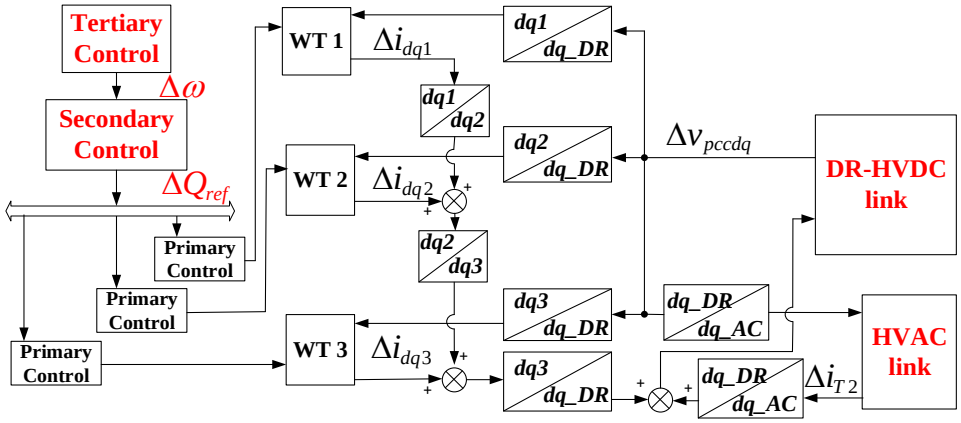

Fig. 6. 6 Complete small-signal model of WT converters connected with DR-HVDC link and HVAC link.

6.4.2 Validation of the small-signal modelling

In order to validate the small-signal model, time domain performances of the small-signal model in MATLAB are compared with the simulation results in PSCAD/EMTDC under different operation modes. The system parameters are shown in Table 6. 1.

Table 6. 1 Parameters of the tested parallel operation system

Components	Parameters	Values
DR-HVDC link	Power	800 MW
	DC voltage	±320 kV
	DR transformer (Y/Y/Δ) Leakage inductance	66/260/260 kV, 0.18 pu
	Reactive power compensation	0.2 pu
HVAC link	Power	400 MW
	HVAC cable length	7×5 km
WTC	Rating of aggregate WTC	400 MW×3

	Transformer (Y/Δ) Leakage inductance	0.69/66 kV 0.08 pu
	WT Filter capacitor C_f	0.1pu
	Converter reactance L_w	0.1 pu
	AC cable length (for each aggregate WT converter)	5 km, 10 km, 15 km

Fig. 6. 7 (a) and (b) compare the responses under DR-HVDC mode when secondary voltage control order increases by 0.05 kV at 3.2 s and phase angle control order increases by 0.05 rad at 0.2s (operating point: WT 1, 2 and 3 generate 100, 200 and 400 MW respectively). Under the same WT operating condition, Fig. 6. 7 (c) and (d) show the comparison of the responses under parallel mode when the AC active power control order changes from 0 to 1 MW at 0.2 s and DC active power control order changes from 0 to -1 MW at 0.2 s. Fig. 6. 7 (e) shows the comparison of the responses under HVAC mode when the virtual DC active power control order changes from 0 to 1 MW at 0.2 s (operating point: WT 1, 2 and 3 generate 200, 50 and 50 MW respectively). As can be seen, the performances of the small-signal model are in good agreements with the results of PSCAD/EMTDC simulation.

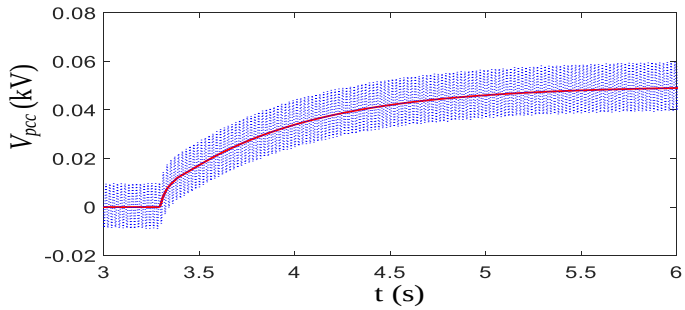

(a) Offshore PCC voltage change on DR-HVDC mode

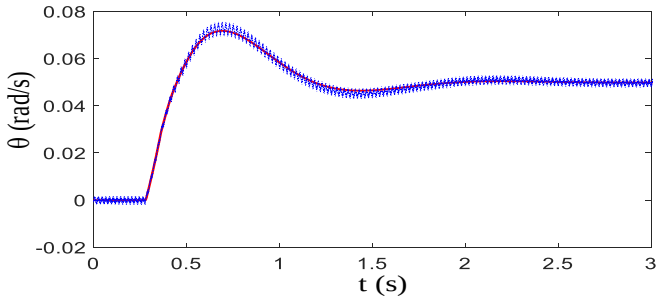

(b) Angle order change on DR-HVDC mode

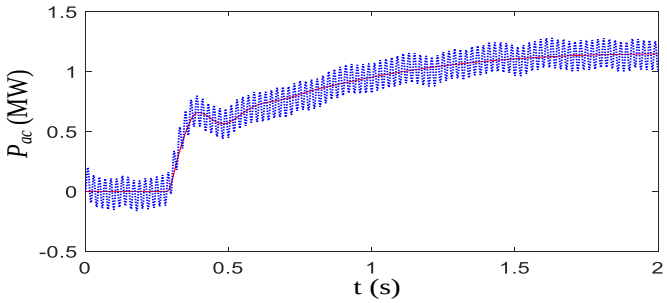

(c) AC power order change on parallel mode

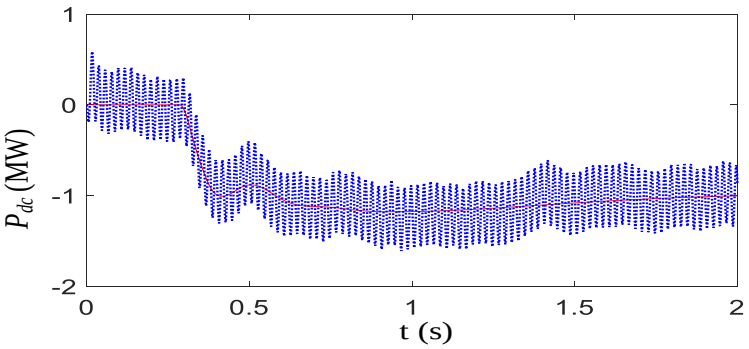

(d) DC power order change on parallel mode

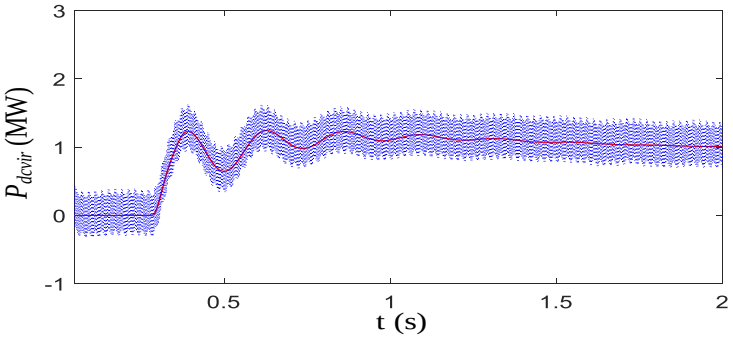

(e) Virtual DC power order change on HVAC mode

Fig. 6. 7 Comparison between small-signal model (red curve) and PSCAD model (blue curve) on different operation modes.

6.4.3 Stability analysis of the secondary and tertiary controls

A. Stability analysis of the secondary control

This sub-section describes the stability analysis of the secondary voltage control, secondary frequency control and phase angle control.

The eigenvalues are derived when the secondary voltage control is enabled. Fig. 6. 8 (a) and (b) shows the trace of the most affected eigenvalues when communication delay T_v increased from 0 s to 1.18 s. As seen, $\lambda_{1,2}$ (-84.9 ± 3.6i) in Fig. 6. 8 (a) are shifted towards the right plane and eventually become evanescent modes, whereas $\lambda_{3,4}$ (-1.27, -4) in Fig. 6. 8 (b) become conjugated roots. When T_v increases to 1.18 s, the real parts of $\lambda_{3,4}$ become positive, resulting in potential system instability. Considering both system stability and practical implementation, communication delay T_v is chosen as 0.08s in further studies.

Fig. 6. 8 (c) shows the root-loci of the closed-loop system by varying the secondary voltage control parameter k_{svp} from 0 to 16 (k_{svp} / k_{svi} keeps constant at 0.1). $\lambda_{3,4}$ move towards the left side, whereas $\lambda_{1,2}$ become less damped and eventually move to the right plane at k_{svp} = 16. In further studies, k_{svp} = 2 is chosen to achieve a balance of stability and response time.

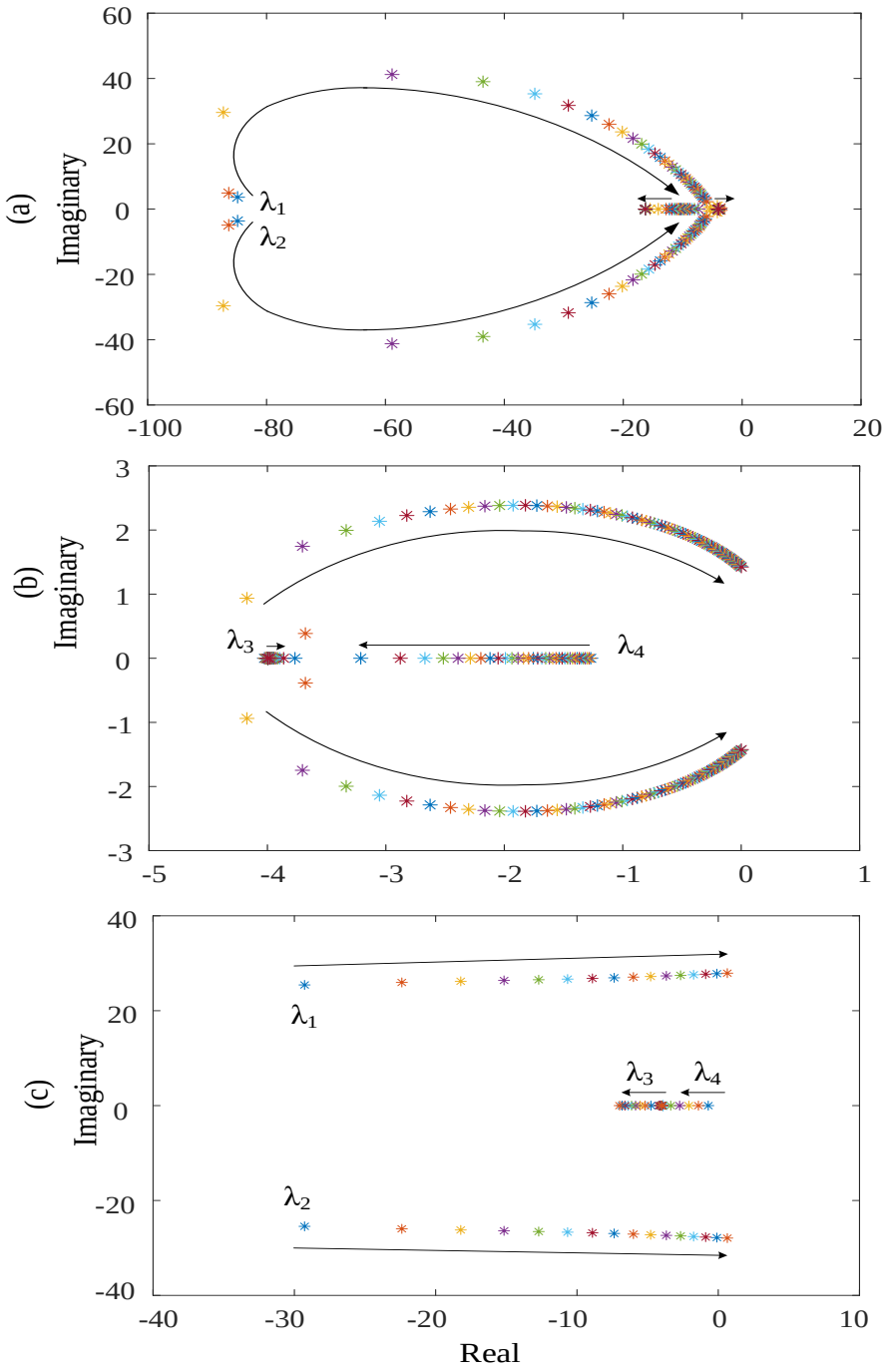

Fig. 6. 8 Traces of eigenvalues when T_v and k_{svp} change: (a) Traces of eigenvalues $\lambda_{1,2}$ when T_v from 0 s to 1.18s by 0.01s, (b) traces of eigenvalues $\lambda_{3,4}$ when T_v from 0 s to 1.18s by 0.01s, (c) traces of eigenvalues $\lambda_{1,2}$ and $\lambda_{3,4}$ when k_{svp} from 0 to 16 by 1.

Similar studies are conducted for the secondary frequency control and phase angle control, as shown in Fig. 6. 9 (a) and (b). As a result, k_{wp} and k_{syp} are chosen as 3 and 20 respectively to achieve satisfactory responses.

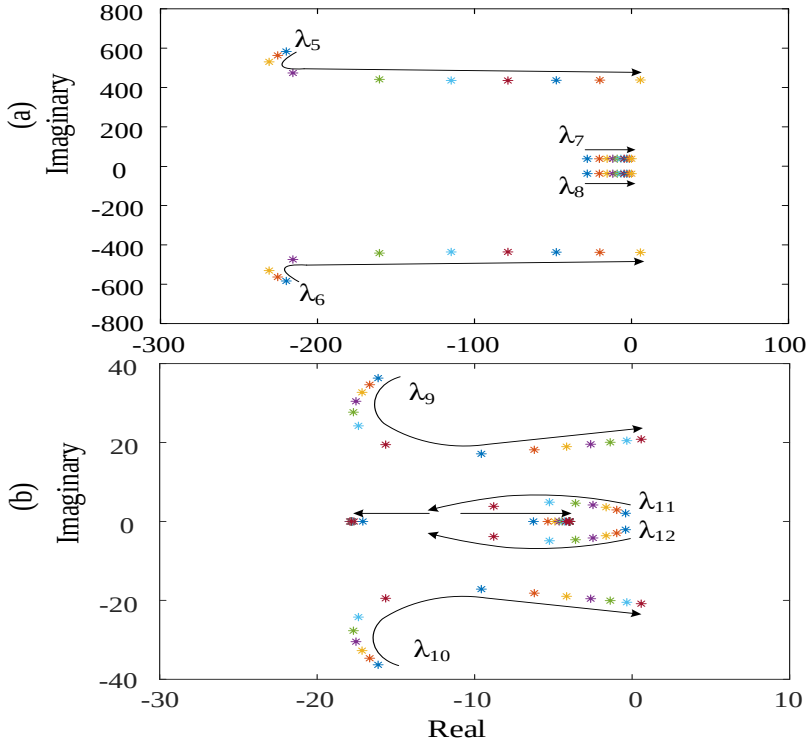

Fig. 6. 9 Traces of eigenvalues when k_{wp} and k_{syp} change: (a) k_{wp} from 0 to 10 by 1, (b) k_{syp} from 0 to 70 by 5.

B. Stability analysis of tertiary power flow control

The stability analysis of the AC active power control and DC active power control is discussed in this sub-section.

Fig. 6. 10 (a) shows the movements of the most affected eigenvalues when AC power control parameter k_{acp} increased from 0 to 0.13. As seen, $\lambda_{15,16}$ are shifted towards to more stable region while $\lambda_{13,14}$ become less damped. When $k_{acp} > 0.13$, the real parts of $\lambda_{13,14}$ turn to positive, resulting in potential system instability. Fig. 6. 10 (b) shows the trace of the eigenvalues when DC power control parameter k_{dcp} varies. The system can remain stable until k_{dcp} is larger than 0.1. Based in the analysis, k_{acp} and k_{dcp} are both chosen as 0.05 to achieve adequate damping and dynamic.

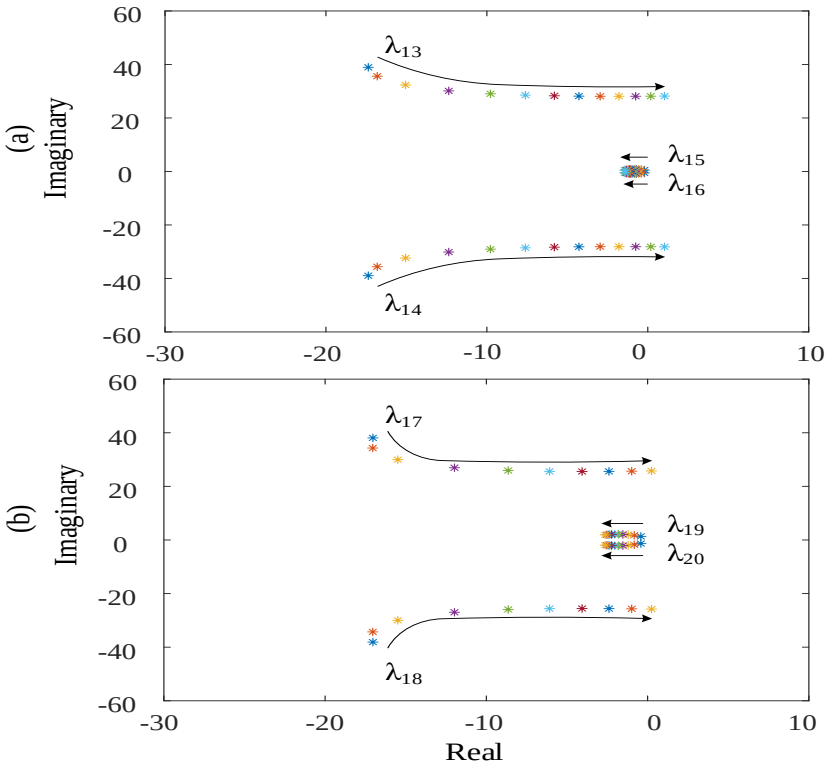

Fig. 6. 10 Traces of eigenvalues when k_{acp} and k_{dcp} change: (a) k_{acp} from 0 to 0.13 by 0.01, (b) k_{dcp} from 0 to 0.1 by 0.01.

6.5 Simulation results

In order to verify the operation of offshore wind farms under different operation modes, the systems shown in Fig. 6. 1 with the parameters in Table 6. 1, are established in PSCAD/EMTDC. The wind farms are modelled as three aggregate 400 MW WT LSCs.

6.5.1 Transition from DR-HVDC mode to parallel mode

The performance during the transition from DR-HVDC mode to parallel mode is illustrated in Fig. 6. 11.

At the beginning, the generated active power of WT1, 2 and 3 is 100 MW, 150 MW and 400 MW respectively under the DR-HVDC mode, as shown in Fig. 6. 11 (a). The reactive power is well shared among the WTs at 6 MVAr each (positive Q_{wt} defined as WTs providing capacitive reactive power to the offshore AC network), as

shown in Fig. 6. 11 (b). The offshore PCC AC voltage is 0.983 pu and frequency is 50.05 Hz, whereas the unconnected HVAC link voltage and frequency are 0.965 pu and 50Hz, respectively, as shown in Fig. 6. 11 (c) and (e).

At 5 s, the proposed secondary voltage control is enabled. The onshore MMC DC voltage V_{dci} is regulated from 1 pu to 0.978 pu and the offshore PCC voltage V_{pcc} is decreased from 0.983 pu to 0.965 pu, to match the HVAC link voltage V_{T2}, as shown in Fig. 6. 11 (d) and (c).

At 10 s, the proposed secondary frequency control is initialized. The offshore frequency is decreased from 50.2 Hz to 50 Hz, to match the HVAC link frequency, as shown in Fig. 6. 11 (e). Consequently, the phase angle difference ($\theta_{pcc}-\theta_{T2}$) between the offshore PCC voltage and HVAC link voltage keeps stable at 1.51 rad., as shown in Fig. 6. 11 (f).

At 20 s, the phase angle control is enabled. The phase angle difference ($\theta_{pcc}-\theta_{T2}$) between offshore PCC voltage and HVAC link starts to decrease from 1.51 rad. to 0 rad., as shown in Fig. 6. 11 (f). For illustration, Fig. 6. 11 (h) and (i) show the instantaneous offshore PCC voltage v_{pcc} and HVAC link voltage v_{T2} before and after phase synchronization. As seen, after the phase synchronization, the two waveforms become closely matched.

At 30 s, the AC breaker of the HVAC link B_{AC} (shown in Fig. 6. 1) is closed to connect the HVAC link with the offshore wind farms. No inrush current is observed and smooth transition from DR-HVDC mode to parallel mode is achieved, as shown in Fig. 6. 11 (i). Meanwhile, the proposed tertiary power flow control is enabled to regulate the HVAC link active power at 0. As a result, all the wind power is still transmitted through DR-HVDC link, as illustrated in Fig. 6. 11 (g).

At 32 s, the secondary offshore PCC voltage control is disabled to restore the onshore MMC DC voltage to 1 pu, as seen in Fig. 6. 11 (d). The PCC voltage also increases, resulting the increase of HVAC link reactive power Q_{ac} from 0 MVAr to 31 MVAr and so as the reactive power provided by the 3 aggregated WTs seen in Fig. 6. 11 (b).

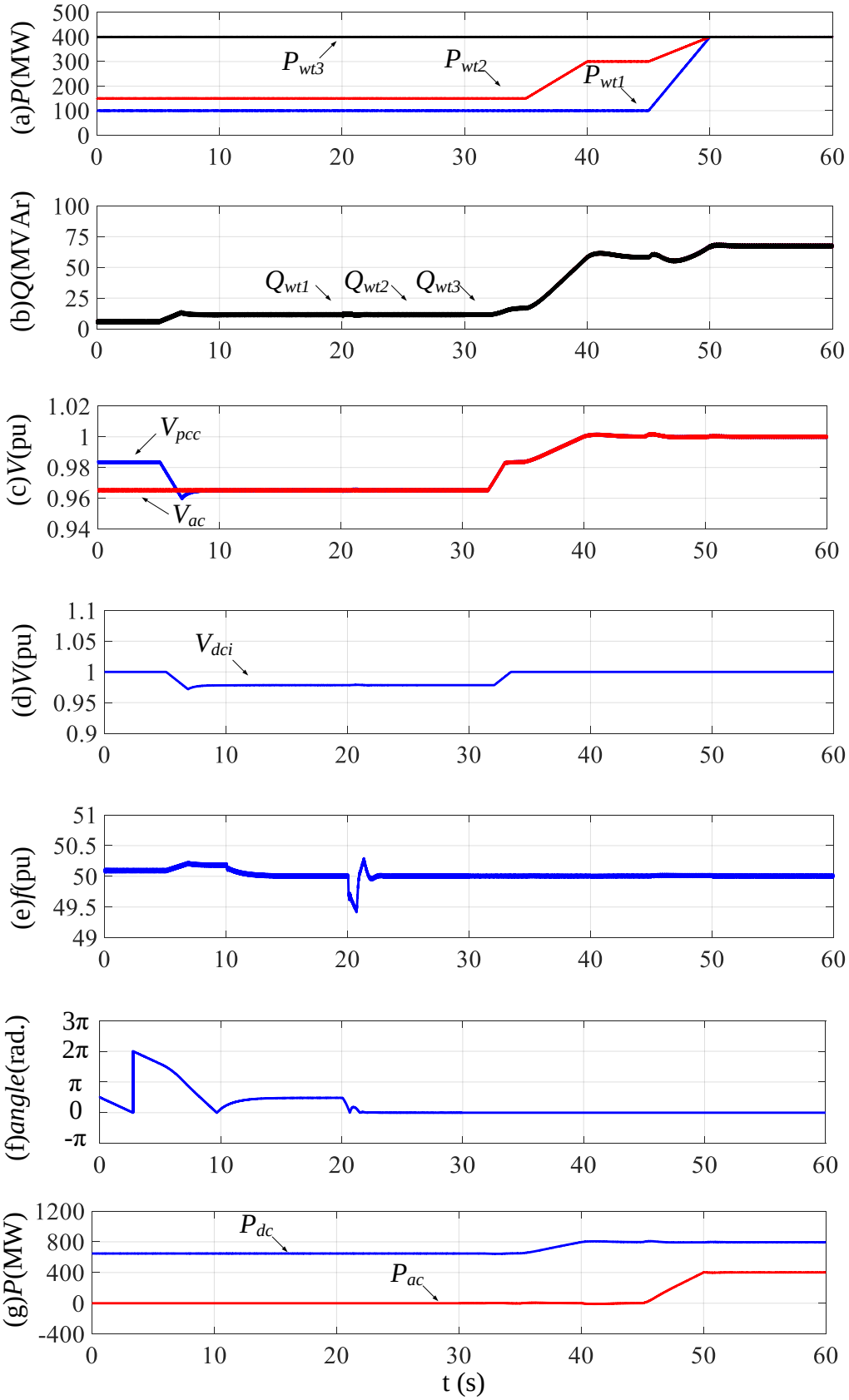
(a)P(MW)
500
400
300
200
100
0
P_{wt3}
P_{wt2}
P_{wt1}
0
10
20
30
40
50
60
(b)Q(MVAr)
100
75
50
25
0
Q_{wt1}
Q_{wt2}
Q_{wt3}
(c)V(pu)
1.02
1
0.98
0.96
0.94
V_{pcc}
V_{ac}
(d)V(pu)
1.1
1.05
1
0.95
0.9
V_{dci}
(e)f(pu)
51
50.5
50
49.5
49
(f)angle(rad.)
3π
2π
π
0
-π
(g)P(MW)
1200
800
400
0
-400
P_{dc}
P_{ac}
t (s)

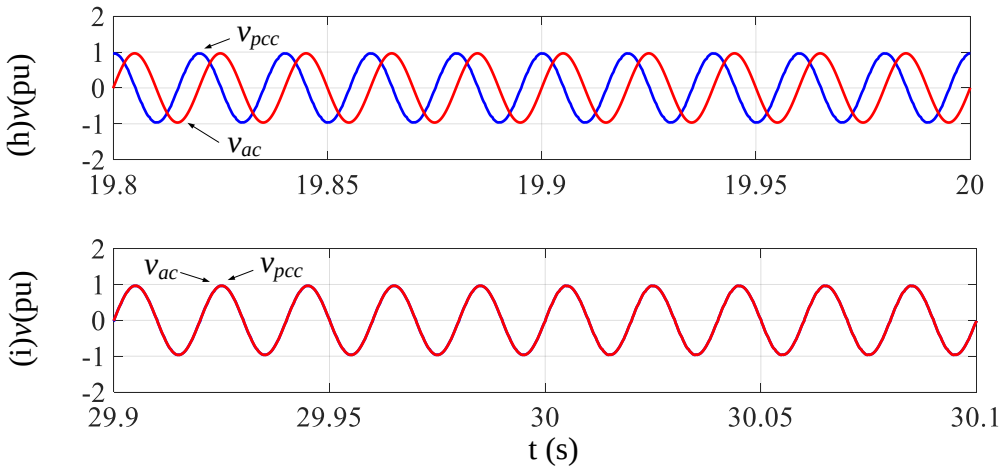

Fig. 6. 11 Simulation results from DR-HVDC mode to parallel mode: (a) WTs active power, (b) WTs reactive power, (c) voltage of offshore PCC and HVAC link, (d) onshore MMC DC voltage, (e) offshore PCC frequency, (f) phase angle difference between offshore PCC voltage and HVAC link, (g) transmitted active power of DR-HVDC link and HVAC link, (h) instantaneous voltage of offshore PCC and HVAC link before synchronization control enabled, (i) instantaneous voltage of offshore PCC and HVAC link after synchronization control enabled.

WT 2 ramps its active power from 150 MW to 300 MW from 35 s to 40 s as shown in Fig. 6. 11 (a). With the DR-HVDC transmitted active power reaching its rated value at 800 MW, the proposed tertiary control is automatically switched from AC active power control to DC active power control to avoid the overload of DR-HVDC link.

From 45 s to 50 s, both WT2 and 3 increase their generated wind power to rated value at 400 MW, as shown in Fig. 6. 11 (a). Fig. 6. 11 (g) shows the DR-HVDC link transmitted active power is controlled at 800 MW by the tertiary DC active power control while additional 400 MW active power is transmitted through the HVAC link.

6.5.2 Transition from HVAC mode to parallel mode

The performance of the systems during the transition from HVAC mode to parallel mode is illustrated in Fig. 6. 12.

Initially, each of WT1, 2 and 3 generates 50 MW on HVAC mode while reactive power of each WT converter is controlled at 0, as shown in Fig. 6. 12 (a) and (b). From

3 s to 4 s, WT1 ramps its power from 50 MW to 200 MW, while WT2 and 3 active power remains at 50 MW. Consequently, HVAC transmitted active power is increased from 150 MW to 300 MW as shown in Fig. 6. 12 (e). These results indicate the primary control, presented in chapter 3, can well operate under HVAC mode.

At 5 s, the proposed virtual DC power control is enabled with P_{dccref} at 0. Fig. 6. 12 (c) and (d) show the offshore PCC voltage decreases from 1.046 pu to 0.89 pu and the virtual DC power is decreased from 280 MW to 0 MW, respectively. Meanwhile WTs start to absorb 66 MVar reactive power, as shown in Fig. 6. 12 (b).

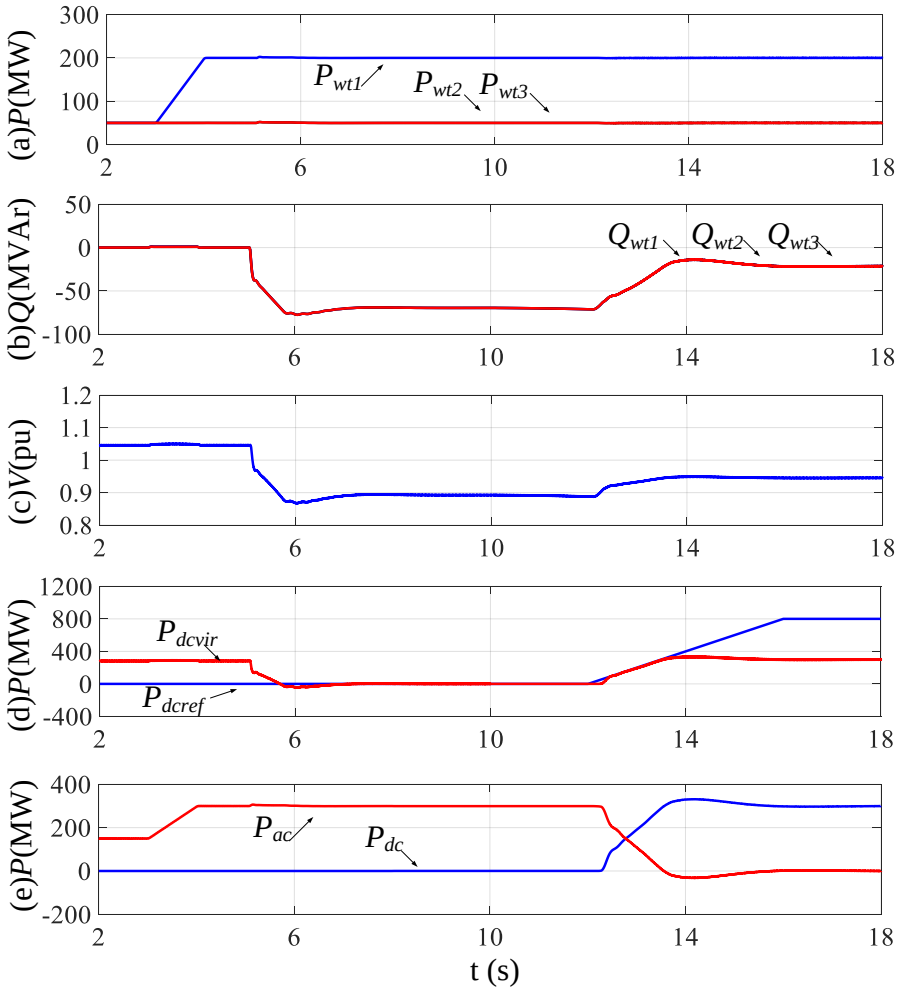

Fig. 6. 12 Simulation results from HVAC mode to parallel mode: (a) WTs active power, (b) WTs reactive power, (c) offshore PCC voltage, (d) virtual power and its reference of DR-HVDC link, (e) active power of DR-HVDC link and HVAC link.

At 8 s, DR-HVDC link is connected to the offshore wind farms. As shown in Fig. 6. 12 (e), the DR-HVDC link transmitted active power before and after the mode switch keeps at 0, indicating the smooth transition from HVAC mode to parallel mode. At 10 s, the virtual DC power control is changed to real DC power control. From 12 s - 16 s, DC power reference is increased from 0 MW to 800 MW, as shown in Fig. 6. 12 (d). With this reference increase, the DC power control saturates meanwhile AC power control starts to de-saturate. As seen in Fig. 6. 12 (e), HVAC link transmitted power is thus decreased to 0 due to the function of AC active power control while all wind power is transmitted to onshore grid through DR-HVDC link.

6.5.3 Transition from parallel mode to DR-HVDC mode

The performance of the systems, during the transition from parallel mode to DR-HVDC mode due to HVAC permanent faults, is illustrated in Fig. 6. 13. Initially, WT 1, 2 and 3 generate 100, 200, 300 MW respectively on parallel mode while reactive power of each WT converter is controlled at 0, as shown in Fig. 6. 13 (d) and (e).

At 5 s, a solid three-phase fault occurs at the middle of HVAC link. As shown in Fig. 6. 13 (a) and (b), voltages at the fault location v_{acf} and offshore PCC v_{pcc} rapidly decrease to 0 and 0.3 pu respectively after the fault. The reduction of the offshore AC voltage leads to the decrease of WT active powers to around 0, as shown in Fig. 6. 13 (d). Due to reduced offshore PCC voltage, diode-rectifier is automatically reverse-biased and no power can be transmitted through DR-HVDC link, as shown in Fig. 6. 13 (f). Meanwhile, each WT converter operates under current limiting mode, controlling the fault current at the allowable maximum value as seen in Fig. 6. 13 (c). Fig. 6. 13 (e) shows that each WT converter reactive power output increases from 1 MVar to 210 MVar to achieve the offshore network reactive power re-balance.

At 5.15 s, the AC breaker B_{AC} (shown in Fig. 6. 1) is opened to isolate the HVAC link fault. As seen from the Fig. 6. 13 (d) and (f), the wind power generation and DR-HVDC link transmission are quickly restored. In the case that after the disconnection of HVAC link, the WT generated wind power is higher than the DR-HVDC rated power, some WTs need to be curtailed as part of wind farm emergency control to avoid overloading of the DR-HVDC link but is not further investigated here.

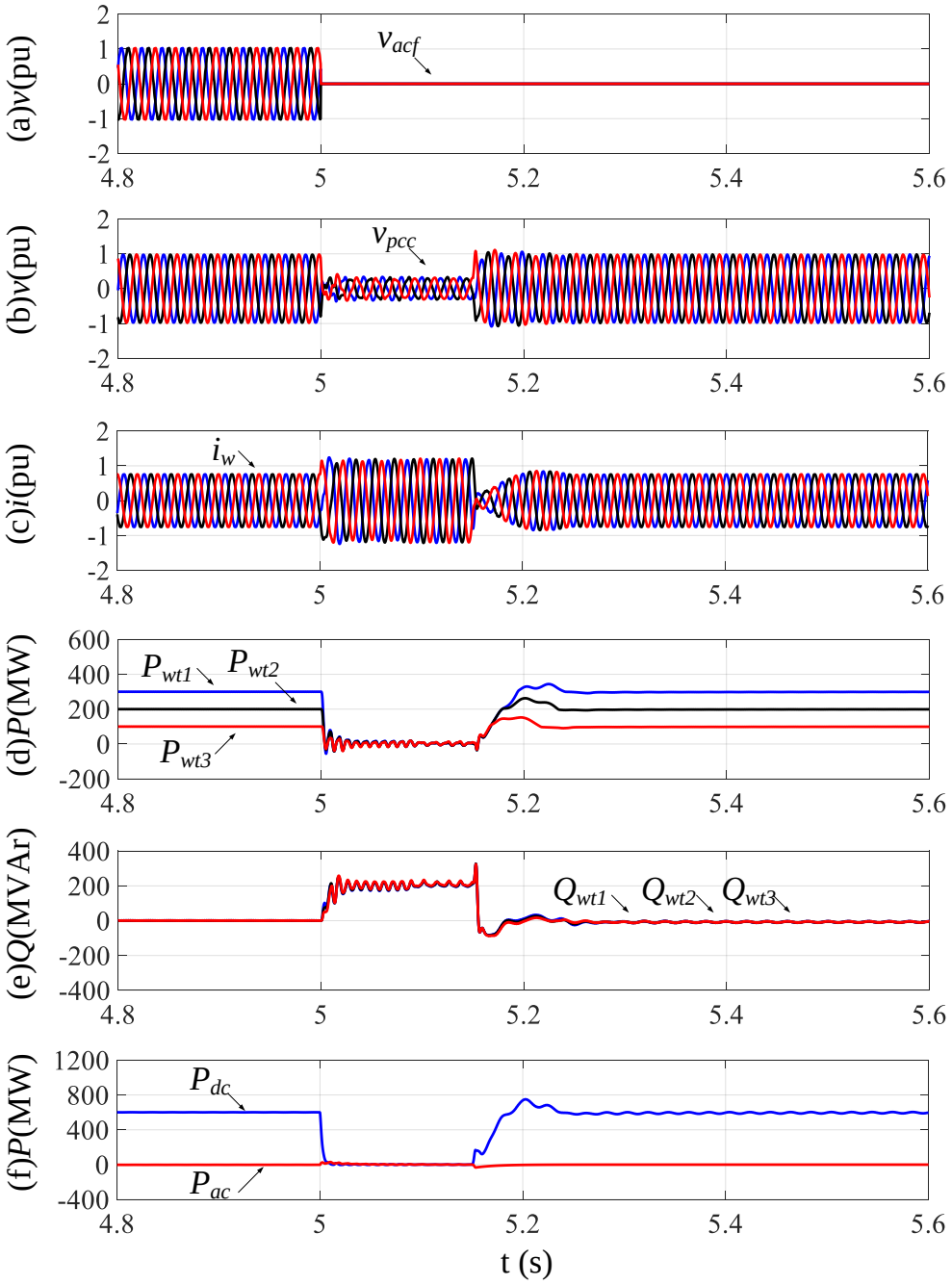

Fig. 6. 13 Simulation results from parallel mode to DR-HVDC mode due to an HVAC link fault: (a) HVAC link AC voltage, (b) offshore PCC voltage, (c) WT current, (d) WTs active power, (e) WTs reactive power, (f) active power of DR-HVDC link and HVAC link.

6.5.4 Transition from parallel mode to AC mode

The performance of the systems during the transition from parallel mode to HVAC mode due to DC permanent faults is illustrated in Fig. 6. 14. Initially, WT1, 2 and 3 generate 50, 100, 150 MW respectively on parallel mode while reactive power of each WT converter is controlled at -20 MVAr, as shown in Fig. 6. 14 (d) and (e).

At 10 s, a solid DC fault occurs at the DR-HVDC link. Fig. 6. 14 (a) and (b) show the DR-HVDC link DC voltage rapidly decreases to 0 pu after the fault and offshore PCC voltage drops to around 0.05 pu. During the fault, the WT fault current is well controlled as shown in Fig. 6. 14 (c). Meanwhile, each WT converter increases its reactive power output from -20 MVar to around 30 MVar to achieve the offshore network reactive power re-balance, as seen in Fig. 6. 14 (e). Both the transmitted DR-HVDC power and HVAC power reduce to 0 MW, as shown in Fig. 6. 14 (f).

At 10.15 s, the AC breaker B_{DR} (shown in Fig. 6. 1) opens to isolate the DR-HVDC fault from the offshore network. As seen from the Fig. 6. 14 (d) and (f), the wind power is restored and transmitted through HVAC link. In the case that after the disconnection of DR-HVDC link, the WT generated wind power is higher than the HVAC rated power, some WTs need to be curtailed as part of wind farm emergency control to avoid overloading of the HVAC link but is not further investigated here.

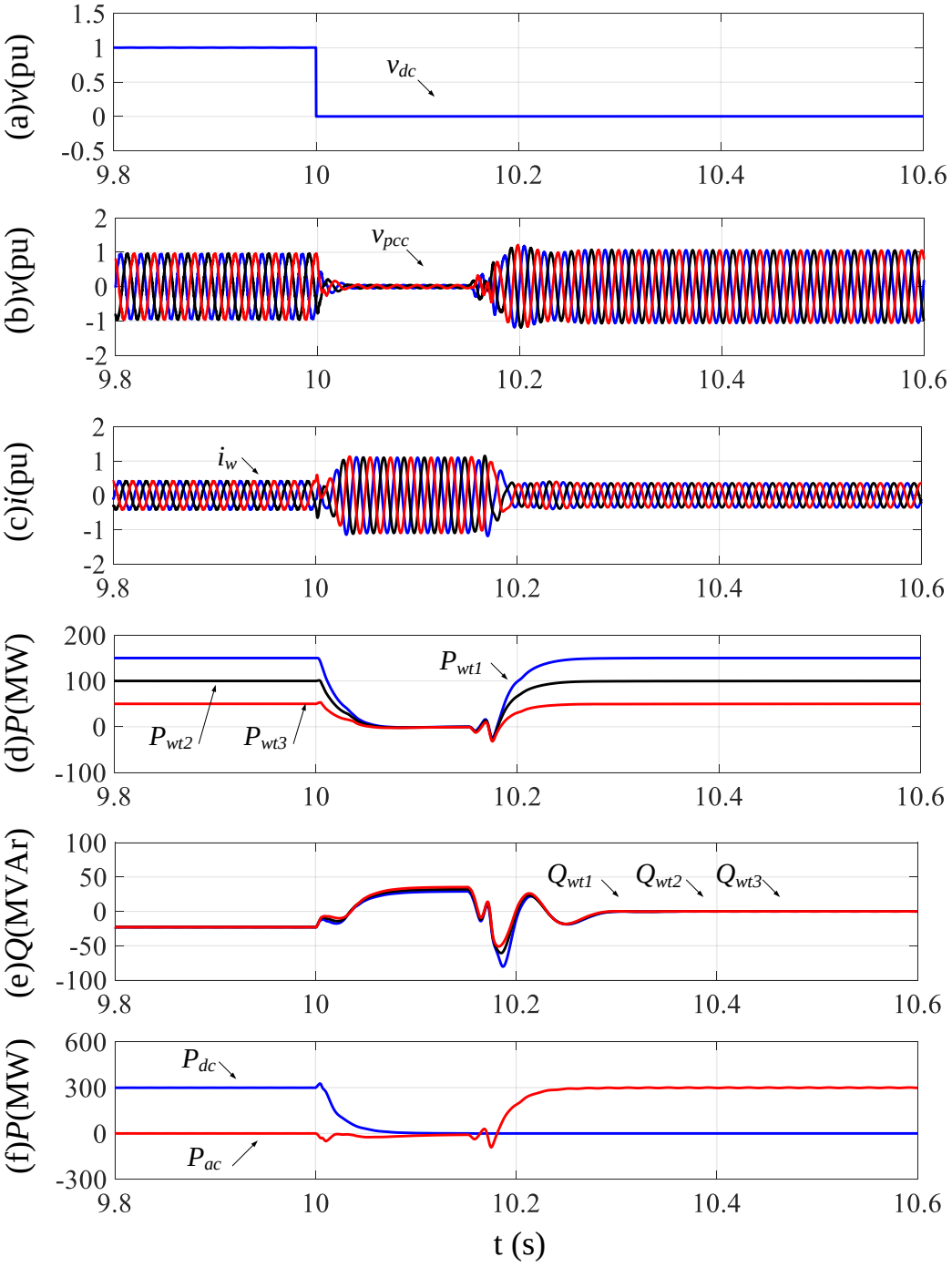

Fig. 6. 14 Simulation results from parallel operation to HVAC operation mode due to a DR-HVDC link DC fault: (a) DC voltage, (b) offshore PCC voltage, (c) WT current, (d) WTs active power, (e) WTs reactive power, (f) active power of DR-HVDC link and HVAC link.

6.6 Summary

The parallel operation of DR-HVDC and HVAC links connected with offshore wind farms is investigated in this chapter. The parallel connection offers the advantages of improved efficiency, reliability and availability, as presented in the 'Kriegers flak-combined grid solution' project. A hierarchical control structure of WT LSC, including primary control, secondary voltage control, secondary frequency control, phase angle control and tertiary active power flow control, is proposed to achieve smooth transition between different operation modes. The proposed secondary voltage control, frequency control and phase angle control regulate the offshore PCC voltage magnitude, frequency and phase angle to match those of the HVAC link, allowing seamless transition from DR-HVDC mode to parallel mode. The tertiary control regulates the power flow between DR-HVDC link and HVAC link through the modification of PCC phase angle, ensuring the required power sharing on parallel mode. The proposed virtual DC power control regulates the virtual DC power at zero by adjusting the offshore PCC voltage magnitude, allowing seamless switch from HVAC mode to parallel mode. Small-signal stability analysis is carried out to design the secondary, tertiary control parameters and investigate the effect of centralized controller communication delay on system performance. Simulation results verify the proposed control strategy during the transition among various operation modes.

Chapter 7 Conclusion and future work

7.1 General conclusions

The thesis focuses on the control and operation of offshore wind farms connected with DR-HVDC systems, where a diode rectifier is used offshore and an MMC is used onshore.

Due to the use of offshore diode rectifier, the WT LSCs need to control the offshore AC voltage and frequency, in addition to regulating the active and reactive power outputs of WTs. A distributed control of WT LSCs is thus proposed for offshore wind farms connected with DR-HVDC system. The proposed control system includes current control, voltage control, PLL-based frequency control, WT active power control using *P-V* loop and reactive power control using *Q-f* loop. The proposed control enables each WT converter to operate as a grid-forming source and contribute to the overall offshore voltage and frequency regulation, which provides WTs with plug-and-play capability for offline WTs to synchronize the offshore network.

A small-signal state-space model of WTs connected with DR-HVDC systems using the proposed control system has been developed. With this small-signal model, the wind farm level analysis is implemented to study the interactions among active and reactive powers, offshore AC voltage and frequency. It is revealed that AC voltage magnitude has a bigger effect on both active and reactive power than offshore frequency in DR-HVDC connected wind farms. WT level analysis has also been carried out, which demonstrates the mechanism of individual WT power transmission to offshore AC network, with the adopted *P-V* and *Q-f* control scheme. The analysis shows that the change of individual WT active power transmission is mainly dependent on the variation of phase angle difference, although the DR-HVDC transmitted active power depends on the variation of offshore PCC AC voltage magnitude. An angle compensation control is further proposed to alleviate the coupling between WT active power and reactive power caused by the use of *P-V* and *Q-f* control in this scheme. Stability analysis has been carried out to derive the stability range of the angle compensation control, active power control and reactive power control parameters.

The performances of WTs connected with DR-HVDC during onshore AC faults, offshore AC faults and DC faults have been investigated. To ride-through onshore AC faults, the active onshore MMC DC voltage control method combined with the WT overvoltage limiting control is proposed. By inserting additional submodules of the onshore MMC to temporarily increase the DC link voltage, the WTs are forced to operate on offshore AC overvoltage limiting control mode more quickly and active power re-balance between the offshore and onshore sides can be achieved faster, alleviating the MMC submodule capacitor overvoltage. The fault current limiting method is proposed to ensure the safe operation of WTs during offshore AC faults. The reactive current is prioritized over active current in order to ensure the offshore frequency remains controlled. A simple and effective offshore AC fault overcurrent protection solution is proposed for fault detection and isolation. In addition, the system response after permanent DC pole-to-pole faults has been analysed. It demonstrates that, the DC fault is propagated to the offshore AC network due to the use of diode rectifier, resulting in the decrease of the offshore AC voltage. The offshore WT converters then operate on fault current limiting control modes to ensure their safe operation.

Due to the potential advantages of parallel DR-HVDC and HVAC links connected offshore wind farms, e.g. improved efficiency, reliability and availability etc., different operation modes including parallel mode, HVAC mode and DR-HVDC mode have been investigated. A hierarchical control structure with primary control, secondary voltage control, secondary frequency control, phase angle control and tertiary active power flow control, is proposed in order to achieve smooth operation mode switch. Specifically, to ensure transition from DR-HVDC mode to parallel mode, the secondary voltage control is proposed to match the offshore AC voltage amplitude with that of the HVAC link, by regulating the DC voltage of the DR-HVDC link. The secondary frequency control and phase angle control are proposed to enable the offshore PCC frequency and phase angle to synchronize with those of the HVAC link. The tertiary control scheme is proposed to control the active power flow distribution between DR-HVDC and HVAC links through the regulation of PCC phase angle on parallel mode. For smooth transition from HVAC mode to parallel mode, the virtual

DC power control is proposed to regulate the virtual DC power at zero, prior to the connection of the DR-HVDC link by adjusting the offshore PCC voltage magnitude.

Extensive time-domain simulation in PSCAD/EMTDC software and frequency-domain simulation in Matlab/Simulink environment have demonstrated the feasibility of the DR-HVDC systems and the proposed control methods.

7.2 Author's contributions

The main contributions of this thesis are:

- A distributed PLL based control is proposed for offshore WT converters connected through DR-HVDC systems. With the proposed control, each WT operates autonomously and contributes to the overall offshore AC voltage and frequency control.
- A small-signal state-space model of the WTs and connected DR-HVDC system is presented. The interactions between active / reactive powers, and offshore AC voltage / frequency is investigated based on the wind farm level analysis. With the adopted *P-V* and *Q-f* control scheme, the mechanism of individual WT power transmission to offshore AC network is revealed based on the WT level analysis. An angle compensation control is proposed to alleviate the coupling between WT active power and reactive power when using the *P-V* and *Q-f* control.
- An active onshore MMC DC voltage control combined with WT overvoltage limiting control is proposed to alleviate the MMC submodule capacitor overvoltage during onshore AC faults. A fault current limiting method is proposed to ensure the safe operation of WTs during offshore faults to avoid converter overcurrent and an effective offshore AC fault overcurrent protection solution is further proposed to detect and isolate the offshore AC faults.
- Parallel operation of DR-HVDC and HVAC links connected with offshore wind farms is investigated. A hierarchical control, which includes the primary control, secondary control and tertiary control, is proposed to achieve seamless transitions between various operation modes.

7.3 Suggestions for future research

Potential areas for future research include:

- System stability analysis and fault performances considering the dynamics of WT generators and generator side converters need to be conducted.
- Integration of DR-HVDC to multi-terminal HVDC systems needs to be further investigated, including the control design, stability analysis, DC fault detection and isolation solutions.
- WT level analysis can be further carried out to improve the WT active power transient performances during WT reactive power change.
- Impedance based stability analysis can be conducted to reveal the interactions between the WTs and the DR-HVDC systems.
- Hardware-in-the-loop simulation platform can be created to further demonstrate the effectiveness of the proposed control methods under various operating conditions.

Reference

[1] EuropeanCommission, "The Revised Renewable Energy Directive," *https://ec.europa.eu/energy/sites/ener/files/documents/directive_renewable_factsheet.pdf,* 2018.

[2] E. (EEA), "Share of renewable energy in gross final energy consumption," *https://www.eea.europa.eu/data-and-maps/indicators/renewable-gross-final-energy-consumption-4/assessment-3,* 2018.

[3] WindEurope, "Wind in power 2017: Annual combined onshore and offshore wind energy statistics," *https://windeurope.org/wp-content/uploads/files/about-wind/statistics/WindEurope-Annual-Statistics-2017.pdf,* 2018.

[4] WindEurope, "Wind Energy in Europe: Outlook to 2022," *https://windeurope.org/about-wind/reports/wind-energy-in-europe-outlook-to-2022,* 2018.

[5] WindEurope, "The European Offshore Wind Industry – Key Trends and Statistics 2017," *https://windeurope.org/wp-content/uploads/files/about-wind/statistics/WindEurope-Annual-Offshore-Statistics-2017.pdf,* 2018.

[6] P. Bresesti, W. L. Kling, R. L. Hendriks, and R. Vailati, "HVDC Connection of Offshore Wind Farms to the Transmission System," *IEEE Transactions on Energy Conversion,* vol. 22, pp. 37-43, 2007.

[7] O. Anaya-Lara, D. Campos-Gaona, E. Moreno-Goytia, and G. Adam, *Offshore wind energy generation: control, protection, and integration to electrical systems*: John Wiley & Sons, 2014.

[8] O. Anaya-Lara, J. O. Tande, K. Uhlen, and K. Merz, *Offshore Wind Energy Technology*: John Wiley & Sons, 2018.

[9] C. Buchhagen, C. Rauscher, A. Menze, and J. Jung, "BorWin1 - First Experiences with harmonic interactions in converter dominated grids," in *International ETG Congress 2015; Die Energiewende - Blueprints for the new energy age*, 2015, pp. 1-7.

[10] V. Hussennether, J. Rittiger, A. Barth, D. Worthington, G. Dell'Anna, M. Rapetti, *et al.*, "Projects BorWin2 and HelWin1–large scale multilevel voltage-sourced converter technology for bundling of offshore windpower," *CIGRE Technical Program Session B4-306. Paris, France: CIGRE,* pp. 1-11, 2012.

[11] L. Xu and B. R. Andersen, "Grid connection of large offshore wind farms using HVDC," *Wind Energy,* vol. 9, pp. 371-382, 2006.

[12] N. M. Kirby, X. Lie, M. Luckett, and W. Siepmann, "HVDC transmission for large offshore wind farms," *Power Engineering Journal,* vol. 16, pp. 135-141, 2002.

[13] R. Blasco-Gimenez, S. A.-. Villalba, J. Rodríguez-D´Derlée, F. Morant, and S. Bernal, "Distributed voltage and frequency control of off-shore wind farms connected with a

diode based HVDC link," in *IECON 2010 - 36th Annual Conference on IEEE Industrial Electronics Society*, 2010, pp. 2994-2999.

[14] P. Menke, "New grid access solutions for offshore wind farms," *EWEA Off-shore*, 2015.

[15] T. Hammer, S. Seman, P. Menke, F. Hacker, B. Szangolies, J. Meth, *et al.*, "Diode-rectifier HVDC link to onshore power systems: Dynamic performance of wind turbine generators and reliability of liquid immersed HVDC diode rectifier units," in *CIGRE Conference Technical Committee B4*, 2016.

[16] O. Kuhn, P. Menke, R. Zurowski, T. Christ, S. Seman, and G. Giering, "2nd generation DC grid access for offshore wind farms: HVDC in an AC fashion," *CIGRE, Paris*, pp. 1-7, 2016.

[17] Siemens, "New DC grid access solution," *http://m.energy.siemens.com/hq/pool/hq/power-transmission/grid-access-solutions/dc-solutions/DC-Flyer.pdf*, pp. 1-7, 2015.

[18] A. D. Hansen, F. Iov, F. Blaabjerg, and L. H. Hansen, "Review of contemporary wind turbine concepts and their market penetration," *Wind Engineering*, vol. 28, pp. 247-263, 2004.

[19] H. Li and Z. Chen, "Overview of different wind generator systems and their comparisons," *IET Renewable Power Generation*, vol. 2, pp. 123-138, 2008.

[20] L. Xu, L. Yao, and C. Sasse, "Grid Integration of Large DFIG-Based Wind Farms Using VSC Transmission," *IEEE Transactions on Power Systems*, vol. 22, pp. 976-984, 2007.

[21] S. I. Nanou and S. A. Papathanassiou, "Grid Code Compatibility of VSC-HVDC Connected Offshore Wind Turbines Employing Power Synchronization Control," *IEEE Transactions on Power Systems*, vol. 31, pp. 5042-5050, 2016.

[22] R. Zeng, "Design, analysis and operation of hybrid modular multilevel converters for HVDC applications," University of Strathclyde, 2015.

[23] A. Lesnicar and R. Marquardt, "An innovative modular multilevel converter topology suitable for a wide power range," in *2003 IEEE Bologna Power Tech Conference Proceedings*, 2003, p. 6 pp. Vol.3.

[24] S. Allebrod, R. Hamerski, and R. Marquardt, "New transformerless, scalable Modular Multilevel Converters for HVDC-transmission," in *2008 IEEE Power Electronics Specialists Conference*, 2008, pp. 174-179.

[25] R. Marquardt, "Modular Multilevel Converter topologies with DC-Short circuit current limitation," in *8th International Conference on Power Electronics - ECCE Asia*, 2011, pp. 1425-1431.

[26] R. Marquardt, "Modular Multilevel Converter: An universal concept for HVDC-Networks and extended DC-Bus-applications," in *The 2010 International Power Electronics Conference - ECCE ASIA -*, 2010, pp. 502-507.

[27] W. Lin, J. Wen, M. Yao, S. Wang, S. Cheng, and N. Li, "Series VSC-LCC converter with self-commutating and dc fault blocking capabilities," in *2014 IEEE PES General Meeting | Conference & Exposition*, 2014, pp. 1-5.

[28] T. H. Nguyen, D. Lee, and C. Kim, "A Series-Connected Topology of a Diode Rectifier and a Voltage-Source Converter for an HVDC Transmission System," *IEEE Transactions on Power Electronics*, vol. 29, pp. 1579-1584, 2014.

[29] T. H. Nguyen, D. Lee, and K. Chan-Ki, "A cost-effective converter system for HVDC links integrated with offshore wind farms," in *IECON 2013 - 39th Annual Conference of the IEEE Industrial Electronics Society*, 2013, pp. 7978-7983.

[30] T. H. Nguyen, Q. A. Le, and D. Lee, "A novel HVDC-link based on hybrid voltage-source converters," in *2015 IEEE Energy Conversion Congress and Exposition (ECCE)*, 2015, pp. 3338-3343.

[31] R. Blasco-Gimenez, S. Ano-Villalba, J. Rodriguez, V. Aldana, A. Correcher, F. Morant, *et al.*, "Variable voltage off-shore distribution network for wind farms based on synchronous generators," in *CIRED 2009 - 20th International Conference and Exhibition on Electricity Distribution - Part 1*, 2009, pp. 1-4.

[32] R. Blasco-Gimenez, S. Ano-Villalba, J. Rodriguez, F. Morant, and S. Bernal, "Uncontrolled rectifiers for HVDC connection of large off-shore wind farms," in *2009 13th European Conference on Power Electronics and Applications*, 2009, pp. 1-8.

[33] R. Blasco-Gimenez, S. A.-. Villalba, J. Rodriguez, V. Aldana, S. Bernal, and F. Morant, "HVDC connection of off-shore wind farms based on synchronous generators," in *2009 IEEE PES/IAS Conference on Sustainable Alternative Energy (SAE)*, 2009, pp. 1-5.

[34] R. Blasco-Gimenez, S. A.-. Villalba, J. Rodriguez, R. Pena, R. Cardenas, S. Bernal, *et al.*, "Fault analysis of uncontrolled rectifier HVDC links for the connection of off-shore wind farms," in *2009 35th Annual Conference of IEEE Industrial Electronics*, 2009, pp. 468-473.

[35] S. Seman, R. Zurowski, and T. Christ, *Investigation of DC Converter Nonlinear Interaction with Offshore Wind Power Park System*, 2015.

[36] P. Cartwright, L. Xu, and J. Ekanayake, *The Integration of Large Scale Wind Power Generation into Transmission Networks using Power Electronics*, 2004.

[37] S. Foster, L. Xu, and B. Fox, "Control of an LCC HVDC system for connecting large offshore wind farms with special consideration of grid fault," in *2008 IEEE Power and Energy Society General Meeting - Conversion and Delivery of Electrical Energy in the 21st Century*, 2008, pp. 1-8.

[38] S. V. Bozhko, R. Blasco-Gimenez, R. Li, J. C. Clare, and G. M. Asher, "Control of Offshore DFIG-Based Wind Farm Grid With Line-Commutated HVDC Connection," *IEEE Transactions on Energy Conversion*, vol. 22, pp. 71-78, 2007.

[39] S. Bozhko, R. Blasko-Gimenez, R. Li, J. C. Clare, and G. M. Asher, "Control of Offshore DFIG-based Wind Farm Grid with Line-Commutated HVDC Connection," in

2006 12th International Power Electronics and Motion Control Conference, 2006, pp. 1563-1568.

[40] S. Bozhko, R. Li, R. Blasco-Gimenez, G. M. Asher, J. C. Clare, L. Yao, *et al.*, "STATCOM-controlled HVDC Power Transmission for Large Offshore Wind Farms: Engineering Issues," in *IECON 2006 - 32nd Annual Conference on IEEE Industrial Electronics*, 2006, pp. 4219-4224.

[41] H. Hamlaoui and B. Francois, "Interest of storage based STATCOM systems to the power quality enhancement of thyristors based LCC HVDC links for offshore wind farm," in *2018 IEEE International Conference on Industrial Technology (ICIT)*, 2018, pp. 1702-1707.

[42] J. Xu, B. Liu, R. E. Torres-Olguin, and T. Undeland, "Grid integration of large offshore wind energy and oil & gas installations using LCC HVDC transmission system," in *SPEEDAM 2010*, 2010, pp. 784-791.

[43] H. Zhou, G. Yang, and J. Wang, "Modeling, Analysis, and Control for the Rectifier of Hybrid HVdc Systems for DFIG-Based Wind Farms," *IEEE Transactions on Energy Conversion*, vol. 26, pp. 340-353, 2011.

[44] H. Liu and J. Sun, "Small-signal stability analysis of offshore wind farms with LCC HVDC," in *2013 IEEE Grenoble Conference*, 2013, pp. 1-8.

[45] X. Dawei, R. Li, J. R. Bumby, P. J. Tavner, and S. Yang, "Coordinated control of an HVDC link and doubly fed induction generators in a large offshore wind farm," *IEEE Transactions on Power Delivery*, vol. 21, pp. 463-471, 2006.

[46] R. Li, S. Bozhko, and G. Asher, "Frequency Control Design for Offshore Wind Farm Grid With LCC-HVDC Link Connection," *IEEE Transactions on Power Electronics*, vol. 23, pp. 1085-1092, 2008.

[47] R. Li, S. Bozhko, G. M. Asher, J. C. Clare, L. Yao, and C. Sasse, "Grid Frequency Control Design for Offshore Wind Farms with Naturally Commutated HVDC Link Connection," in *2006 IEEE International Symposium on Industrial Electronics*, 2006, pp. 1595-1600.

[48] R. Li, S. V. Bozhko, and G. M. Asher, "Grid Frequency Control for LCC HVDC Link Connected Wind Farms," in *IECON 2007 - 33rd Annual Conference of the IEEE Industrial Electronics Society*, 2007, pp. 1673-1678.

[49] R. Li, S. V. Bozhko, G. M. Asher, and L. Yao, "Grid frequency control design for offshore wind farms with naturally commutated HVDC link connection," in *2007 European Conference on Power Electronics and Applications*, 2007, pp. 1-10.

[50] H. Yin and L. Fan, "Modeling and control of DFIG-based large offshore wind farm with HVDC-link integration," in *41st North American Power Symposium*, 2009, pp. 1-5.

[51] M. Zhang, X. Yuan, J. Hu, S. Wang, M. Shicong, Q. He, *et al.*, "Wind power transmission through LCC-HVDC with wind turbine inertial and primary frequency supports," in *2015 IEEE Power & Energy Society General Meeting*, 2015, pp. 1-5.

[52] M. E. Montilla-DJesus, D. Santos-Martin, S. Arnaltes, and E. D. Castronuovo, "Optimal Operation of Offshore Wind Farms With Line-Commutated HVDC Link Connection," *IEEE Transactions on Energy Conversion,* vol. 25, pp. 504-513, 2010.

[53] Z. Dongling, H. Minxiao, and S. Xu, "Coordination control for offshore wind power sending through hybrid HVDC," in *2013 IEEE Grenoble Conference*, 2013, pp. 1-6.

[54] X. He, H. Geng, G. Yang, and X. Zou, "Coordinated Control for Large-Scale Wind Farms with LCC-HVDC Integration," *Energies*, vol. 11, p. 2207, 2018.

[55] J. L. Rodriguez-Amenedo, S. Arnaltes, M. Á. Cardiel-Álvarez, and M. Montilla-DJesus, "Direct Voltage and frequency control of an offshore wind farm connected through LCC-HVDC link," in *2017 19th European Conference on Power Electronics and Applications (EPE'17 ECCE Europe)*, 2017, pp. P.1-P.10.

[56] L. Wang and M. S. Thi, "Comparisons of Damping Controllers for Stability Enhancement of an Offshore Wind Farm Fed to an OMIB System Through an LCC-HVDC Link," *IEEE Transactions on Power Systems,* vol. 28, pp. 1870-1878, 2013.

[57] L. Wang and M. S. Thi, "Stability Analysis of Four PMSG-Based Offshore Wind Farms Fed to an SG-Based Power System Through an LCC-HVDC Link," *IEEE Transactions on Industrial Electronics*, vol. 60, pp. 2392-2400, 2013.

[58] L. Wang and M. S.-N. Thi, "Stability Enhancement of a PMSG-Based Offshore Wind Farm Fed to a Multi-Machine System Through an LCC-HVDC Link," *IEEE Transactions on Power Systems,* vol. 28, pp. 3327-3334, 2013.

[59] S. M. Muyeen, R. Takahashi, and J. Tamura, "Operation and Control of HVDC-Connected Offshore Wind Farm," *IEEE Transactions on Sustainable Energy*, vol. 1, pp. 30-37, 2010.

[60] P. Mitra, L. Zhang, and L. Harnefors, "Offshore Wind Integration to a Weak Grid by VSC-HVDC Links Using Power-Synchronization Control: A Case Study," *IEEE Transactions on Power Delivery,* vol. 29, pp. 453-461, 2014.

[61] Y. Jing, R. Li, L. Xu, and Y. Wang, "Enhanced AC voltage and frequency control of offshore MMC station for wind farm connection," *IET Renewable Power Generation,* vol. 12, pp. 1771-1777, 2018.

[62] O. Gomis-Bellmunt, A. Junyent-Ferre, A. Sumper, and J. Bergas-Jane, "Control of a Wind Farm Based on Synchronous Generators With a Central HVDC-VSC Converter," *IEEE Transactions on Power Systems,* vol. 26, pp. 1632-1640, 2011.

[63] C. Feltes, H. Wrede, F. W. Koch, and I. Erlich, "Enhanced Fault Ride-Through Method for Wind Farms Connected to the Grid Through VSC-Based HVDC Transmission," *IEEE Transactions on Power Systems,* vol. 24, pp. 1537-1546, 2009.

[64] S. K. Chaudhary, R. Teodorescu, P. Rodriguez, P. C. Kjaer, and A. M. Gole, "Negative Sequence Current Control in Wind Power Plants With VSC-HVDC Connection," *IEEE Transactions on Sustainable Energy,* vol. 3, pp. 535-544, 2012.

[65] R. Vidal-Albalate, H. Beltran, A. Rolán, E. Belenguer, R. Peña, and R. Blasco-Gimenez, "Analysis of the Performance of MMC Under Fault Conditions in HVDC-Based Offshore Wind Farms," *IEEE Transactions on Power Delivery*, vol. 31, pp. 839-847, 2016.

[66] R. Zeng, L. Xu, L. Yao, S. J. Finney, and Y. Wang, "Hybrid HVDC for Integrating Wind Farms With Special Consideration on Commutation Failure," *IEEE Transactions on Power Delivery*, vol. 31, pp. 789-797, 2016.

[67] L. P. Kunjumuhammed, B. C. Pal, C. Oates, and K. J. Dyke, "The Adequacy of the Present Practice in Dynamic Aggregated Modeling of Wind Farm Systems," *IEEE Transactions on Sustainable Energy*, vol. 8, pp. 23-32, 2017.

[68] L. P. Kunjumuhammed, B. C. Pal, R. Gupta, and K. J. Dyke, "Stability Analysis of a PMSG-Based Large Offshore Wind Farm Connected to a VSC-HVDC," *IEEE Transactions on Energy Conversion*, vol. 32, pp. 1166-1176, 2017.

[69] L. Wang and M. S. N. Thi, "Comparative Stability Analysis of Offshore Wind and Marine-Current Farms Feeding Into a Power Grid Using HVDC Links and HVAC Line," *IEEE Transactions on Power Delivery*, vol. 28, pp. 2162-2171, 2013.

[70] L. Xu, B. W. Williams, and L. Yao, "Multi-terminal DC transmission systems for connecting large offshore wind farms," in *2008 IEEE Power and Energy Society General Meeting - Conversion and Delivery of Electrical Energy in the 21st Century*, 2008, pp. 1-7.

[71] L. Xu, L. Yao, and M. Bazargan, "DC grid management of a multi-terminal HVDC transmission system for large offshore wind farms," in *2009 International Conference on Sustainable Power Generation and Supply*, 2009, pp. 1-7.

[72] L. Xu and L. Yao, "DC voltage control and power dispatch of a multi-terminal HVDC system for integrating large offshore wind farms," *IET Renewable Power Generation*, vol. 5, pp. 223-233, 2011.

[73] G. O. Kalcon, G. P. Adam, O. Anaya-Lara, S. Lo, and K. Uhlen, "Small-Signal Stability Analysis of Multi-Terminal VSC-Based DC Transmission Systems," *IEEE Transactions on Power Systems*, vol. 27, pp. 1818-1830, 2012.

[74] S. Khan and S. Bhowmick, "A Generalized Power-Flow Model of VSC Based Hybrid AC-DC Systems Integrated with Offshore Wind Farms," *IEEE Transactions on Sustainable Energy*, pp. 1-1, 2018.

[75] J. Rafferty, L. Xu, Y. Wang, G. Xu, and F. Alsokhiry, "Frequency support using multi-terminal HVDC systems based on DC voltage manipulation," *IET Renewable Power Generation*, vol. 10, pp. 1393-1401, 2016.

[76] C. Li, P. Zhan, J. Wen, M. Yao, N. Li, and W. Lee, "Offshore Wind Farm Integration and Frequency Support Control Utilizing Hybrid Multiterminal HVDC Transmission," *IEEE Transactions on Industry Applications*, vol. 50, pp. 2788-2797, 2014.

[77] X. Hu, J. Liang, D. J. Rogers, and Y. Li, "Power Flow and Power Reduction Control Using Variable Frequency of Offshore AC Grids," *IEEE Transactions on Power Systems,* vol. 28, pp. 3897-3905, 2013.

[78] J. L. Rodriguez-Amenedo, S. Arnaltes, M. Aragues-Penalba, and O. Gomis-Bellmunt, "Control of the Parallel Operation of VSC-HVDC Links Connected to an Offshore Wind Farm," *IEEE Transactions on Power Delivery,* pp. 1-1, 2018.

[79] L. Guan, X. Fan, Y. Liu, and Q. H. Wu, "Dual-Mode Control of AC/VSC-HVDC Hybrid Transmission Systems With Wind Power Integrated," *IEEE Transactions on Power Delivery,* vol. 30, pp. 1686-1693, 2015.

[80] M. Raza, E. Prieto-Araujo, and O. Gomis-Bellmunt, "Small-Signal Stability Analysis of Offshore AC Network Having Multiple VSC-HVDC Systems," *IEEE Transactions on Power Delivery,* vol. 33, pp. 830-839, 2018.

[81] R. Blasco-Gimenez, S. Añó-Villalba, J. Rodríguez-D'derlée, F. Morant, and S. Bernal, "Control of an Off-Shore Synchronous Generator Based Wind Farm with Uncontrolled Rectifier HVDC Connection," *IFAC Proceedings Volumes,* vol. 43, pp. 1-6, 2010/01/01/ 2010.

[82] R. Blasco-Gimenez, S. A.-. Villalba, J. Rodríguez-D'derlée, F. Morant, and S. Bernal, "Voltage and frequency control of SG based wind farms with uncontrolled HVDC rectifier," in *2010 IEEE International Symposium on Industrial Electronics*, 2010, pp. 2499-2504.

[83] R. Blasco-Gimenez, S. Anó-Villalba, J. Rodriguez-D'Derlée, S. Bernal-Perez, and F. Morant, "Diode-Based HVdc Link for the Connection of Large Offshore Wind Farms," *IEEE Transactions on Energy Conversion,* vol. 26, pp. 615-626, 2011.

[84] S. Bernal-Perez, S. A.-. Villalba, R. Blasco-Gimenez, and J. Rodríguez-D'Derlée, "Off-shore wind farm grid connection using a novel diode-rectifier and VSC-inverter based HVDC transmission link," in *IECON 2011 - 37th Annual Conference of the IEEE Industrial Electronics Society*, 2011, pp. 3186-3191.

[85] R. Blasco-Gimenez, S. A.-. Villalba, J. Rodríguez-D'Derlée, F. Morant, and S. Bernal-Perez, "Distributed Voltage and Frequency Control of Offshore Wind Farms Connected With a Diode-Based HVdc Link," *IEEE Transactions on Power Electronics,* vol. 25, pp. 3095-3105, 2010.

[86] A. I. Andrade, R. Blasco-Gimenez, and G. R. Pena, "Distributed control strategy for a wind generation systems based on PMSG with uncontrolled rectifier HVDC connection," in *2015 IEEE International Conference on Industrial Technology (ICIT)*, 2015, pp. 982-986.

[87] A. A. Iván, P. G. Ruben, R. Blasco-Gimenez, and R. A. Javier, "Control strategy of a HVDC-Diode Rectifier connected type-4 off-shore wind farm," in *2015 IEEE 2nd International Future Energy Electronics Conference (IFEEC)*, 2015, pp. 1-6.

[88] R. Blasco-Gimenez, S. A.-. Villalba, J. Rodríguez-D'Derlée, and S. Bernal-Pérez, "Diode based HVDC link for the connection of large off-shore wind farms with self

start capability," in *Proceedings of the 2011 14th European Conference on Power Electronics and Applications*, 2011, pp. 1-9.

[89] S. Bernal-Perez, S. Ano-Villalba, R. Blasco-Gimenez, and J. Rodriguez-D'Derlee, "Efficiency and Fault Ride-Through Performance of a Diode-Rectifier- and VSC-Inverter-Based HVDC Link for Offshore Wind Farms," *IEEE Transactions on Industrial Electronics*, vol. 60, pp. 2401-2409, 2013.

[90] R. Blasco-Gimenez, S. A.-. Villalba, N. Aparicio, and S. Bernal-Perez, "Harmonic filter reduction of off-shore wind farms connected with a diode based HVDC link," in *2012 IEEE International Symposium on Industrial Electronics*, 2012, pp. 1585-1590.

[91] R. Blasco-Gimenez, N. Aparicio, S. Ano-Villalba, and S. Bernal-Perez, "LCC-HVDC Connection of Offshore Wind Farms With Reduced Filter Banks," *IEEE Transactions on Industrial Electronics*, vol. 60, pp. 2372-2380, 2013.

[92] R. Blasco-Gimenez, N. Aparicio, S. A.-. Villalba, and S. Bernal-Perez, "Connection of off-shore wind farms using a diode based HVDC link with reduced filter banks," in *2012 3rd IEEE International Symposium on Power Electronics for Distributed Generation Systems (PEDG)*, 2012, pp. 745-750.

[93] S. Bernal-Perez, S. A.-. Villalba, and R. Blasco-Gimenez, "Stability analysis of HVDC-diode rectifier connected off-shore wind power plants," in *IECON 2015 - 41st Annual Conference of the IEEE Industrial Electronics Society*, 2015, pp. 004040-004045.

[94] S. Bernal-Perez, S. A.-. Villalba, R. Blasco-Gimenez, and N. Aparicio, "Wind power plant control for the connection to multiterminal HVdc links," in *2012 IEEE Energy Conversion Congress and Exposition (ECCE)*, 2012, pp. 2873-2879.

[95] S. Bernal-Perez, S. A.-. Villalba, R. Blasco-Gimenez, and N. Aparicio, "Connection of off-shore wind power plants to VSC-MTdc networks using HVdc diode-rectifiers," in *2013 IEEE International Symposium on Industrial Electronics*, 2013, pp. 1-6.

[96] S. Añó-Villalba, R. Blasco-Gimenez, S. Bernal-Perez, and E. Belenguer, "Wind power plant integration in voltage source converter HVdc grids with voltage droop control," *Mathematics and Computers in Simulation*, vol. 146, pp. 186-199, 2018/04/01/ 2018.

[97] S. A.-. Villalba, S. Bernal-Perez, R. Pena, R. Vidal-Albalate, E. Belenguer, N. Aparicio, *et al.*, "24-Pulse rectifier for harmonic management in HVDC diode rectifier wind power plants," in *12th IET International Conference on AC and DC Power Transmission (ACDC 2016)*, 2016, pp. 1-6.

[98] D. Herrera, E. Galván, and J. M. Carrasco, "Method for controlling voltage and frequency of the local offshore grid responsible for connecting large offshore commercial wind turbines with the rectifier diode-based HVDC-link applied to an external controller," *IET Electric Power Applications*, vol. 11, pp. 1509-1516, 2017.

[99] C. Prignitz, H. Eckel, and A. Rafoth, "FixReF sinusoidal control in line side converters for offshore wind power generation," in *2015 IEEE 6th International Symposium on Power Electronics for Distributed Generation Systems (PEDG)*, 2015, pp. 1-5.

[100] C. Prignitz, H. Eckel, and H. Knaak, "Voltage and current behavior in a FixReF controlled offshore wind farm using a HVDC transmission system based on uncontrolled diode rectifier units," in *2016 18th European Conference on Power Electronics and Applications (EPE'16 ECCE Europe)*, 2016, pp. 1-6.

[101] C. Prignitz, H. Eckel, S. Achenbach, F. Augsburger, and A. Schön, "FixReF: A control strategy for offshore wind farms with different wind turbine types and diode rectifier HVDC transmission," in *2016 IEEE 7th International Symposium on Power Electronics for Distributed Generation Systems (PEDG)*, 2016, pp. 1-7.

[102] C. Prignitz, H. Eckel, and S. Achenbach, "A fault handling current control strategy for offshore wind turbines in interconnected offshore wind farms with different types of HVDC transmission," in *2017 IEEE 8th International Symposium on Power Electronics for Distributed Generation Systems (PEDG)*, 2017, pp. 1-6.

[103] R. Ramachandran, S. Poullain, A. Benchaib, S. Bacha, and B. Francois, "AC Grid Forming by Coordinated Control of Offshore Wind Farm connected to Diode Rectifier based HVDC Link - Review and Assessment of Solutions," in *2018 20th European Conference on Power Electronics and Applications (EPE'18 ECCE Europe)*, 2018, pp. P.1-P.10.

[104] M. Á. Cardiel-Álvarez, S. Arnaltes, J. L. Rodriguez-Amenedo, and A. Nami, "Decentralized Control of Offshore Wind Farms Connected to Diode-Based HVdc Links," *IEEE Transactions on Energy Conversion*, vol. 33, pp. 1233-1241, 2018.

[105] M. Á. Cardiel-Álvarez, J. L. Rodriguez-Amenedo, S. Arnaltes, and M. E. Montilla-DJesus, "Modeling and Control of LCC Rectifiers for Offshore Wind Farms Connected by HVDC Links," *IEEE Transactions on Energy Conversion*, vol. 32, pp. 1284-1296, 2017.

[106] R. Yin, D. Jiang, Y. Du, P. Hu, and Y. Liang, *A novel control strategy for offshore DFIG-based wind farm integrated through diode-rectifier-based HVDC transmission* vol. 25, 2015.

[107] C. Prignitz, H. Eckel, and H. Knaak, "DFIG wind turbines operating in a fixed reference frame," in *2015 17th European Conference on Power Electronics and Applications (EPE'15 ECCE-Europe)*, 2015, pp. 1-8.

[108] R. Vidal-Albalate, R. Pena, E. Belenguer, S. Añó-Villalba, S. Bernal Pérez, and R. Blasco-Gimenez, *Simultaneous connection of Type-3 and Type-4 offshore wind farms to HVDC diode rectifier units*, 2016.

[109] S. Seman, N. Tuan Trinh, R. Zurowski, and S. Kreplin, *Modeling of the Diode-Rectifier Based HVDC Transmission Solution for Large Offshore Wind Power Plants Grid Access*, 2016.

[110] S. Seman, R. Zurowski, and C. Taratoris, *Interconnection of advanced Type 4 WTGs with Diode Rectifier based HVDC solution and weak AC grids*, 2015.

[111] G. Chaqués-Herraiz, S. Bernal-Perez, J. Martínez-Turégano, S. A.-. Villalba, R. Peña, and R. Blasco-Gimenez, "DC voltage control in off-shore wind farms with distributed

diode rectifier units," in *IECON 2017 - 43rd Annual Conference of the IEEE Industrial Electronics Society*, 2017, pp. 202-207.

[112] N. Pogaku, M. Prodanovic, and T. C. Green, "Modeling, Analysis and Testing of Autonomous Operation of an Inverter-Based Microgrid," *IEEE Transactions on Power Electronics,* vol. 22, pp. 613-625, 2007.

[113] J. Rocabert, A. Luna, F. Blaabjerg, and P. Rodríguez, "Control of Power Converters in AC Microgrids," *IEEE Transactions on Power Electronics,* vol. 27, pp. 4734-4749, 2012.

[114] J. M. Guerrero, J. C. Vasquez, J. Matas, L. G. d. Vicuna, and M. Castilla, "Hierarchical Control of Droop-Controlled AC and DC Microgrids—A General Approach Toward Standardization," *IEEE Transactions on Industrial Electronics,* vol. 58, pp. 158-172, 2011.

[115] U. N. Gnanarathna, A. M. Gole, and R. P. Jayasinghe, "Efficient modeling of modular multilevel HVDC converters (MMC) on electromagnetic transient simulation programs," *IEEE Transactions on power delivery,* vol. 26, pp. 316-324, 2011.

[116] F. B. Ajaei and R. Iravani, "Enhanced Equivalent Model of the Modular Multilevel Converter," *IEEE Transactions on Power Delivery,* vol. 30, pp. 666-673, 2015.

[117] A. Beddard, M. Barnes, and R. Preece, "Comparison of Detailed Modeling Techniques for MMC Employed on VSC-HVDC Schemes," *IEEE Transactions on Power Delivery,* vol. 30, pp. 579-589, 2015.

[118] K. Givaki, D. Chen, and L. Xu, "Current Error Based Compensations for VSC Current Control in Weak Grids for Wind Farm Applications," *IEEE Transactions on Sustainable Energy,* vol. 10, pp. 26-35, 2019.

[119] M. Cheah-Mane, L. Sainz, J. Liang, N. Jenkins, and C. E. Ugalde-Loo, "Criterion for the Electrical Resonance Stability of Offshore Wind Power Plants Connected Through HVDC Links," *IEEE Transactions on Power Systems,* vol. 32, pp. 4579-4589, 2017.

[120] H. Saad, J. Peralta, S. Dennetière, J. Mahseredjian, J. Jatskevich, J. A. Martinez, *et al.*, "Dynamic Averaged and Simplified Models for MMC-Based HVDC Transmission Systems," *IEEE Transactions on Power Delivery,* vol. 28, pp. 1723-1730, 2013.

[121] L. Lin, Y. Lin, Z. He, Y. Chen, J. Hu, and W. Li, "Improved nearest-level modulation for a modular multilevel converter with a lower submodule number," *IEEE Transactions on Power Electronics,* vol. 31, pp. 5369-5377, 2016.

[122] P. Hu, D. Jiang, Y. Zhou, Y. Liang, J. Guo, and Z. Lin, "Energy-balancing control strategy for modular multilevel converters under submodule fault conditions," *IEEE Transactions on Power Electronics,* vol. 29, pp. 5021-5030, 2014.

[123] L. He, C. Liu, A. Pitto, and D. Cirio, "Distance Protection of AC Grid With HVDC-Connected Offshore Wind Generators," *IEEE Transactions on Power Delivery,* vol. 29, pp. 493-501, 2014.

[124] energinet, "KRIEGERS FLAK - COMBINED GRID SOLUTION," *https://en.energinet.dk/Infrastructure-Projects/Projektliste/KriegersFlakCGS*, 2018.

[125] A. Marten, V. Akmatov, T. B. Sørensen, R. Stornowski, D. Westermann, and C. Brosinsky, "Kriegers flak-combined grid solution: coordinated cross-border control of a meshed HVAC/HVDC offshore wind power grid," *IET Renewable Power Generation*, vol. 12, pp. 1493-1499, 2018.

[126] P. Krause, O. Wasynczuk, S. D. Sudhoff, and S. Pekarek, *Analysis of electric machinery and drive systems* vol. 75: John Wiley & Sons, 2013.

Author's Publications

[1] **L. Yu**, R. Li, and L. Xu, "Distributed PLL-Based Control of Offshore Wind Turbines Connected With Diode-Rectifier-Based HVDC Systems," *IEEE Transactions on Power Delivery*, vol. 33, pp. 1328-1336, 2018.

Abstract: A distributed PLL-based frequency control is proposed in this paper for offshore wind turbine converters connected with diode-rectifier based high-voltage-direct-current (HVDC) systems. The proposed control enables a large number of wind turbines to work autonomously to contribute to the offshore AC frequency and voltage regulation. The proposed control also provides automatic synchronization of the offline wind turbines to the offshore AC grid. Stability of the proposed frequency control is analysed using root locus method. Moreover, an active dc voltage control of the onshore modular multilevel converter (MMC) is proposed to ride-through onshore AC fault, where the onshore MMC converter quickly increases the dc voltage by adding additional submodules in each phase, in order to rapidly reduce wind farm active power generation so as to achieve quick active power re-balance between the offshore and onshore sides. Thus, the overvoltage of the submodule capacitor is alleviated during the onshore fault, reducing the possibility of system disconnection. Simulation results in PSCAD verify the proposed control strategy during start-up, synchronization and under onshore and offshore fault conditions.

[2] **L. Yu**, R. Li, and L. Xu, " Hierarchical control of offshore wind farm connected by parallel diode-rectifier based HVDC and HVAC links," *IET Renewable Power Generation*. (accepted).

Abstract: This paper investigates the operation of offshore wind farm connected by parallel diode-rectifier based HVDC (DR-HVDC) and HVAC links. A secondary voltage control is proposed to control the offshore AC voltage amplitude by regulating the DC voltage of the DR-HVDC link. A secondary frequency control and a phase angle control are proposed to adjust the reactive power reference in the primary control, which synchronise the offshore point of common coupling (PCC) frequency and phase angle to those of the HVAC link. Such secondary voltage control, frequency

control and phase angle control enable seamless transition from DR-HVDC mode to parallel mode. A tertiary power control scheme is further proposed to control the active power flow distribution between DR-HVDC and HVAC links through the regulation of PCC phase angle. To ensure smooth transition from HVAC mode to parallel mode, a virtual DC power control is proposed to control the virtual DC power at zero prior to the connection of the DR-HVDC link. A small-signal model of the parallel system is developed and the stability analysis is carried out for the proposed control scheme. Simulation results in PSCAD/EMTDC verify the proposed control under normal and fault conditions.

[3] **L. Yu**, R. Li, L. Xu and Grain P. Adam, "Analysis and Control of Offshore Wind Farm Connected with Diode Rectifier based HVDC System," *IEEE Transactions on Power Delivery.* (under second-round review).

Abstract: This paper analyses the control and operation of offshore wind farms connected with diode rectifier based HVDC (DR-HVDC) system. A small-signal state-space model of the offshore wind turbines (WTs) and DR-HVDC system is developed to investigate the interactions among the active and reactive power (*P* and *Q*), offshore AC voltage and frequency (*V* and *f*) at the offshore network level. The impact of using the previously proposed *P*-*V* and *Q*-*f* control on the individual WT active and reactive power transmission to offshore AC network and their interaction are clarified. In order to reduce the coupling between WT active power and reactive power, an angle compensation control is proposed where an additional phase shift is directly added to the WT output voltage based on the WT's active power output. The effectiveness of the proposed control on improving dynamic response and reducing active and reactive power interaction is verified by frequency-domain analysis and time-domain simulations in PSCAD/EMTDC.

[4] **L. Yu**, R. Li, and L. Xu, "Parallel operation of diode-rectifier based HVDC link and HVAC link for offshore wind power transmission," in the 7th International Conference on Renewable Power Generation (RPG2018), 2018.

Abstract: This paper investigates the integration of large offshore wind farms using parallel HVAC and diode-rectifier based HVDC (DR-HVDC) systems. Three different

operation modes, i.e. HVAC operation mode, DR-HVDC operation mode and parallel operation mode are investigated. A wind turbine control scheme including distributed control and centralized control is proposed to ensure the stable operation of the offshore wind farms under different operation modes. The proposed control requires no switching of the distributed control strategy when operation mode is changed. Moreover, power flow between the DR-HVDC link and HVAC link under parallel operation can be well controlled with the centralized control. Simulation results in PSCAD/EMTDC verify the proposed control during transition among the three operation modes.

[5] R. Li, **L. Yu**, and L. Xu, "Offshore AC Fault Protection of Diode Rectifier Unit-Based HVdc System for Wind Energy Transmission," *IEEE Transactions on Industrial Electronics*, vol. 66, pp. 5289-5299, 2019.

Abstract: Offshore AC fault protection of wind turbines (WTs) connecting with diode rectifier unit based HVDC (DRU-HVDC) system is investigated in this paper. A voltage-error-dependent fault current injection is proposed to regulate the WT current during offshore AC fault transients and quickly provide fault current for fault detection. Considering different fault locations, the fault characteristics during symmetrical and asymmetrical faults are presented and the requirements for fault detection are addressed. A simple and effective offshore AC fault protection solution, combining both overcurrent protection and differential protection, is proposed by utilizing the developed fast fault current providing control. To improve system availability, reduced DC voltage of the DRU-HVDC system is investigated, where one of the series-connected DRUs is disconnected and the onshore modular multilevel converter (MMC) actively reduces DC voltage to resume wind power transmission. The proposed scheme is robust to various offshore AC faults and can automatically restore normal operation. Simulation results confirm the proposed fault protection strategy

[6] R. Li, **L. Yu**, L. Xu and Grain P. Adam, " Coordinated Control of Parallel DR-HVDC and MMC-HVDC Systems for Offshore Wind Energy Transmission," *IEEE*

Journal of Emerging and Selected Topics in Power Electronics. (under second-round review).

Abstract: Parallel operation of diode rectifier based HVDC (DR-HVDC) and modular multilevel converter (MMC) based HVDC (MMC-HVDC) for transmitting offshore wind power is investigated in this paper. An enhanced active power control scheme of the offshore MMC station is proposed to improve the power flow distribution between the MMC-HVDC and DR-HVDC links which are both connected to the offshore wind farm AC network. By regulating the offshore voltage, all the wind powers are transmitted via the DR-HVDC link in low wind conditions while the offshore MMC power is controlled around zero to reduce transmission losses, considering the efficiency superiority of DR-HVDC over its MMC counterpart. When the DR-HVDC is out of service, wind energy is transferred via the MMC-HVDC and the wind turbine generated power is automatically limited by slightly increasing the offshore AC voltage to avoid potential MMC-HVDC overload. A power curtailment control is also proposed which slightly increases the DC voltage of the DR-HVDC to enable autonomous reduction of the generated wind power so as to avoid DR-HVDC overload during MMC-HVDC outage. The proposed coordinated control only uses local measurements and, without the need for communication, can seamlessly handle transitions including various faults. The proposed scheme provides a highly efficient solution with flexible operation for integrating large offshore wind farms. Simulation results confirm the proposed control strategy.

[7] R. Li, **L. Yu**, and L. Xu, "Operation of offshore wind farms connected with DRU-HVDC transmission systems with special consideration of faults," *Global Energy Interconnection,* vol. 1, pp. 608-617, 2018.

Abstract: The diode rectifier unit (DRU)-based high-voltage DC (DRU-HVDC) system is a promising solution for offshore wind energy transmission thanks to its compact design, high efficiency, and strong reliability. Herein we investigate the feasibility of the DRU-HVDC system considering onshore and offshore AC grid faults, DC cable faults, and internal DRU faults. To ensure safe operation during the faults, the wind turbine (WT) converters are designed to operate in either current-

limiting or voltage-limiting mode to limit potential excessive overcurrent or overvoltage. Strategies for providing fault currents using WT converters during offshore AC faults to enable offshore overcurrent and differential fault protection are investigated. The DRU-HVDC system is robust against various faults, and it can automatically restore power transmission after fault isolation. Simulation results confirm the system performance under various fault conditions.

[8] R. Li, **L. Yu**, L. Xu, and G. P. Adam, "DC Fault Protection of Diode Rectifier Unit Based HVDC System Connecting Offshore Wind Farms," in *2018 IEEE Power & Energy Society General Meeting (PESGM)*, pp. 1-5, 2018.

Abstract: DC fault ride-through operations of the offshore wind farm connecting with diode rectifier unit (DRU) based HVDC link are presented in this paper. A voltage-error-dependent fault current injection is proposed to regulate the WT current during DC faults and to provide fault current. This contributes the control of the offshore AC voltage, which does not drop to zero but is remained relatively high to facilitate fast system recovery after clearance of a temporary DC fault. The WT converters operate on current limiting mode during DC faults and automatically restore normal operation after fault clearance. The full-bridge based modular multilevel converter (MMC) is adopted as the onshore station and its DC fault current control ability is explored to effectively suppress the fault current from the onshore station around zero, which reduces semiconductor losses and potential overcurrent risk of the MMC station. Simulation results confirm the robustness of the system to DC faults.